Stephen P. Berkebile

Electronic and Geometric Structure of Sexiphenyl on TiO_2(110):

From interface formation to device relevant dimensions

Diplomarbeit

zur Erlangung des akademischen Grades eines

Magisters

an der Naturwissenschaftlichen Fakultät der

Karl-Franzens-Universität Graz

Ao.Univ.-Prof. Dr. M.G. Ramsey

Institut für Experimentalphysik

Oberflächen- und Grenzflächenphysik

2004

To my parents,

for their steady love and support during the completion of this thesis and throughout my studies.

Table of Contents

List of Abbreviations

6P	Sexiphenyl
ϕ	Work function
AEY	Auger electron yield
AFM	Atomic force microscopy
BE	Binding energy
E_F	Fermi level
E_{vac}	Vacuum level
HOMO	Highest occupied molecular orbital
HT	High temperature
IP	Ionization potential
ISEELS	Inner-shell electron energy loss spectroscopy
LEED	Low-energy electron diffraction
LNT	Liquid nitrogen temperature
LUMO	Lowest unoccupied molecular orbital
ML	Monolayer
MO	Molecular orbital
NE	Normal emission
NEXAFS	Near-edge X-ray absorption fine structure
NI	Normal incidence
PEY	Partial electron yield
PL	Photoluminescence
RDS	Reflectance difference spectroscopy
RT	Room temperature
STM	Scanning tunneling microscopy
TEY	Total electron yield
UHV	Ultrahigh vacuum
UPS	Ultraviolet photoemission spectroscopy
w.r.t.	with respect to
XPS	X-ray photoemission spectroscopy
XRD	X-ray diffraction

Chapter 1

Introduction

Thin films of organic materials as the active layer in electronic and optoelectronic devices have attracted considerable interest for more than fifteen years, yet consumer devices utilizing these materials have only appeared within the last few years. Although the quality of these devices has steadily improved and with it, their range of applications, the pace of device development seems to have outstripped the understanding of basic properties of film growth, critical for device operation.

The most important characteristics of an organic thin film affecting device properties are film morphology, charge transport in the active organic layer and charge injection at the interfaces between the active layer and the inorganic electrodes of the device, shown schematically in Fig.1.1. Although often mentioned in studies of organic devices, little work is devoted directly to the understanding and improvement of these characteristics. Furthermore, the advent of organic nanotechnology will require both the ability to grow oriented crystalline structures on a nanometer scale and a basic comprehension of their electronic, morphologic and crystalline properties.

Charge injection at the interface between the active organic layer and the inorganic contact is governed by the relative positions of the highest occupied molecular orbital (HOMO) and the lowest unoccupied molecular orbital (LUMO) of the organic material with respect to the Fermi level of the inorganic contact (see

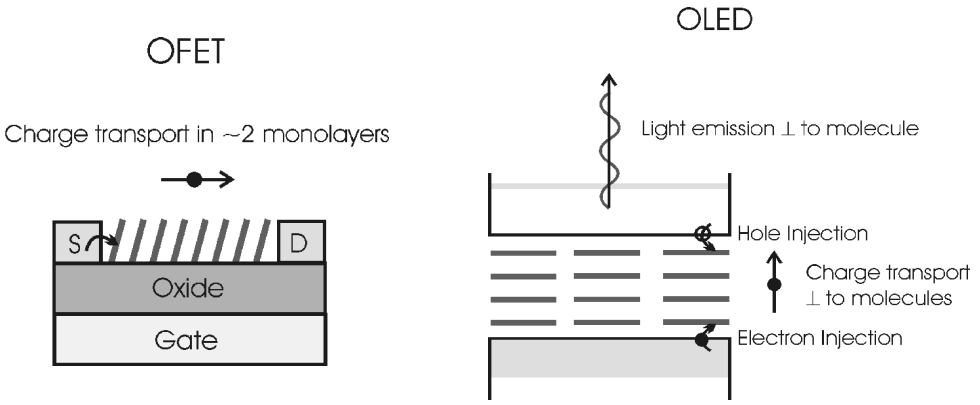

Figure 1.1 *Representation of an organic field effect transistor (OFET), also called organic thin film transistor (OTFT), and an organic light emitting diode (OLED).*

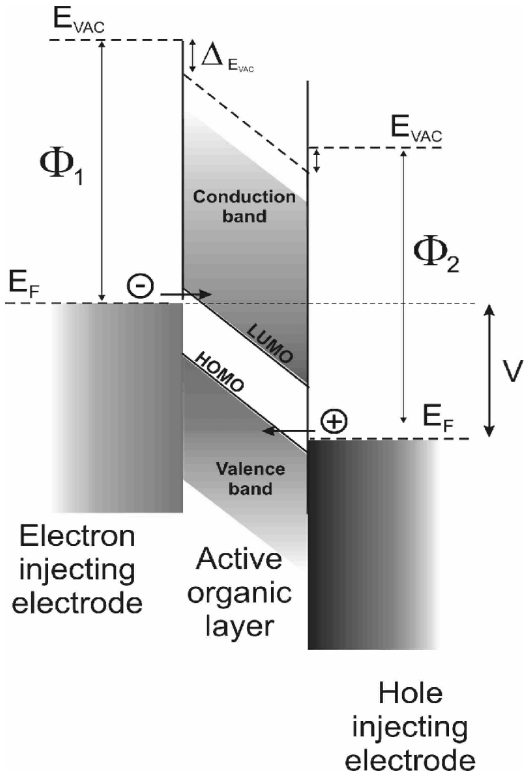

Figure 1.2 *Energy level diagram of a model organic/inorganic device.*

Fig.1.2). For good hole injection, the valence band of the organic layer should be close to the Fermi level E_F of the hole injecting electrode, while for electron injection, the conduction band of the organic layer should be close to E_F of the electron injecting electrode. The alignment of these levels is determined by the interface dipole Δ, which is specific to the interaction at the organic-inorganic interface [1],[2].

It has been demonstated that this alignment can be tuned over a wide range for a particular molecule by the selection of inorganic contact material [1] or, indeed, for the same contact material through its temperature and cleanliness during film growth [3]. The importance of band alignment in determining the electrical properties of a device was demonstrated in thin film transistors (TFTs) with pentacene as the active material. It was seen that the threshold voltage could be varied over a wide range by controlling the interface properties between the active layer and gate dielectric [4].

The orientation of the molecules in the active organic layer is decisive in the quality of a device. Not only does the molecular orientation affect charge injection at the organic/inorganic interface, it also influences the movement of charge carriers through the organic layer [5]. Carrier transport in oligophenyl-based TFTs is dominated by the difficulty of moving carriers from one molecule to the next (Fig.1.1). Disorder in the crystal structure of the organic layer presents one of the greatest hindrances to high carrier mobilities [6]. Yet even highly ordered crystals perform poorly as an active layer if the molecular orientation is inappropriate. Charge transport in crystals of conjugated molecules primarily occurs perpendicular to the molecular axis, with transport along the axis hindered by a significant potential barrier. Moreover, morphologically, thin films are comprised of small domains where the many boundaries present a further obstacle to charge transport.

The growth of highly oriented crystalline films of conjugated organic materials is, therefore, of great interest as this may lead to improved performance in organic thin film transistors (OTFTs) and organic light emitting diodes (OLEDs) [7],[8] and organic photovoltaic cells.

While band alignment and charge transport are crucial for the development of high-quality organic devices, equal attention must be given to the morphology of films intended for use in devices. Crystallites must be of sufficient size, since each domain boundary represents not only a loss in charge transport but also a potential channel for

the diffusion of impurities and a possible cause of short circuits.

Another morphological consideration is the roughness of the film. OTFTs and OLEDs are planar devices, consisting of any number of layers, implying that a relatively flat morphology is sought to avoid mixing between layers, channels for undesired current leakage and inhomogeneous field strengths. Additionally, novel crystal structures may present new uses in their own right. For example, the use of *para*-phenylene oligomers as nanoscaled waveguides has already been demonstrated [9],[10].

The question remains of how one achieves such ordered layers and controls their orientation with respect to the substrate. Although other methods exist, the most promising is molecular self-assembly. In this thesis, a patterned anisotropic substrate has been used as a template to influence molecular organization and, therefore, to guide molecular self-assembly. It has already been demonstrated that the control of the electronic and geometric structure at the molecular level is possible and has been successfully employed in thin layers of bithiophene [1],[11]. The characterization of the growth of organic crystals on numerous substrates, both metallic and nonmetalic, will be decisive in the development of better organic devices and will most certainly lead to new, previously unconceptualized possibilities.

In the present study, *para*-sexiphenyl (*p*-6P: $C_{36}H_{26}$) films grown via physical vapour deposition on a TiO_2 (110) single crystal substrate have been investigated. *p*-6P, a π-conjugated organic molecule, is of technological relevance since it is used as the active material in blue light emitting diodes [12], and is also considered to be a promising material for solar cells [13]. The TiO_2 substrate is interesting because it is an optically clear insulating oxide, which can be n-doped via heat treatment in UHV to become conductive. The use of TiO_2 as an electrical contact would preclude the necessity of removing the molecular layer from the growth substrate for optical devices. Moreover, the TiO_2(110) orientation is highly anisotropic and can thus be used as a template for crystalline film growth to steer molecular orientation.

Numerous studies on various substrates have shown that substrate temperature during evaporation strongly influences the morphology, crystallinity and electronic structure of *p*-6P films [3],[14],[15],[16]. Therefore, the growth of *p*-6P films was studied over a wide range of temperatures, from -190°C to 150°C, in order to control

molecular orientation and optimize film growth.

The basic layout of this thesis is as follows. In Chapter 2, the *in-situ* UHV techniques used in this study will be described, followed by the *ex-situ* (in air) techniques. Chapter 3 will discuss the particulars of the experimental system used: *p*-6P and TiO_2(110). In Chapters 4 through 6, the bulk of the results of experiments carried out during the course of this thesis will be presented. These results have been divided by chapter into liquid nitrogen temperature growth (LNT), high temperature growth (HT) and room temperature growth (RT), in that order. Films grown at LNT and HT substrate temperature are more homogeneous in their growth and have therefore been placed before RT growth, the most complicated and, arguably, the most interesting of the three cases. In each of these chapters, the electronic structure, morphology and molecular orientation will be presented and discussed. The final chapter will summarize the growth at different temperatures and present a unified picture of this particular experimental system.

Chapter 2

Experimental Techniques

2.1 *in-situ* Ultra-high Vacuum

A variety of *in-situ* ultra-high vacuum (UHV) techniques were performed to study the growth of *p*-6P on TiO_2(110). Most experiments using the following *in-situ* techniques were done in a custom-built UHV chamber with a Scienta SES-200 analyzer (SCIENTA system) at the Karl-Franzens University, Graz, which has been described in more detail before [17]. The exception is the near edge X-ray absorption fine structure (NEXAFS) technique, which was done in the MUSTANG end-chamber attached to the Russian-German beam-line at the synchrotron radiation facility BESSY II, Berlin. The UHV chambers used in this study had base pressures in the low 10^{-10} mbar range.

2.1.1 Photoelectron Spectroscopy

First described by Einstein in 1905, the photoemission process is the basis of several important surface science techniques. In the photoemission process, an electron is given the energy of an incident photon and is ejected from its host material.

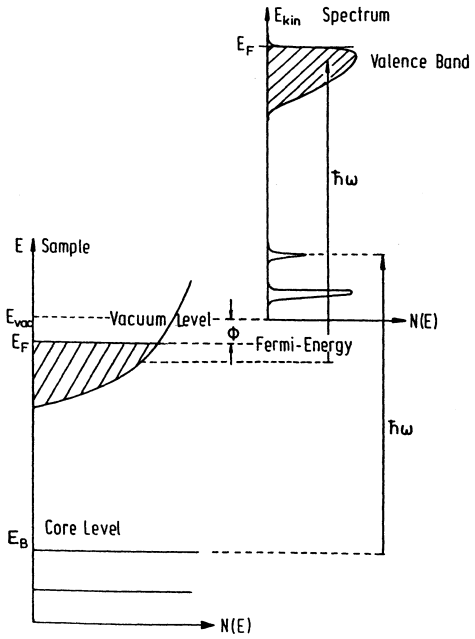

Figure 2.1 *In the photoemission process an electron from an atomic core level or from the valence band of a solid is given the energy of a photon* hν (= ħω). *It is then ejected from the solid with a kinetic energy* E_{kin} *equal to hν minus the work function* φ *of the solid and the binding energy of the electron* E_B. *(from Hüfner [*18*]).*

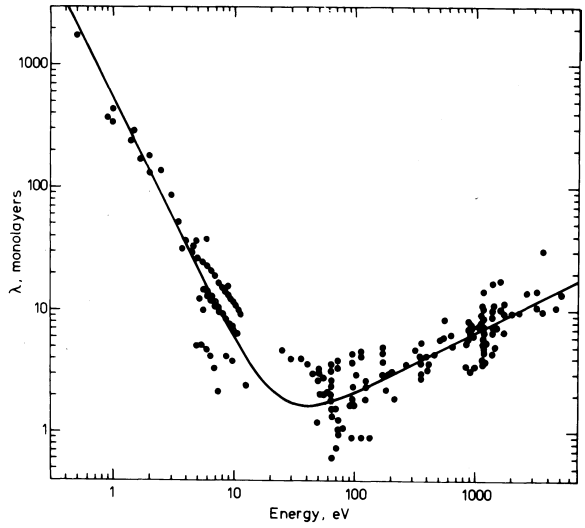

Figure 2.2 *The electron mean free path in different solids as a function of their kinetic energy forms what is known as the universal curve. The mean free path is given in monolayers. A monolayer is the thickness of a overlayer when it just completely covers the substrate beneath it (from Ertl [*19*]).*

The kinetic energy of this ejected electron depends on the energy of the photon *hν*, the binding energy of the electron in its host material E_B and the work function of the material ϕ according to

$$E_{kin} = h\nu - E_B - \phi, \tag{2.1}$$

illustrated in Fig.2.1. Note that the photon energy must be greater than the binding energy of the electron and the work function of the material if a photon is to be emitted. If the photon energy *hν* is known, information about the elements present in a sample, their chemical state and the electronic structure of the valence band can be gained.

Due to the high cross section of electrons with kinetic energies between 10 eV and 1000 eV in solids, photoemission can be used as an effective tool to determine the

growth mode of a material on a substrate. The mean free path of an electron in various solids forms a 'universal curve', which is shown in Fig.2.2.

Ultraviolet Photoelectron Spectroscopy – UPS

Ultraviolet Photoelectron Spectroscopy (UPS) utilizes ultraviolet light ($h\nu$ = 10 – 100 eV) from a helium lamp or a synchrotron source to excite the electrons of the valence band of a sample. The number of photoelectrons collected is displayed as a function of their kinetic energy. In this study, the He I line of a helium lamp with $h\nu$ = 21.2 eV and a linewidth in the meV range was used. The He II line with $h\nu$ = 40.813 eV was also available from the lab source but not used in this study.

A UPS spectrum reflects, to a first approximation, the density of states N(E) (DOS) of the valence band and is used to study its electronic structure. UPS can also give indications of the growth mode of a material on a substrate with strong features, due to the small escape depth of the electrons with kinetic energies between 10 eV and 20 eV (Fig.2.2).

Photoelectrons collected as a function of angle, called angle-resolved UPS (ARUPS), can be used to determine the orientation and bonding geometry of absorbed molecules. Angular behavior of emitted photoelectrons is governed by the differential cross section in the dipole approximation, as expressed by Fermi's 'Golden Rule':

$$\frac{d\sigma}{d\Omega} \sim \left| \langle f | \boldsymbol{P}\,\boldsymbol{A} | i \rangle \right|^2 \delta(E_f - E_i - h\nu). \tag{2.1}$$

The 'Golden Rule' describes the transition from an initial state $|i\rangle$ to a final state $|f\rangle$, determined by the momentum operator $\boldsymbol{P}$ and the vector potential $\boldsymbol{A}$ of the incoming electromagnetic radiation (photon). Based on Eqn.2.1, predictions can be made as to whether a particular orbital will be observable or forbidden for a particular geometry.

A determination of molecular geometry using ARUPS relies on the use of polarized light and restricted electron collection angles. Although nonpolarized light was used in these experiments and the analyzer had a large acceptance angle (± 8°), existing angular differences can give an indication of order in the sample.

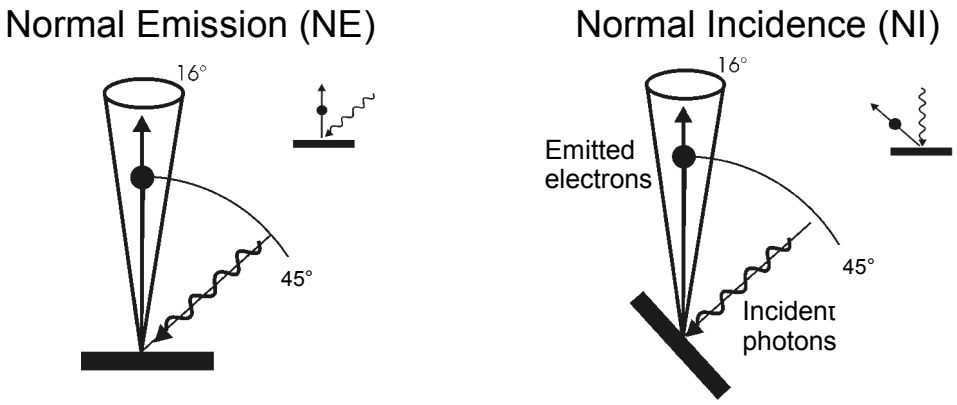

Figure 2.3 *The geometries used for UPS Spectra taken with the Scienta SES-200 analyzer. The analyzer has an acceptance angle of 16°. The TiO_2(110) substrate could also be rotated about its surface normal to place either the [001] or [1$\underline{1}$0] azimuthal direction parallel to the experimental plane formed by the incident photons and emitted electrons.*

The experimental geometries used in this study are shown in Fig.2.3. Later spectra are labeled according to which azimuth of the surface is in the experimental plane formed by the incident photons and emitted electrons and to which emission geometry was used, normal emission (NE) or normal incidence (NI).

The features of the valence band lie on a background of secondary electrons which increases strongly at lower electron kinetic energies. These secondary electrons have lost energy through multiple scattering processes and contain no specific information about their initial state. They are used to determine the work function of a material.

Fig.2.4 shows full-scale UPS spectra measured with a bias (a),(b) (9-V battery, measured at 8.05 V) and without a bias (c),(d). The secondary-electron cut-off is observed at the energy position of the vacuum level E_{vac}. The work function $\phi = E_F - E_{vac}$ can be determined by measuring the position of the cut-off with respect to the Fermi level E_F. Alternatively, the width of the spectrum can be deducted from the photon energy to measure the work function. In the experiments conducted with the SCIENTA system, the secondary electron cut-off displayed an unusual shape for some coverages, as in Fig.2.4(d). Thicker films, particularly when measured at low temperature (LNT), were especially problematic. Applying a bias to the sample

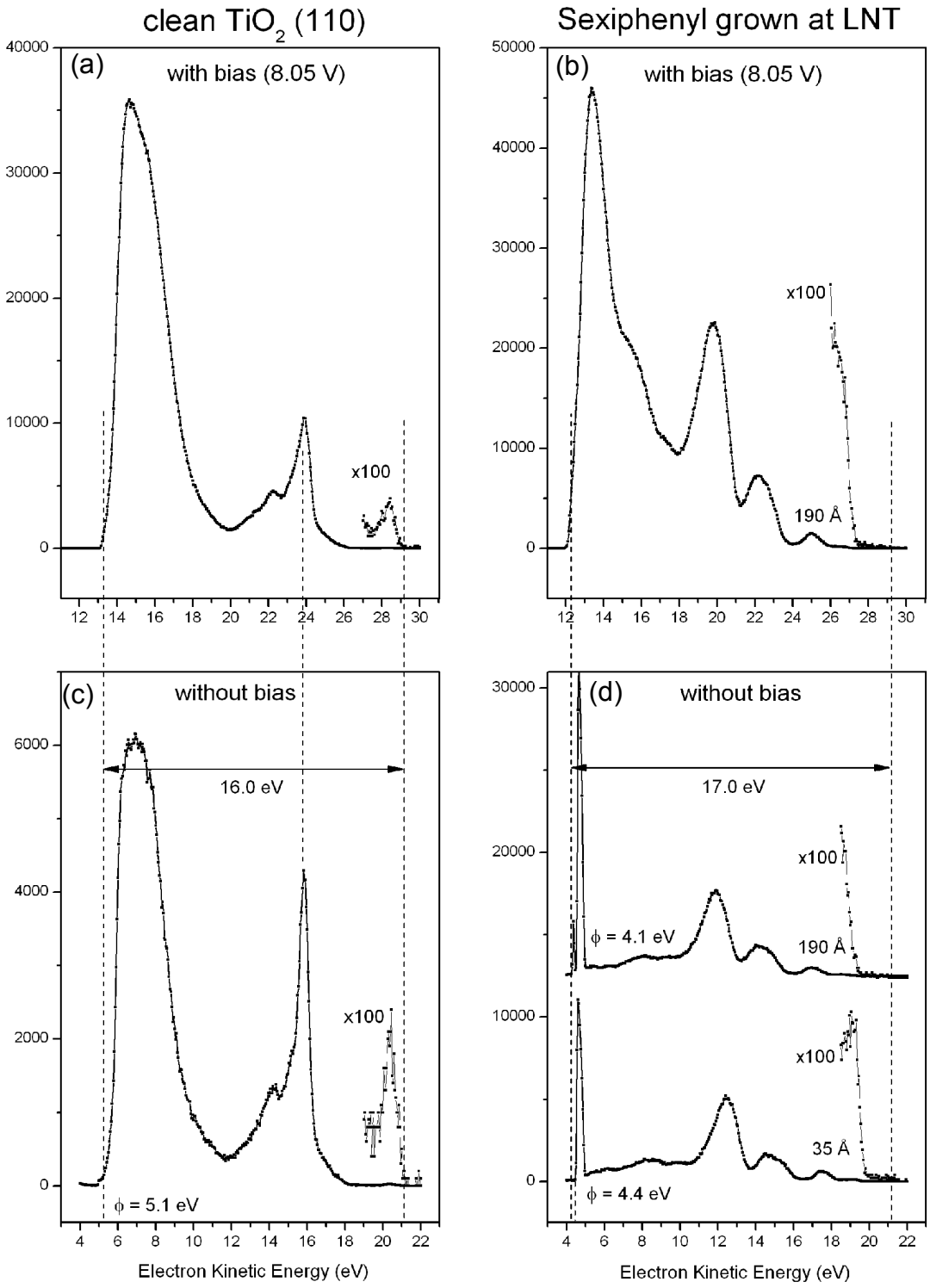

Figure 2.4 *Work function measurements were made with UPS. The spectra have been aligned between* ***(a),(b)*** *those taken with a bias of 8.05 V on the sample and* ***(c),(d)*** *those without a bias.*

corrected this problem (Fig.2.4(b)), indicating that the irregular transmission function at these low energies is likely due to the electron lenses of the SES-200 analyzer.

Regardless of the use of a bias, the slope of the secondary electron cut-off was often uneven. For consistency, the work function was measured at the position of the leading edge of the secondary electron cut-off, as shown in the spectra of Fig.2.4.

All UPS spectra in this work were measured in the SCIENTA experimental system using a Scienta SES-200 hemispherical analyzer with a curved 0.8 mm slit and an electron pass energy of E_p = 20 eV, which together gives an expermental resolution of 66 meV, as previously measured [17]. The work function measurements were done with a pass energy of E_p = 10 eV and the same values were obtained from measurements made with and without a bias.

X-ray Photoelectron Spectroscopy – XPS

X-ray Photoelectron Spectroscopy (XPS) uses X-rays ($h\nu$ = 100 – 1500 eV) to excite the core level electrons which lie at deeper levels than UPS can probe. The binding energies of core level orbitals are element specific, allowing XPS to be used for chemical analysis. The shape and position of the core-level peaks offers information on the chemical states of an element.

In the SCIENTA system, two sources are available: the Mg K_α emission of $h\nu$ = 1253.7 eV (resolution 0.70 eV) and the Al K_α emission of $h\nu$ = 1486.6 eV (resolution 0.85 eV). No synchrotron XPS was done in this study.

Auger electron features are visible in an XPS spectrum in addition to the direct core level emissions. Auger electrons are created when an electron is emitted from a core level. Another electron at a lower binding energy, e.g. from the valence band, can drop into the hole created at the core level giving the energy lost in this transition to a third electron which is then emitted from the material. Since the kinetic energy of this emitted electron depends only on its binding energy and the energy of the transition of the second electron to the hole, Auger features do not change in kinetic energy with changing photon energy.

XPS was used exclusively to check substrate cleanliness in this study. Although XPS can also be used to study the morphology and growth of a film due to the small escape depth of the photoelectrons (Fig.2.2), it was not used in the present

study. This decision was reached when it became evident that X-rays damaged the *p*-6P films grown. At growth on a room temperature substrate, a shift of the entire spectrum towards higher BE was seen, as well as an equal shift in the work function. The same phenomenon was observed for growth on a low temperature substrate, in addition to a loss in the clarity of the π-band at low coverages (~10 Å).

2.1.2 Near Edge X-ray Adsorption Fine Structure – NEXAFS

Near Edge X-ray Adsorption Fine Structure (NEXAFS) spectroscopy is a powerful technique used to determine the orientation of molecular adsorbates. The X-ray absorption process excites electrons from core levels to unoccupied molecular orbitals (UMO). As the photon energy is swept, the X-ray absorption of a particular core level is monitored. The resulting spectra display the intensity of these absorption resonances versus photon energy. A model of the adsorption process is seen in Fig.2.5.

In order to sweep the photon energy, a synchrotron light source is required. The linearly polarized nature of dipole synchrotron radiation allows the selection of particular resonances depending on experimental geometry. This effect, particularly strong for K-shell spectra, allows NEXAFS to be used in determining molecular orientation.

The NEXAFS experiments were performed in the MUSTANG end station attached to the Russian-German beam line at the synchrotron radiation facility BESSY II, Berlin with the assistance Dr. Denis Vyalikh. The Russian-German beamline has a polarization of over 95%. Partial electron yield NEXAFS spectra were obtained using a partial yield detector with an overall resolution of <0.3 eV. Auger electron yield NEXAFS spectra were obtained using a Specs electron energy analyzer. Only K-shell excitations of carbon, the excitations from the C_{1s} level to unoccupied states, are presented in this thesis.

The schematic in Fig.2.5 shows the effective molecular potential of a diatomic molecule, which differs in shape from the typical muffin-tin potential seen in any solid-state physics text. The centrifugal barrier in the effective molecular potential

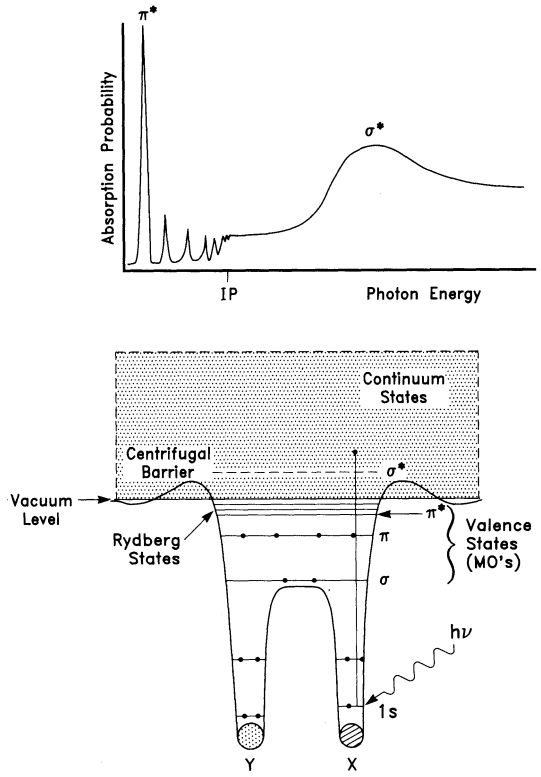

Figure 2.5 *A energy diagram of the states involved in the NEXAFS process (below). Such a diatomic molecule would produce the NEXAFS spectrum found above (from Stöhr [20]).*

arises from an extra centrifugal term $l(l+1)\hbar^2/2mr^2$ when the Schrödinger equation is written in spherical coordinates. Although the angular momentum l of the final electron state is equal to 1 in the coordinate system of the excited atom in a K-shell spectrum, it can take on any value in the coordinate system of the molecule, often leading to an appreciable potential barrier.

The UMOs, indicated with a *, lie above and below the vacuum level E_{vac} in a neutral molecule. In the core-excited molecule, the electron-hole Coulomb attraction produces a shift in these orbitals that pulls them to a lower energy than in the unexcited state. These orbitals are confined within the molecular potential barrier, leading to exceptionally long excited-state lifetimes and, therefore, sharp features. The most interesting of the UMOs in our case is the lowest unoccupied molecular orbital, the π* LUMO.

This description of the X-ray absorption process is for diatomic molecules. Regardless, it is valid for more complex molecules, such as *p*-6P. For an in depth description of this process, see Stöhr [20].

A detailed description of resonant energy positions and intensities for the

NEXAFS spectra requires the initial state $|i\rangle$ and final state $|f\rangle$ of the system to be solved by the Schrödinger equation. However, trends can be predicted and molecular orientation obtained by using symmetry classifications of resonances which come from the direct relationship between resonances and molecular orbitals [20]. Through the use of these symmetry classifications, the angular dependence of the transition matrix elements for a transition from a core level to an unoccupied molecular orbital can be derived and the angular behavior of the associated resonance can be determined.

In Fig.2.6, the two lowest UMOs of the relatively simple ethylene molecule are shown. The orbital on top displays σ symmetry, because it is symmetric about the molecular axis. The bottom orbital is antisymmetric about the molecular axis, which is defined as having π symmetry.

The 1s state, the core level from which the electrons are excited, has σ symmetry. According to the dipole selection rules, the final state must contain an atomic p-orbital component and can be σ or π in character. These molecular orbitals have a strong directional character. The spatial orientation of the orbitals is directly related to the molecular geometry. [20] Oriented molecules and polarized X-rays cause the resonance intensities of σ* and π* final states to display opposite dicroism. The dichroic behavior of the π* and σ* orbitals of ethylene is shown in Fig.2.6. A C_{1s} electron will be excited to the respective UMO by polarized X-rays with an electric field vector $\vec{E}$ in the indicated orientation.

There are several typical K-shell NEXAFS resonances, which shall be briefly described. The lowest in all K-shell spectra, the 1s → π* transition is referred to as *π* resonance.* Typically, a small upward relaxation shift of 1s orbital and a downward shift of outer orbital due to the increased attractive Coulomb potential (Z+1), results in transition energy of the π* lower in energy than the 1s ionization potential IP.

Rydberg and mixed valence/Rydberg resonances exist between the π* resonance and the IP. The series of Rydberg resonances merge into a continuous step-like feature about 2 eV below the IP. The mixing is caused primarily by the Rydberg states being pulled below E_{vac} by the electron-hole interaction, a final state effect. [20]

σ* shape resonances lie in the continuum above the IP for low Z molecules, some resonances with σ* character were seen below the IP in *p*-6P (see Chapter 3).

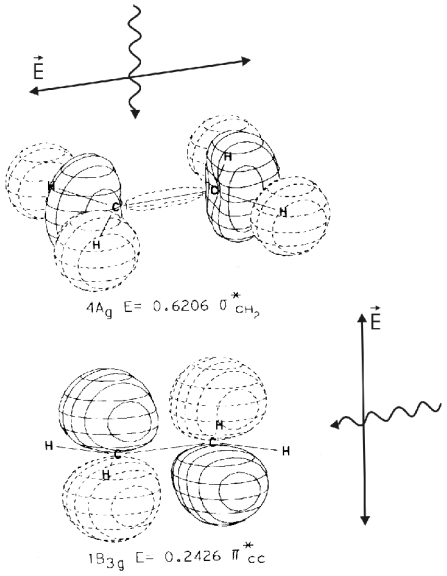

Figure 2.6 *The two lowest unoccupied orbitals of ethylene (from Jorgensen [21]). The polarization vector of the incident photons is oriented such that a C1s transition to the respective orbital is probable.*

Figure 2.7 *The π* MO of benzene can be represented by a vector perpendicular to the plane of the aromatic ring, the σ* MOs by a plane parallel to the ring (from Stöhr [20].*

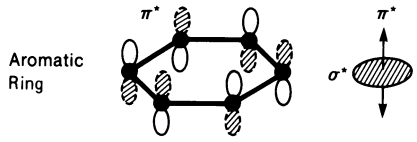

The term "shape resonances" refers to the idea that the excited state is shielded from immediate decay by the hump in the centrifugal potential barrier, even if the state lies above the barrier. At higher energies, σ* shape resonances tend to have a broader shape due to increasing decay probability.

In Chapter 3, an attempt is made at identifying these features in *p*-6P through a comparison with relatively simple benzene spectra applying the building block principle.

As mentioned above, the σ* and π* resonances display opposite behavior with incident X-ray angle. This behavior can be derived from the X-ray absorption cross section σ_X, which can be calculated from Fermi's "Golden Rule",

$$P_{if} = 2\frac{\pi}{\hbar}|\langle f|\bar{V}|i\rangle|^2 \rho_f(E)\,, \tag{2.2}$$

for the probability of a transition from an initial state $|i\rangle$ to a final state $|f\rangle$ driven by a harmonic time-dependent perturbation $V(t)=\bar{V}e^{-i\omega t}$. P_{if} is the excitation probability per unit time, and $\rho_f(E)$ is the energy density of final states (more details can be found in Stöhr [20]).

For K-shell spectra, it is convenient to classify the highly directional MOs into general groups. According to Stöhr [20], a single orbital can be represented by a vector, and two orthogonal orbitals by a plane, leading to the classifications seen in Fig.2.7. The π* orbital in a benzene ring is represented by a vector perpendicular to the plane of the ring, while the symmetry of the σ* orbitals leads to their representation as a plane parallel to the aromatic ring.

The dipole selection rules for K-shell resonances can be summarized as follows. The intensity of the resonance is largest when its associated MO vector points in the same direction as the electric field vector $\vec{E}$ of the polarized X-rays. The intensity of a resonance should disappear when $\vec{E}$ is perpendicular to its associated MO vector.

Determination of Molecular Orientation

In principal, it is possible to determine the molecular orientation from the intensity variation of both the π* and σ* resonances with X-ray incidence angle, but it is most convenient and accurate to use the narrow and intense lowest energy π* resonance seen, for example, in the NEXAFS spectra of *p*-6P on oxidized aluminum in Fig.2.9(a).

The angular dependence of the transition matrix elements for a final state orbital have been derived from the X-ray absorption cross section by Stöhr [20]. The intensity dependence of a vector-type resonance (e.g. π* resonance of a benzene ring) can be calculated by

$$I = A[PI^{\parallel} + (1-P)I^{\perp}] \tag{2.3}$$

where P is the degree of polarization of the light from 0 to 1, and A is a constant. $I^{\parallel}$ is the intensity associated with the electric field vector parallel to the polarization vector of the X-rays $\vec{E}^{\parallel}$, as seen in Fig.2.8(a), and is given by

$$I^{\parallel} = \cos^2\theta' \cos^2\alpha + \sin^2\theta' \sin^2\alpha \cos^2\phi + 2\sin\alpha\cos\alpha\sin\theta'\cos\theta'\cos\phi \quad . \tag{2.4a}$$

$I^{\perp}$ is associated with the electric field vector perpendicular to the polarization vector $\vec{\mathrm{E}}^{\perp}$ and is given by

$$I^{\perp} = \sin^2\alpha \sin^2\phi \; . \tag{2.4b}$$

θ' is the angle between the electrical vector parallel to the polarization vector of the light $\vec{\mathrm{E}}^{\parallel}$ and the surface normal, ϕ is the angle between the projection of $\vec{\mathrm{E}}^{\parallel}$ and the MO vector $\vec{O}$ onto the surface, and α is the tilt angle of $\vec{O}$ measured from the surface normal, as seen in Fig.2.8(a). These equations describe the general case where no symmetry considerations of the surface have been made.

On a substrate with twofold symmetry, such as TiO_2(110), the cross-term containing $\cos\phi$ is eliminated when averaging over domains. The above equations then simplify to

$$I^{\parallel} = \cos^2\theta' \cos^2\alpha + \sin^2\theta' \sin^2\alpha \cos^2\phi \tag{2.5a}$$

and

$$I^{\perp} = \sin^2\alpha \sin^2\phi \; . \tag{2.5b}$$

The diagram in Fig.2.8(b) is for the twofold TiO_2(110) substrate when the molecular orbital has no component in the [001] direction, as seen later in Chapter 6.

Simplifying these formulas further, a substrate of threefold or higher symmetry causes the $\cos^2\phi$ term to average to ½ :

$$I^{\parallel} = \cos^2\theta' \cos^2\alpha + \frac{1}{2}\sin^2\theta' \sin^2\alpha \tag{2.6a}$$

and

$$I^{\perp} = \frac{1}{2}\sin^2\alpha \; . \tag{2.6b}$$

To demonstrate how the precise MO tilt angle α can be found from Eqns.2.6, the simple case of an oxidized aluminum surface has been chosen.

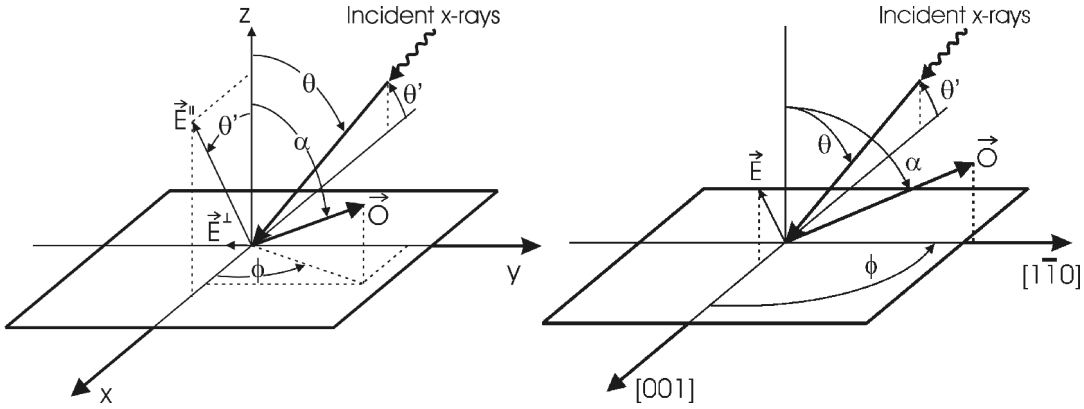

Figure 2.8 ***(a)*** *General NEXAFS Geometry for molecular orbital* ***O*** *tilt angle α.* ***(b)*** *NEXAFS diagram for a 2-fold surface such as TiO_2(110). Here the electrical field vector of the polarized light has a component lying primarily along the the [001] substrate azimuthal direction, labeled the [001] azimuthal geometry. In the [110] azimuthal geometry, the substrate is rotated 90° about the surface normal and the electrical field vector lies primarily along the [1$\underline{1}$0] substrate azimuth. The molecular orbital* ***O*** *is shown pointing exclusively along the [1$\underline{1}$0] substrate azimuth, as found in the needles in Chapter 6.*

α ... molecular orbital **O** tilt angle
θ ... angle of incident x-rays from surface normal
φ ... azimuthal angle between the electric field vector and molecular orbital vector surface projections
$\vec{E}^{\parallel}$ ... electrical field vector parallel to polarization vector of incident x-rays
$\vec{E}^{\perp}$ ... electrical field vector perpendicular to polarization vector of incident x-rays

Consideration of the dipole selection rules and the spectra in Fig.2.9(a) can lead to the orientation of the *p*-6P molecules on oxidized aluminum. In *p*-6P, which consists of six benzene rings in a chain (Chapter 3), the π* MO vectors are perpendicular to the axis of the molecule. At normal incidence (θ = 0°), when the electrical vector $\vec{E}^{\parallel}$ (and polarization vector) of the X-rays is parallel to the surface, the strongest π* resonances are seen, while at glancing incidence (θ = 80°) the π* resonance intensity is strongly reduced. The strong intensity at normal incidence indicates that the MO vectors are mainly parallel to the surface and implies that the axis of the molecule is perpendicular to the surface. A small intensity at glancing incidence would result from either due to a small tilt in the molecules away from the surface normal or because at glancing incidence a small component of $\vec{E}^{\parallel}$ exists in a lateral direction along the surface due to imperfectly polarized X-rays. The X-rays

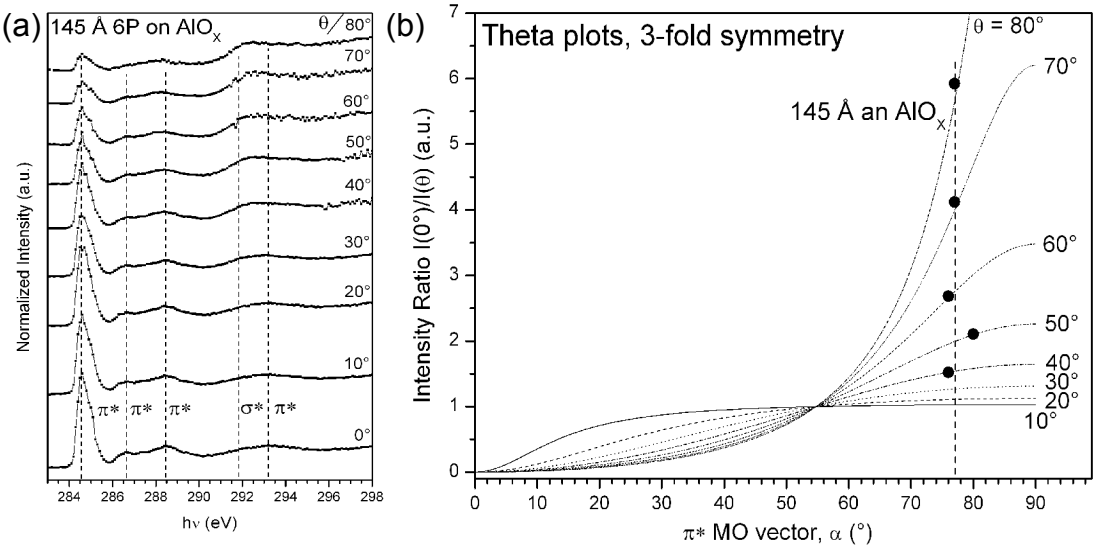

Figure 2.9 *The tilt angle of an ordered species of molecule can be determined by NEXAFS, in this case* p-*6P on a thin layer of oxidized aluminum. The NEXAFS spectra have been divided by a smoothed I_0 and normalized to the front edge of the spectra in* ***(a)****. In* ***(b)*** *the ratio of the intensity at $\theta = 0°$ to the intensities from each angle is compared with theoretical curves obtained from Eqns.2.6 for 3-fold symmetry indicating a MO tilt angle of $\alpha \approx 77 \pm 5°$.*

used here have a polarization of better than 95%.

The tilt angle can be determined from these spectra by the comparing the ratios of a particular peak intensity for different X-ray incident angles with theoretical curves calculated from Eqns.2.6. Fig.2.9(b) displays the intensity ratio $I(\theta = 0°)/I(\theta)$ of the first π* resonance at 284.5 eV calculated for incident angles of $\theta = 10°$ to 80° in steps of 10° versus the MO tilt angle α. By comparing the ratio of the intensities from the data for each of the incident angles with these theoretical intensity curves, it becomes clear that the MO tilt angle is $77 \pm 5°$. The axis of the molecules is perpendicular to the MO vector and is, therefore, tilted 13° from the surface normal. This orientation is near to that which would result from (001) oriented 6P crystallites. The (001) orientation is most commonly reported in XRD studies of films on passive surfaces.

The intensities of the first π* resonances have been measured by integration after background subtraction by a smoothed I_0 curve (explained below) and an additional straight sloped background to simulate the vacuum-edge step. All spectra have been normalized to each other at their preceding edge.

Most NEXAFS studies in the literature are performed for (sub-)monolayer

coverages on threefold (111) surfaces, where averaging simplifies both the experiment and the analysis. But in this study, the anisotropic twofold surface of TiO_2(110) is considered and an attempt to derive geometries beyond the monolayer is made.

NEXAFS works well for homogeneous systems but can be misleading in mixed systems, because it detects all molecular orientations, which will become apparent in Chapter 6. Another limitation is its inability to uniquely determine the MO tilt angle if more than one molecular orientation is present, although a newly developed method which assumes two molecular orientations with a known ratio can determine if the NEXAFS data is consistent with the assumption of two species [22].

Detection Technique

When the X-rays are absorbed, photoholes are created. These holes decay mostly through Auger processes (and photons) and the Auger emission intensity is proportional to the number of holes created.

Three types of electron yield detection exist and are schematically illustrated in Fig.2.10. The simplest is total electron yield (TEY). TEY measures all emitted electrons from the photoemission spectrum. The large inelastically-scattered electron tail adds only to the background of the NEXAFS signal, making signal to background ratio poor. For this reason, partial electron yield (PEY), in which only electrons with energies above a certain pass energy threshold are collected, is used to achieve a higher signal-to-noise ratio, even if the overall signal is lower. The PEY threshold energy should be chosen so that no new XPS peaks enter spectrum as the photon energy is increased. An even higher signal-to-noise ratio is obtained with Auger electron yield (AEY), where a specific auger peak at a specific energy associated with the decay of the core level of interest is monitored. In AEY mode, the energy range can be carefully chosen so that no XPS peaks wander through the energy window.

AEY spectra were measured using the carbon Auger transition at a kinetic energy of 260 eV with a Specs electron energy analyzer with the pass energy determining the KE range monitored. A home-made detector consisting of a channeltron behind two grids was used for the PEY spectra. The first grid was grounded to eliminate electric fields in the chamber from the second grid, which was kept at a negative retarding potential of -200 V.

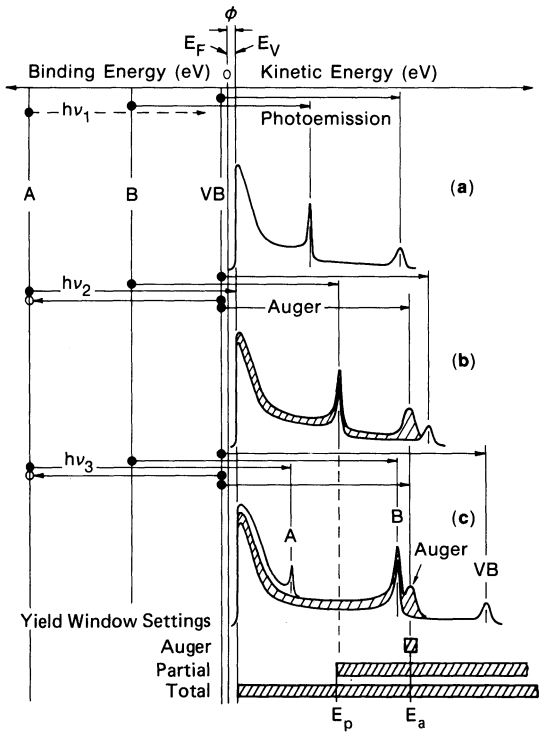

Figure 2.10 *PES Spectra with different cut-offs or energy windows. This schematic demonstrates which electrons of the PES spectrum are collected by different NEXAFS detection methods. (from Stöhr [20])*

C_K NEXAFS spectra which have not undergone background correction can be seen in Fig.2.11. Differences in intensity of individual NEXAFS spectra are caused by changes in intensity of the X-ray source and the particular geometry of the sample. After the spectra have been normalized by setting the front edge equal to one, it can be seen that the signal increases significantly with coverage. The noise seen in the 350 Å spectrum taken at $\theta = 0°$ is due to the auto-range function of the Keithly instrument used.

Background Correction

When NEXAFS spectra are collected, a number of spurious features can be introduced due to absorption in beamline optics, from the substrate and due to changes in intensity of light emitted from the storage ring. In C_K-NEXAFS, the most problematic of these is caused by a loss in X-ray intensity due to carbon absorption on the beamline optics. These features can be seen in all of the uncorrected NEXAFS spectra of Fig.2.1 around photon energies of 284 and 290 eV, as indicated by the arrows. Additionally, the 3 Å *p*-6P films show two peaks due to edge absorption of the potassium impurity present in the TiO_2 substrate. These peaks are not present in

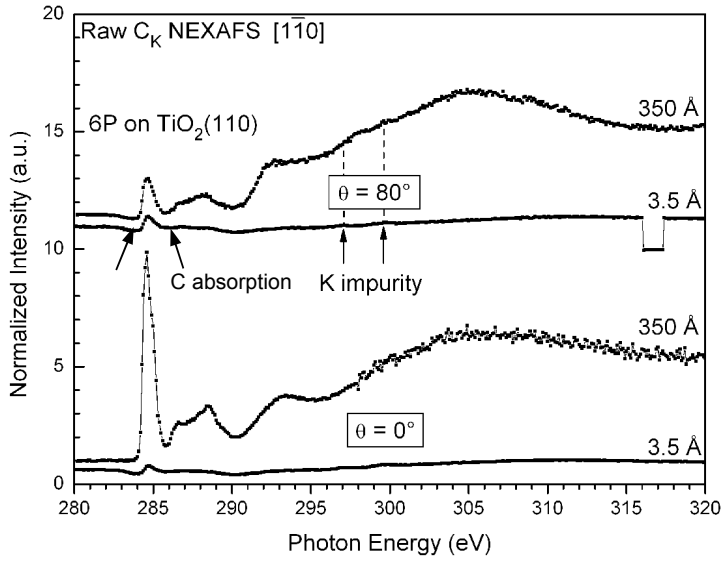

Figure 2.11 *NEXAFS of* p-*6P on TiO_2 before background correction The spectra have been normalized by setting the front edge equal to one.*

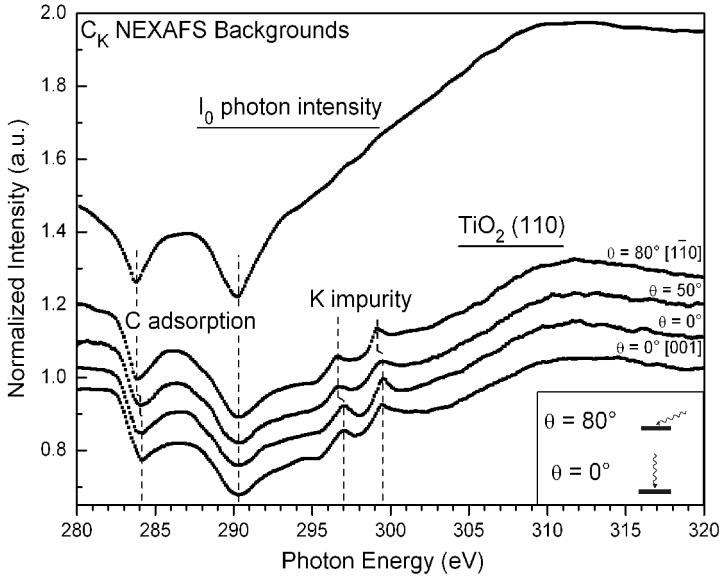

Figure 2.12 *The reference photon intensity I_0 spectrum used for background subtraction for large coverages compared to the reference spectra of a clean TiO_2 (110) substrate used for small coverages. The I_0 spectrum here is the average of many I_0 spectra to reduce noise. All spectra have been smoothed with 7-point adjacent averaging.*

the 350 Å films because of their thickness.

It is important to correct for the carbon absorption structure of the beamline optics through background correction due to its concurrent energy position with the most significant C_K-edge NEXAFS resonance, the first π^* resonance. Additionally, background correction is needed to avoid inauthentic peaks from substrate impurities at low coverages. There are two methods to remove these structures.

For low coverages, the NEXAFS signal can be divided by the signal from the clean TiO_2 substrate (Fig.2.12). Dividing by the substrate corrects for spurious structures due to the detector, the monochromator transmission function (C absorption) and substrate and impurity signal, such as the K impurity.

The substrate spectra in Fig.2.12 were used for coverages of 3 to 9 Å and were smoothed with 7-point adjacent averaging. The structure introduced by C absorption in the beamline optics and the K impurity of the substrate are clearly visible in these spectra. Differences are also observed in the substrate spectra between the different geometries. As the reference spectra are necessarily collected at a different time, often from a different injection, small energy shifts need to be carefully considered.

Shifts between the true and the apparent photon energy occurred between some measurements, most likely attributible to mechanical movements of the monochromator. Some background spectra had to be shifted appropriately to counteract this occurance and to avoid spurious structures. The signal and background spectra were calibrated to the leading edge of the carbon absorption, where there should be no features, before division. No shift in the carbon absorption is expected, as these experiments were carried out within two weeks [23].

As the coverage increases, division by a photon reference intensity I_0 becomes more desirable as the signal from the substrate decreases. The reference intensity was measured as the photocurrent of a gold grid placed between the X-ray source and the sample and has the advantage that it can be obtained at the same time as the spectra themselves and, thus, has no energy shift problems. Division by the I_0 spectrum removes the C absorption features of the beam-line components but does not correct for the substrate impurities. The I_0 spectrum used for the background subtraction of coverages from 35 Å to 180 Å is shown in Fig.2.12. It is the average of many I_0 spectra and has been smoothed by 7 point adjacent averaging.

Although background correction worked for both high coverages with the I_0 and for low coverages with the reference spectra from a clean substrate, it is desirable to use a gold energy reference for each NEXAFS spectrum to assist in the alignment of the background and NEXAFS spectra. Unfortunately, a gold reference was available only for recent NEXAFS experiments. A gold reference also delivers the true energy of the NEXAFS resonances, which cannot be obtained by referencing to the carbon absorption, because shifts in its energy can occur over longer periods in a beamline[23].

Background correction was done in Origin 7.0 with the help of a few Origin C functions written during this thesis found in Appendix A.

2.1.3 Low Energy Electron Diffraction – LEED

Low Energy Electron Diffraction (LEED), one of most widely employed techniques in surface science, is used to characterize the surface crystal lattice constants and check surface lattice order. A monoenergetic beam of electrons, incident on the surface, are elastically diffracted to form an interference pattern. The diffraction pattern formed is a reciprocal representation of the crystal surface lattice,

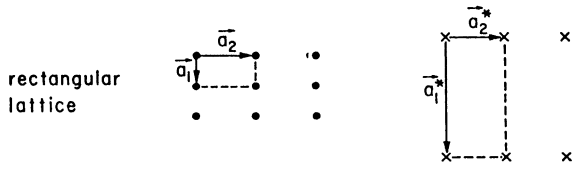

Figure 2.13 *Real and reciprocal lattice representations of a rectangular lattice. (from Van Hove [24])*

as shown for a rectangular lattice in Fig.2.13.

Although LEED studies of *p*-6P have been completed with success [25], no LEED study of the growth of *p*-6P on TiO_2 was possible. The electron beam damaged the molecule quickly, apparent in the destruction of π-band features, even when cooled to LNT (-190°C). LEED was used only to determine the alignment of the substrate azimuth.

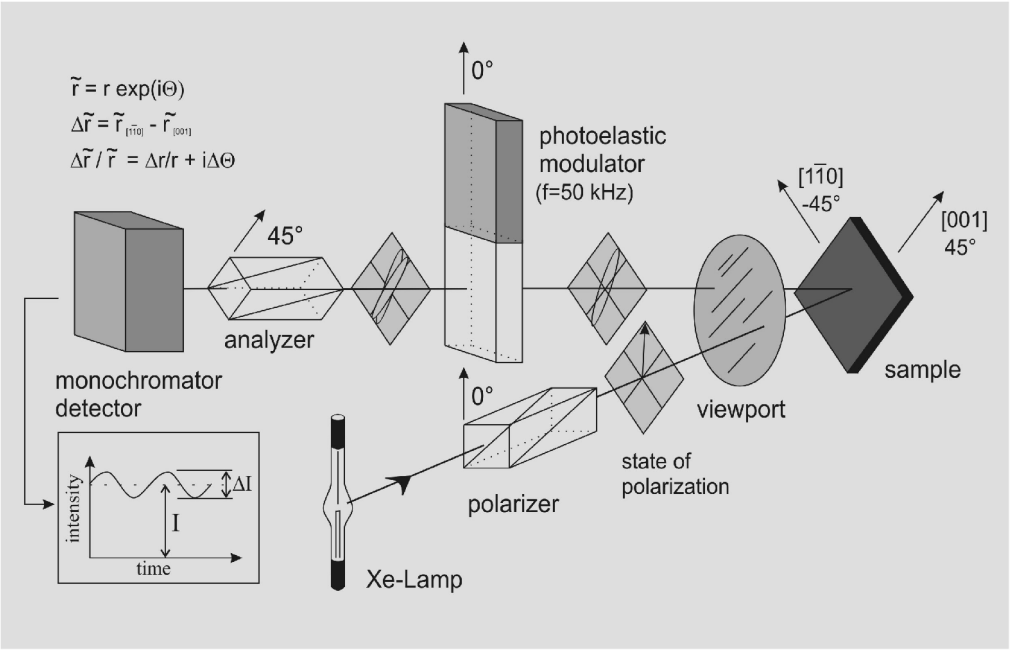

Figure 2.14 *A Schematic of the Reflection Difference Spectroscopy setup. White light from a Xenon lamp, polarized at an angle of 45° to the two orthagonal azimuthal directions of a two-fold surface, is reflected from the sample into a detector designed to measure the difference in intensity ΔI between the reflected light polarized along the two azimuths. In order to detect weak signals, a lock-in amplifier is used in conjunction with a photoelastic modulator. Both incident and reflected light are normal to the sample surface.*

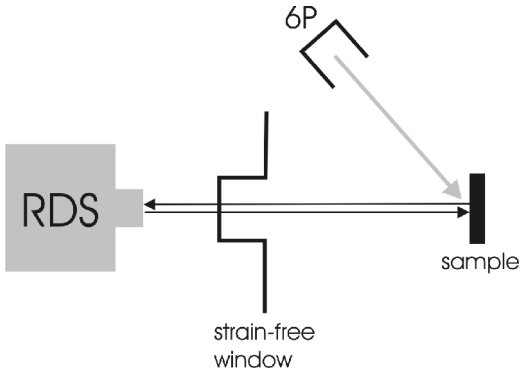

Figure 2.15 *RDS monitoring of the* in-situ *growth of 6P.*

2.1.4 Reflection Difference Spectroscopy – RDS

Reflection Difference Spectroscopy (RDS) measures the difference in optical reflectivity at normal incidence for light polarized along perpendicular directions. It is sensitive to subtle changes of surface electronic structure such as surface morphology, adsorption, and growth. It has been performed successfully with submonolayer sensitivity for the adsorbtion of simple gases such as CO on the anistropic Cu(110)

substrate [26].

During the course of this work RDS was set up on the SCIENTA system to study the *in-situ* growth of 6P films on TiO_2. The RDS experiments were performed in conjunction with Drs. Peter Zeppenfeld, Michael Hohage and Lidong Sun of the Johannes Kepler University, Linz.

RDS proved to be a powerful method in the study of 6P growth on TiO_2(110) despite the high amount of optical anisotropy of the TiO_2 substrate due partially to the anisotropy of the bulk.

RDS interpretation is based on the three-phase model. The difference in reflection along the two substrate azimuths [1$\underline{1}$0] and [001] at the surface depends on the difference between the permittivities in the substrate azimuthal directions (Fig.2.14):

$$\frac{\Delta r}{r} = -\frac{4\pi i d}{\lambda}\frac{\Delta \epsilon_s}{\epsilon_b - \epsilon_a} = -\frac{4\pi i E d}{hc}\frac{\epsilon_{[1\bar{1}0]} - \epsilon_{[001]}}{\epsilon_b - 1} \qquad (2.7)$$

where ϵ_b is the permittivity of the bulk and ϵ_a of air or vacuum, $\Delta\epsilon_s$ the difference between the permittivities of the surface along the two principal substrate azimuths and d is the thickness of the surface.

As shown in Fig.2.14, white light from a Xenon lamp, polarized at an angle of 45° to the two orthagonal azimuthal directions of a two-fold surface, is reflected from the sample into the detector. Changes in optical anisotropy on adsorption lead to elliptically polarized light which, via the photoelastic modulator, can be analyzed into a difference in the reflectivity in the two principle azimuthal directions as a function of photon energy. In order to detect the weak RDS signals, a lock-in amplifier is used in conjunction with the photoelastic modulator. An RDS spectrum could be measured in a matter of minutes and, thus, with an appropriately low growth rate, spectra could be measured continuously during growth (Fig.2.15).

2.1.5 Experimental System SCIENTA

Most experiments were done in the SCIENTA system located in Graz (Fig.2.16). The SCIENTA system is equipped with LEED, a quadrapole mass

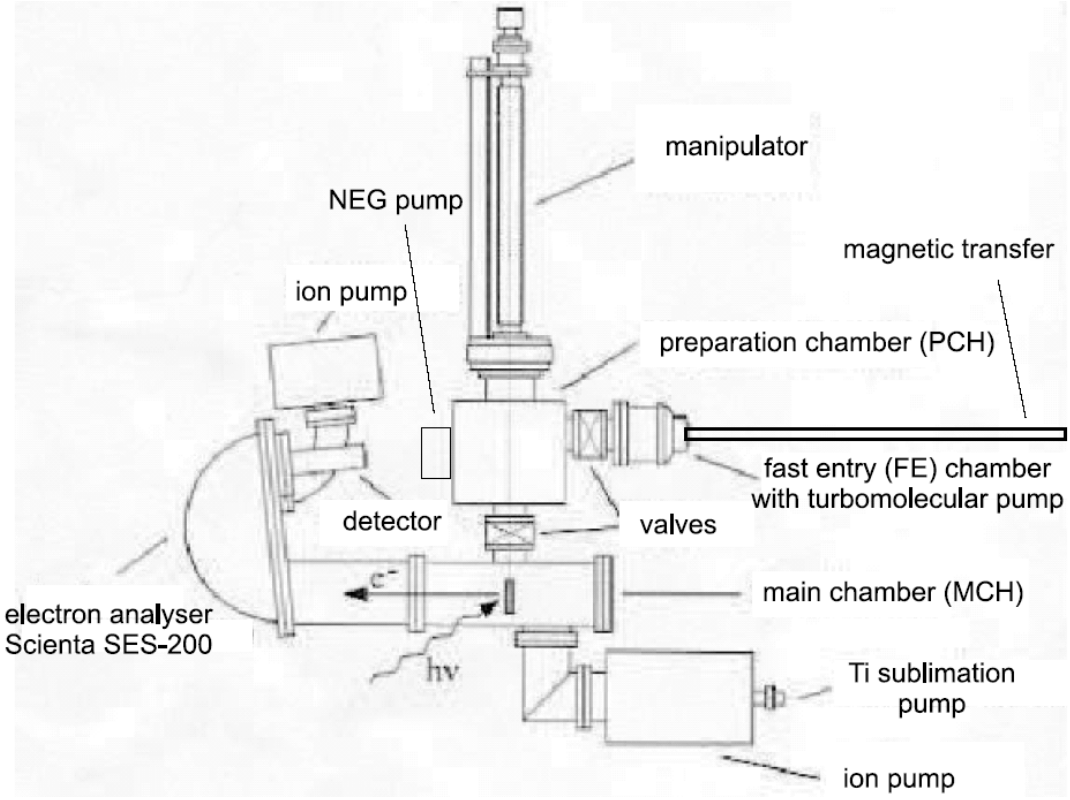

Figure 2.16 *SCIENTA experimental system.*

spectrometer, an ion sputter gun, a quartz microbalance, electron-beam heating and a molecular evaporator in the preparation chamber and a Scienta SES-200 hemispherical electron energy analyzer, a He-lamp and an X-ray source with Mg and Al anodes in the main chamber.

The SCIENTA system allows sample rotation around the normal of the experimental plane formed by the incident photons and emitted electrons, 45° apart from each other. The sample could also be rotated about its surface normal to place either the TiO_2[001] or [1$\underline{1}$0] azimuthal direction parallel to the experimental plane.

The quartz microbalance was used to determine the evaporation rate and, consequently, the coverages of *p*-6P on TiO_2. It was set for a density of 1.0 g/cc for improved sensitivity. The coverages given were obtained through division by the accepted *p*-6P solid-state density of 1.3 g/cc. These coverages are in agreement with the amount of material seen in the AFM (see below) images.

2.2 *ex-situ* Investigation

Two *ex-situ* techniques were used in the study of the crystal structure and morphology of *p*-6P grown on TiO_2. For measurement by *ex-situ* techniques, the samples were allowed to come to room temperature and removed from UHV.

2.2.1 X-ray Diffraction – XRD

X-ray Diffraction (XRD) is a widely used tool to determine crystal structures. It is sensitive only to ordered structures, as with LEED; unordered structures appear only as background.

XRD data was obtained at the Technical University, Graz by Dr. Roland Resel and Ondrej Lengyel using a Philips X'pert system and its Cr K_α-source, described in [27]. The Stereogram software package [28] was used for the crystallographic analysis, based on the crystal structure of *p*-6P with a = 8.091 Å, b= 5.564 Å, c = 26.24 Å and β = 98.17° [29].

XRD relies on Bragg's law (the scalar condition for constructive interference in X-ray diffraction)

$$n\lambda = 2d_{HKL}\sin\Theta\,, \tag{2.8}$$

which associates the interplanar spacing of lattice planes d_{HKL} in crystal with the wavelength of incident radiation λ and the angle at which constructive interference is observed Θ.

Two types of XRD measurements were performed during this thesis, the so-called Θ/2Θ-plot and pole figure. The Θ/2Θ-plot is used to determine the net planes parallel to a well-defined and aligned substrate. Only net planes that are symmetrically oriented with respect to the incident beam and detector position fulfill Bragg condition.

The pole figure technique is used to determine the orientational distribution of crystallites in an epitaxial thin film and shows whether crystallites are well aligned. Its representation is a stereographic projection of points on a hemisphere onto a plane bound by the hemisphere equator.

2.2.2 Atomic Force Microscopy – AFM

Atomic Force Microscopy (AFM) measurements are used to study surface morphology. AFM is a direct probe of the surface using a chemically sharpened silicon tip, possibly with a carbon whisker attached for better resolution.

The AFM measurements were performed on two different Digital Instruments Nanoscope IIIa instruments. The measurements were performed in cooperation with Dr. Christian Teichert and Gregor Hlawacek at the Montan University, Leoben, and with Dr. Joachim Krenn at the Karl-Franzens University, Graz.

AFM measurements on *p*-6P were done in tapping mode, where the tip is only briefly in contact with the sample, therefore reducing damage to the molecular layers. In tapping mode, also known as intermittent mode, the tip of the AFM is driven near a strong, preferably its strongest resonant frequency. The maximum amplitude is dampened and there is a phase shift when the tip begins to contact the surface. The tip is driven to stay near resonant frequency, producing the height information.

The silicon tip has a diameter around 25 nm. To improve the resolution, tips with a carbon whisker grown on the conventional silicon tip can be used. The carbon whisker has a tip diameter around 5 nm.

2.3 Growth in three temperature ranges

Thin films of 6P were grown in three different substrate temperature ranges to study the effect that the temperature has on the growth of the film: liquid nitrogen temperature (LNT, -190°C), room temperature (RT, 0 to 40°C) and high temperature (HT, 100 to 150°C).

Growth on a substrate at liquid nitrogen temperature (LNT) was achieved by cooling the manipulator by adding liquid nitrogen (-196°C). The thermocouple showed a temperature of -180°C. The actual temperature of the sample was between -196°C and -185°C.

What is labeled growth on a room temperature substrate (RT) was a range of temperatures from 0°C to 40°C. Samples could take over an hour to cool to 40°C after annealing. Adding some liquid nitrogen to the cryostat could speed up cooling, but

sometimes resulted in temperatures somewhat below ambient RT. Experiments were conducted only when the sample had cooled to $\leq 40°C \pm 10°C$.

Growth on a high temperature (HT) substrate was achieved by heating the sample plate with the filament used for e-beam heating located on the opposite side from the crystal. No high voltage was applied to the sample plate during HT growth. The thermocouple indicated a temperature of 100°C to 150°C on the sample plate, with a filament current of 1.2 to 1.4 A, depending on the particular experiment described below. Adequate time was allowed for the sample plate, sample head and sample to come to thermal equilibrium.

The thermocouple was mounted either to the sample plate or under a spring holding the sample plate to the manipulator head. Measurements made under the spring were calibrated to those made directly on the sample plate. Given temperatures correspond to those measured on the sample plate.

Chapter 3

Experimental System

3.1 The Substrate – TiO_2

Titanium dioxide is an optically clear oxide that is found naturally as an insulator (optical band gap 3 eV) but can be made conductive by doping or heat treatment in UHV. The TiO_2(110) surface of the rutile structure is highly anisotropic and can be used as an anisotropic template for organic crystalline film growth, as has been achieved with other substrates [30],[31]. Diebold calls it the 'best characterized' prototypical metal oxide surface but remarks that its atomic level structure is complex [32].

TiO_2 becomes n-doped by oxygen removal through cycles of sputtering and annealing in UHV or by annealing above 800°C in UHV. The oxygen removal results in defect states in the band gap, generating resistivities from 108 Ω-cm for a slightly reduced, light blue crystal to 9 Ω-cm for a heavily reduced dark blue crystal. Roughening of the surface increases with the number of treatment cycles. [32] Lightly reduced crystals are sufficiently conductive for the the electron spectroscopic methods described in Chapter 2 which required conductivity. The polished TiO_2(110) crystals used in this study were purchased from Pi-Kem Ltd., England.

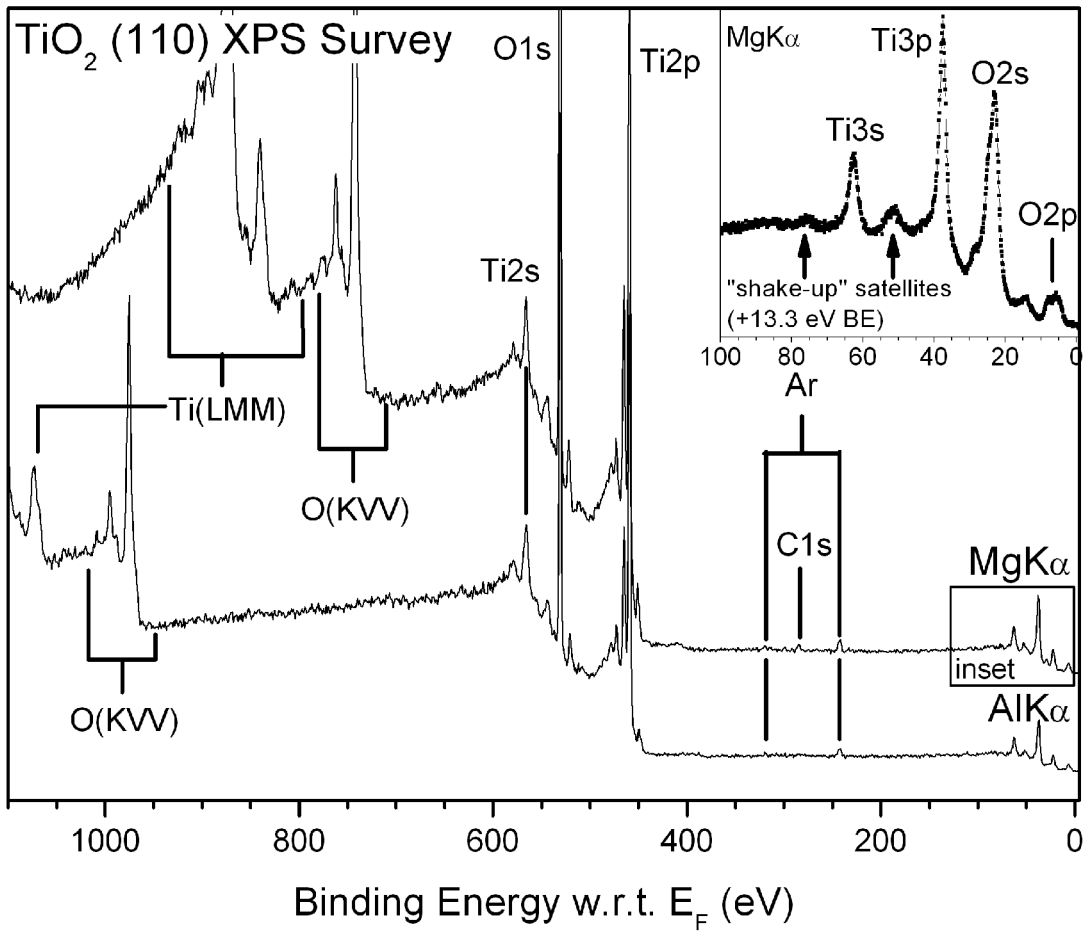

Figure 3.1 *XPS survey of sputtered and annealed TiO_2(110). XPS peaks are identified by their corresponding orbitals, Auger electron peaks are labeled with the transitions involved.*

As can be seen in the XPS survey of TiO_2 in Fig.3.1, a small amount of argon from sputtering remains in the surface even after annealing at 700°C for 30 minutes, which is a well-documented phenomenon [32]. Carbon also contaminates this particular surface but could be removed fully by subsequent sputtering.

The major contaminate found in commercially available TiO_2 crystals, potassium [32], is not seen due to its low cross section at these X-ray energies. XPS at lower photon energies (not shown) performed at BESSY II show that potassium does indeed exist in the crystals used for these experiments, and it is seen in the NEXAFS spectra as two peaks around a photon energy of 297 and 299 eV, corresponding to the K_{2p} peaks at binding energies (BE) of 293 and 296 eV. No other contaminants were found in the crystals used during this study.

Preparation

Since in is not possible to spot-weld a thermocouple directly on the TiO_2 crystal, the temperature was monitored with a thermocouple spot-welded directly to the wires holding the crystal to the sample plate or under a spring about 0.5 cm from the sample calibrated to reflect the measurement made directly on the plate.

The samples were sputtered for 10-15 minutes with Ar^+ ions with an acceleration voltage of 1 kV and an Ar partial pressure of $<2x10^{-6}$ mbar yielding a sample current of 3.4 μA to ground with approximately $1.8x10^{13}$ $Ar^+/s\text{-}cm^2$ incident on the surface.

The subsequent anneal was typically completed at 700°C for 15 - 20 minutes at 700°C (U_{sample} = + 700 V, $i_{filament}$ = 2 A, i_{sample} = 42 mA) for sample plates with no window (typically used), which resulted in an evenly heated sample, or an apparent 500°C for sample plates with a window (as used for the two AFM samples in Chapter 6). The use of sample plates with a window was discontinued after two months of experiments due to the highly irregular appearance of the crystals with regard to color, indicating uneven reduction, and the crystal's tendency to crack due to the extremes of direct e-beam heating (Fig.3.2). The measurements on samples prepared on cracked substrates are the AFM, XRD and PL of a 350 Å, the AFM of a 35 Å coverage and one heating series of a 10 Å coverage, all evaporated onto a RT substrate.

Several cycles of sputtering and annealing are required to clean the crystal and restore order to its surface, as required with most samples studied in UHV. These cycles have a second purpose with TiO_2, specifically the reduction of the crystal through missing-oxygen defects resulting in its conductivity.

The oxygen defects, which are created at the surface through their preferential sputtering (1.7 O atoms per Ar^+ ion as opposed to 1.3 Ti atoms), diffuse into the bulk upon annealing in UHV [32]. Fig.3.2 illustrates how the large amount of these defects states created during sputtering, seen just below the Fermi level E_F at 0.7 eV, diffuse into the bulk upon annealing at 700°C in UHV, evident in the reduction of this peak.

Sputter induced damage is also easily removed from the surface by annealing, as seen in the increase in angular differences in the O_{2p} band between 3 and 9 eV BE with respect to E_F after annealing. In particular, strong azimuthal differences,

(a) highly reduced

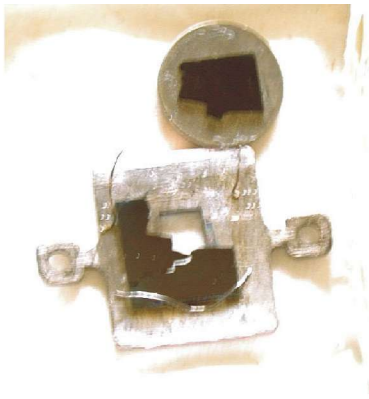

(b) highly reduced

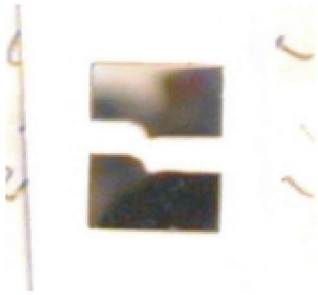

(c) New and heavily reduced crystals

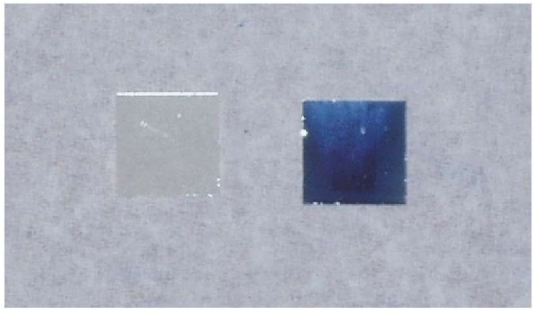

(d) New and lightly reduced crystals

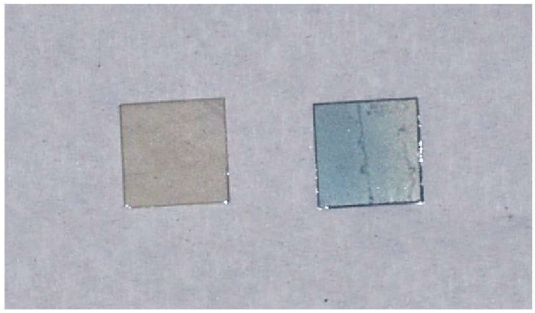

(e) RDS spot on crystal at 25°C

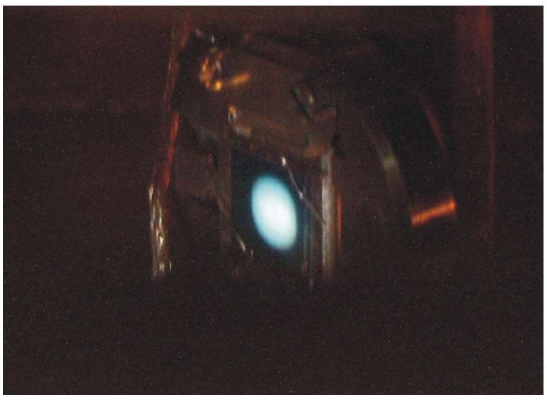

(f) RDS spot on crystal at 700°C

Figure 3.2 (a) *This TiO_2(110) crystal was cracked by the e-beam heater due to a window in its mounting plate. The 350 Å* p-*6P film which produced the AFM images (Figs. 6.9-11), XRD (Fig.6.12) and PL (Fig.6.18) results in Chapter 6 is found on this crystal.* ***(b)*** *This crystal was also cracked by e-beam heating and holds the 35 Å 6P film in the AFM images of Fig. 6.9.* ***(c),(d)*** *A comparison of new crystals with a heavily reduced crystal not used in these experiments and a lightly reduced crystal on which the >300 Å* p-*6P film used for the NEXAFS spectra of Fig.3.8 and 6.14(c) was deposited.* ***(e),(f)*** *Lightly reduced TiO_2(110) shows its blue color at room temperature in the white light of the RDS lamp. It takes on a green color at annealing temperature (700°C).*

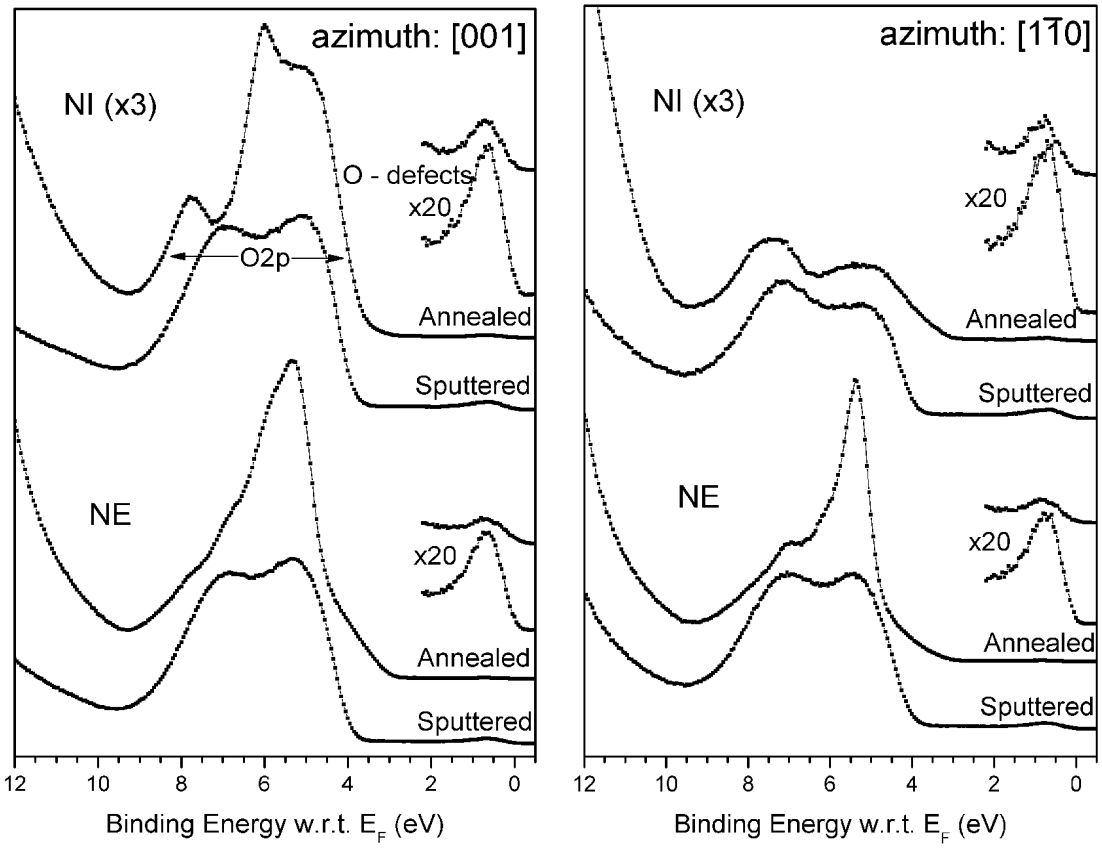

Figure 3.3 *The UPS spectra of the TiO_2 valence band is shown here in the two principle azimuths after sputtering and after subsequent annealing in UHV at 700°C. The oxygen defect states have been magnified by twenty to reveal their concentration on the surface before and after annealing. Spectra taken in normal incidence (NI) geometry have been multiplied by 3. NE is normal emission geometry.*

particularly pronounced in normal incidence (NI) geometry, become apparent. The band gap is illustrated by the absence of electronic states starting at 3 eV BE below E_F and continuing to the defect state just below E_F in Fig.3.3.

Surface and Electronic Structure

The highly anisotropic (1x1) surface reconstruction of TiO_2(110) (of the rutile structure: tetragonal, $D_{4h}^{14} - P4_2/mnm$, a = b = 4.584 Å, c = 2.953 Å) consists of parallel rows of titanium atoms between rows of bridging oxygen atoms protruding from the surface, as depicted in the ball and stick model of Fig.3.4(b). The oxygen rows are separated by 6.5 Å and run parallel to the TiO_2[001] direction. In the STM of Fig.3.4(a) the protruding oxygen rows are seen as dark stripes between the clearly

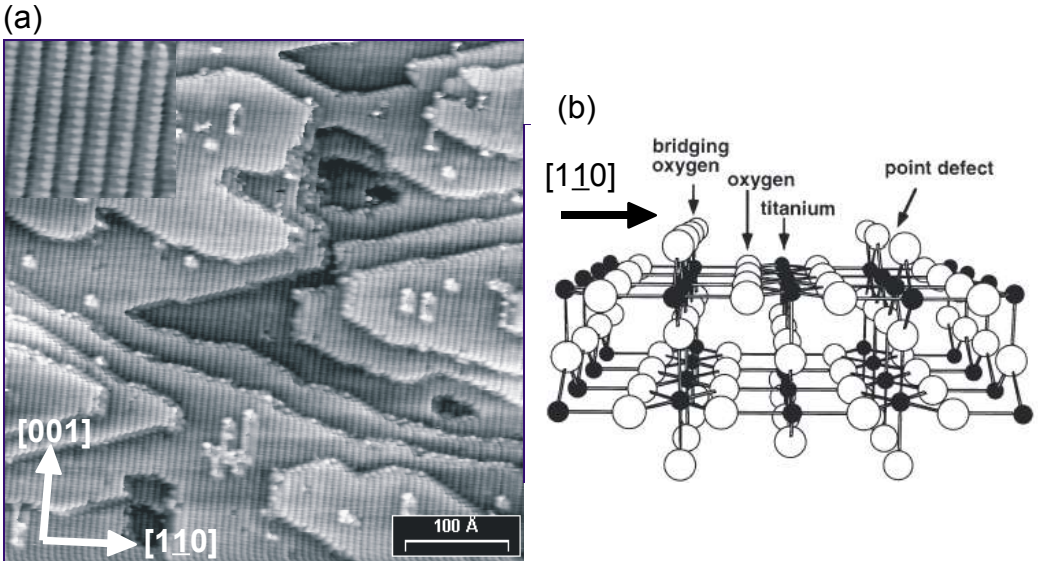

Figure 3.4 ***(a)*** *STM image of TiO_2(110) with close view of the oxygen rows in the inset with labeled substrate azimuths.* ***(b)*** *Ball-and-stick model of the surface. The [001] azimuthal direction points into the page.*

visible bright rows of titanium atoms. [32] The substrate anisotropy is visible in the UPS of a clean sample (Fig.3.5), manifested in the drastic change in relative peak intensity within the O_{2p} band with changing incident and emission angles despite the large analyzer acceptance angle of 16° and the use of nonpolarized light.

Also visible in the STM image are the 3.2 Å high step edges, which run predominantly parallel to the TiO_2[001] and [1$\underline{1}$1] directions, the latter of which are clearly observed in Fig.3.4(a) at ± 24.5° off the [1$\underline{1}$0] substrate azimuthal direction. Terrace size increases with annealing temperature [32],[33]. The step edges are associated with a decrease in coordination number, often accompanied by increased reactivity [32]. Surface chemistry is also affected by the several possible reconstructions of the surface and point defects in the oxygen rows, whose oxygen atoms are thought to be removed quite easily.

Earlier studies have shown that the amount of reconstruction and the step density increases with the number of sputtering and annealing cycles. Diebold suggests using light blue crystals for (1x1)-terminated surfaces, as dark crystals form more complex structures, especially with oxygen treatment during annealing.

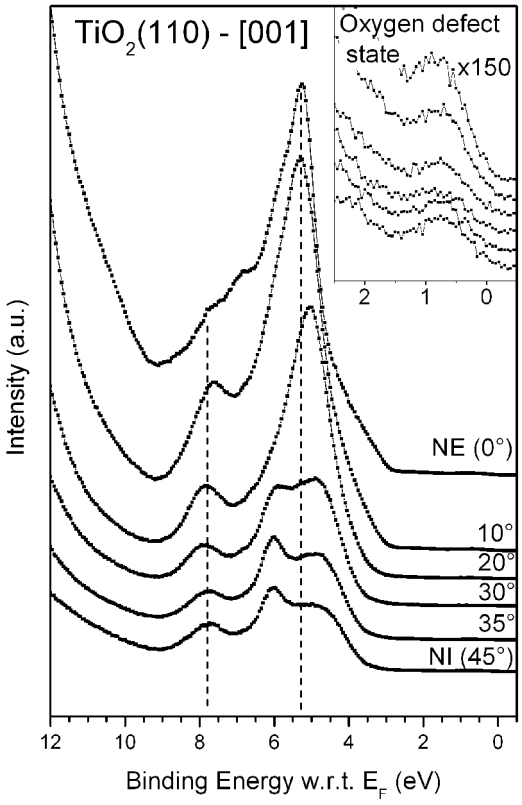

Figure 3.5 *The oxygen 2*p *states in the valence band of TiO_2 change remarkably with emission and incident light angle, considering the large acceptance angle of the analyzer. This behavior suggests a highly ordered surface. These spectra were taken in the [001] azimuthal geometry.*

The concentration of surface reconstructions and step density likely increased over the lifetime of a crystal in this study, yet the *p*-6P films grown seemed not to show a growth dependency on the amount of reduction of the TiO_2, as indicated by its color.

LEED, which was used to determine if a new crystal had reached the desired conductivity and to align the substrate azimuths, also offers a verification of the short range order of the surface in the clarity of the diffraction spots.

3.2 The Molecule – Sexiphenyl

para-Sexiphenyl (*p*-6P, $C_{36}H_{26}$) is a π-conjugated organic molecule consisting of six phenyl rings and is considered to be a 'rigid', 'rod-like' molecule (Fig.3.6(b)). *p*-6P was used due to its technological relevance as the active material in blue light emitting diodes and its utility as a model for longer chain-like molecules, e.g. poly-*para*-phenyl (PPP). 6P is available for purchase as a pure substance and can be easily

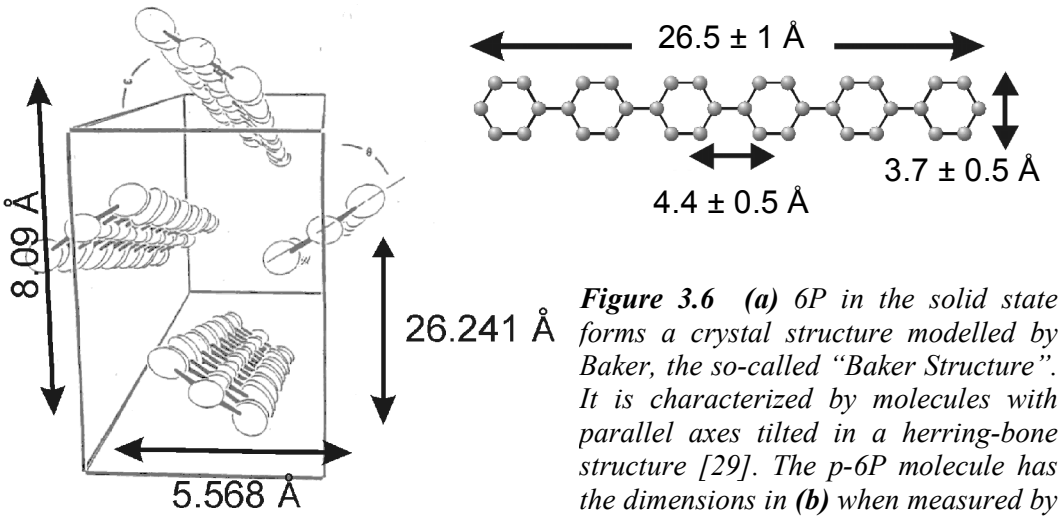

Figure 3.6 ***(a)*** *6P in the solid state forms a crystal structure modelled by Baker, the so-called "Baker Structure". It is characterized by molecules with parallel axes tilted in a herring-bone structure [29]. The p-6P molecule has the dimensions in* ***(b)*** *when measured by STM on Nickel [30].*

grown on a substrate by physical vapor deposition in UHV.

The *p*-6P used in these experiments was obtained from Tokyo Chemical Industry Co., Ltd., Japan. Typical cleaning procedure was to heat the *p*-6P for at least half an hour in UHV with a current through the heating wire higher than that normally used for evaporation. The *p*-6P sublimes in UHV around 240°C and was deposited on the surface by physical vapor deposition at rates between 0.5 and 4 Å/min (typically ~1 Å/min). Pressure remained in the 10^{-10} mbar range during film growth.

Geometric Structure

An individual *p*-6P molecule has the dimensions of 26.5 ± 1 Å x 3.7 ± 0.5 Å with an inter-ring spacing of 4.4 ± 0.5 Å when measured by STM on an oxygen passivated Nickel surface [30]. In the solid state, *p*-6P packs in a herring-bone structure in which all molecular axes are parallel and the molecular planes non-parallel. Although the phenyl rings are not co-planar in the gas phase, it is reported to be 'on-average' planar in the solid state [29],[34]. Recently, however, Ivanco *et al*. [3] have shown that both planar and twisted molecules can be obtained in the solid state, depending on growth conditions, as evidenced by UPS. This issue is one of the focal points of the present study. The room-temperature crystal structure belongs to the space group $P2_1/c$ and has the lattice constants a = 26.241 Å, b = 5.568 Å, c = 8.091 Å and β=98.17° [29].

Baker *et al*. note that, based upon its crystal structure, *p*-6P does not seem to be a good model for PPP [29]. This assertion, however, is contested by Seki *et al*., who have documented the electronic structure of *p*-6P and found that it suggests otherwise [34],[35].

Valence Band Electronic Structure

Fig.3.7(a) shows the similarity between the UPS spectra of *p*-6P, biphenyl (2P) with two phenyl rings and benzene. Four molecular emission bands can be seen. The band closest to E_F is commonly called the π-band and displays the greatest differences between benzene, biphenyl and sexiphenyl. The frontier orbital of the π-band, called the highest occupied molecular orbital (HOMO), is the most important band for the electrical properties of the *p*-6P crystal. Its position with respect to the vacuum level determines the ionization potential (IP) of the molecules, critical for charge injection.

The two degenerate e_{1g} orbitals of benzene (Fig.3.7(b)) are responsible for the π-band in the UPS spectra. This orbital delocalizes to a certain extent over the entire molecule when further phenyl rings are added, causing an energy split in these orbitals due to the Pauli exclusion principle. Fig.3.7(c) shows how the e_{1g} orbitals of benzene splits into four orbitals in biphenyl, one bonding orbital at higher BE, one antibonding orbital at lower BE and two degenerate nonbonding orbitals. Likewise, in *p*-6P this orbital splits into three nondegenerate bonding orbitals, three nondegenerate antibonding orbitals and six degenerate nonbonding orbitals.

The width of the π-band is proportional to the degree of overlap of the e_{1g} orbitals on neighboring rings. The degree of overlap can be controlled by the conformation of the molecule, or twist angle of the rings with respect to one another [3],[36]. Theoretical calculations indicate that a range of ionization potentials (IP) of 0.5 eV exist for phenyl tilt angles from 0° to 50° in the gas phase [37]. On Al(111) the IP could be shifted over a range of 0.7 eV, depending on whether the film contained planar standing molecules, as in the case of HT growth, or twisted lying molecules, as for RT and LNT growth [3]. As will be seen in Chapters 4 through 6, a tuning of the IP could also be achieved for *p*-6P on TiO_2(110), resulting in differences in IP of up to 0.6 eV depending on growth conditions.

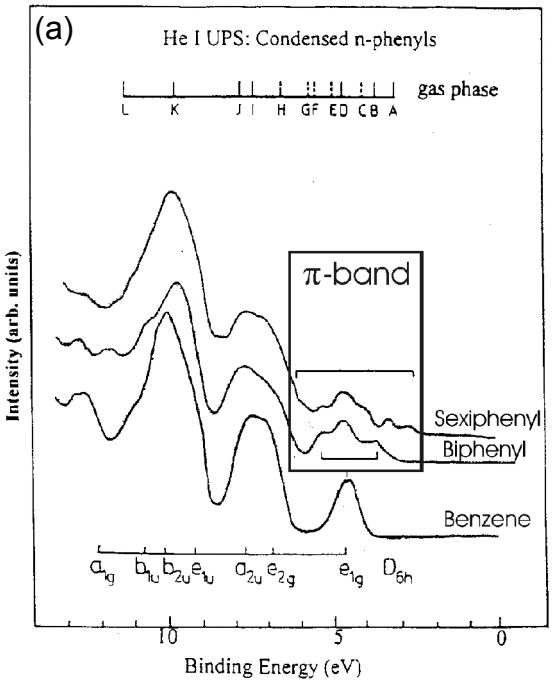

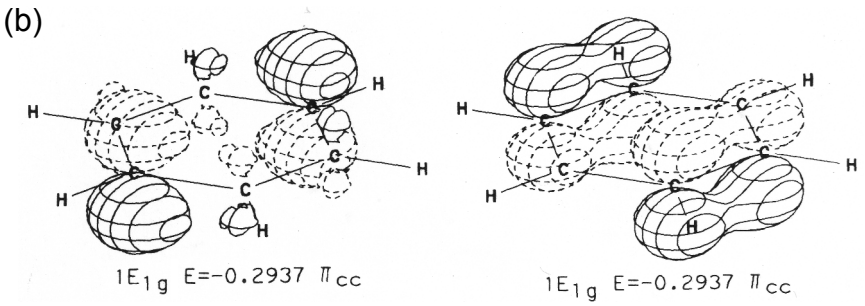

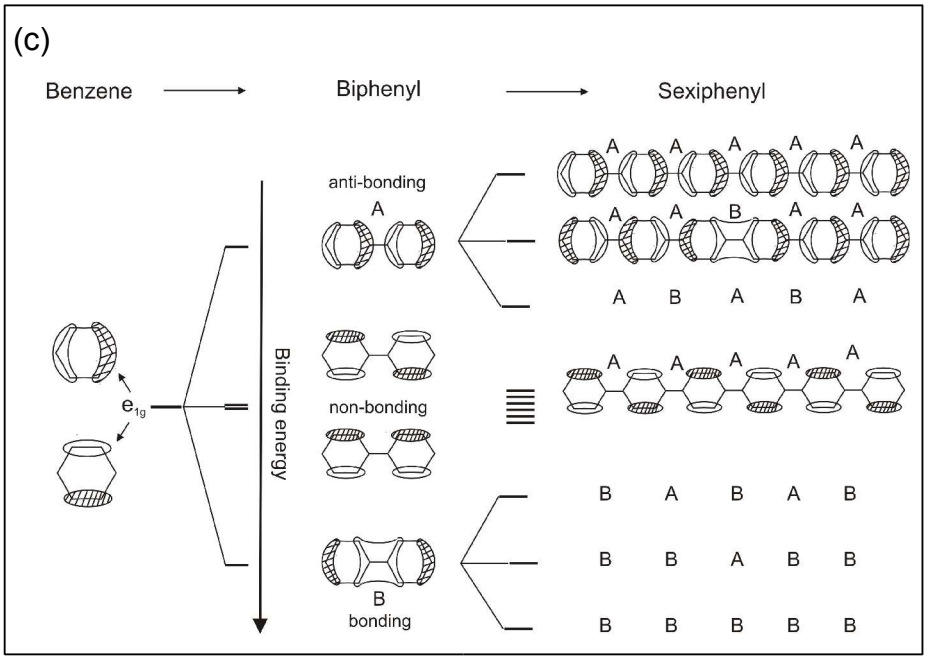

Figure 3.7 ***(a)*** *The UPS of benzene, biphenyl and sexiphenyl.* ***(b)*** *The e_{1g} orbital, the HOMO of benzene [21].* ***(c)*** *Overlap of the e_{1g} orbitals in* p-*6P leads to splitting in the* ***π****-band, creating three interring bonding orbitals at higher BE, three antibonding orbitals at lower BE and six degenerate nonbonding π-orbitals. ((a) & (c) from Ramsey* et al. *[36])*

Unoccupied States

A prerequisite to the determination of molecular orientation with NEXAFS is a clear assignment of orbitals to the resonances seen in the spectra. Since no study assigning *p*-6P NEXAFS resonances can be found in the literature, the attempt to do so here will rely on comparison to NEXAFS and ISEELS spectra of benzene. Such an attempt can be made based on the building-block principle: the NEXAFS resonances of a complex molecule are thought to correspond to the resonances of its constituent parts due to the localization of the excited state around the core hole [20]. Indeed, the NEXAFS resonances of biphenyl closely resemble those of benzene [38].

The *p*-6P spectra in Fig.3.8 are also similar to the benzene spectra yet display a much more complicated structure, particularly from 287 to 290 eV excitation energy. This partial breakdown in the building block principle has been explained by Oji *et al*., through *ab initio* molecular orbital (MO) calculations, as a core-hole effect with additional effect by the site-dependent core ionization energy [39]. They maintain that transitions to the same orbital can, in some cases, create multiple features in the spectrum and other transitions to two separate MOs can contribute to the same feature. Koller *et al*. [40] have observed both initial and final state effects for bithiophene in comparison to the monomer thiophene.

By measuring NEXAFS spectra of a well-defined layer of *p*-6P in which the orientation of the molecules is known, experimental geometries can be used which select resonances with π* character, as in the top spectrum of Fig.3.8, or with σ* character, as in the bottom spectrum. Even though some differences exist between the spectra of *p*-6P and benzene, an attempt can be made to identify some of the *p*-6P resonances, at least in terms of their basic character. All features observed and there assignments are given in Table 3.1.

The first resonance in benzene π*(I) is universally assigned to a transition to the LUMO, $C_{1s}\rightarrow\pi^*(e_{2u})$ transition [41],[42],[43],[44],[45],[46] (benzene $\pi^*(e_{2u})$ orbitals in Fig.3.9). The transition labeled π*(A) seen in *p*-6P can also be unambiguously assigned to the $C_{1s}\rightarrow\pi^*(e_{2u})$ transition as it is expected to be the lowest energy unoccupied MO. The asymmetry of the π*(I) peak of benzene has been explained as vibrational effects [47], but the π*(A) peak in *p*-6P appears to consist of

Feature	Assignment Relative energy (in eV)		
	Benzene		*p*-6P
	Solid	Gas	Solid
π*(A) / π*(I)	π*(e_{2u}) 0	π*(e_{2u}) 0	π*(e_{2u}) 0
π*(A')			π*(e_{2u}) 0.4
σ*(i)		3s Rydberg + σ*(a_1/C-H) 2.0	
π*(B)			2.2
σ*(ii)	3s Rydberg + σ*(C-H) 2.4	3p 2.9	
π*(C)			2.8
σ*(a)			σ*(C-H) + more 3.4
π*(II)	π*(b_{2g}) + shake-up 3.8	σ*(a_1/C-H) + shake-up 3.9	
π*(D)			π*(b_{2g})? 4.2
σ*(iii)	σ*(C-H) 5.2	σ*(a_1/C-H) + continuum 5.2	
σ*(b)			σ*(C-C) 8.0
σ*(iv)	σ*(C-C) + shake-up 8.4	σ*(C-C) + shake-up 8.3	
π*(D)			σ*(C-C) 8.5

Table 3.1 Assignment of NEXAFS Resonances
Benzene resonances have been assigned from several sources listed in the text. The energy position of each resonance has been referenced to the first resonance.

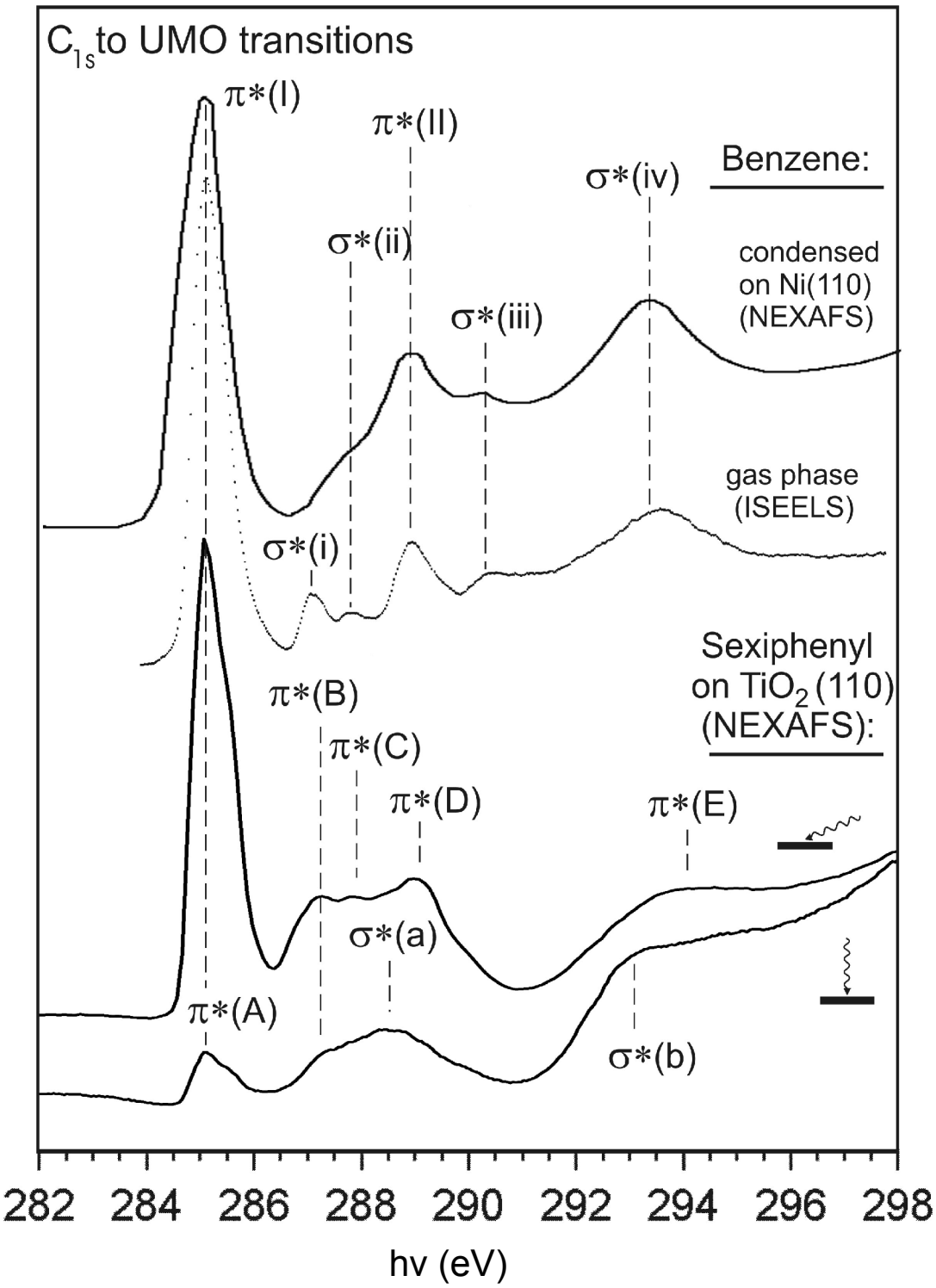

Figure 3.8 *Comparison of NEXAFS and ISEELS of benzene with NEXAFS of* p-*6P. The NEXAFS spectrum of benzene is from Menzel* et al. *[41], the ISEELS from Duflot* et al. *[42] and the NEXAFS spectra are recently obtained results of a* p-*6P film grown at 0°C. The benzene spectra have been shifted so that the first transition is at the same energy as that measured for* p-*6P, which was confirmed by a gold reference. The* p-*6P spectra have been normalized at the preceding edge.*

at least two and possibly more directly neighboring peaks, as can also be observed in the NEXAFS spectra in Fig.3.8 as a shoulder on the high energy side (π*(A')), which is difficult to explain only by vibrations. The ISEELS spectrum of benzene has the resolution to resolve this peak if it was present in benzene, therefore, it is assigned as being unique to 6P. While clearly of the same character, its origin is, as yet, unknown, although investigation is underway to determine if this originates from an initial state effect (e.g. site-dependent C_{1s} ionization energy) or final state effects.

The first π* resonance presents itself as the most useful in analysis of molecular tilt angle due to its large size and distance from other resonances.

Due to the complex nature of the *p*-6P spectra in the region between the first transition at 285.3 eV photon energy and a photon energy of about 291 eV, correlating peaks in benzene with those in *p*-6P is difficult without curve fitting. Nevertheless, the features have been labeled with either π* or σ* character, depending on their behavior with X-ray incidence angle, and a brief description of these features will be given.

At first glance, one could correlate the peak labeled π*(B) in *p*-6P with that labeled σ*(i) in the ISEELS of benzene, which has been assigned to a $C_{1s}\rightarrow$3s Rydberg + σ*(a_1/C-H) transition due to its weakness in solid-state benzene. This cannot be the case in *p*-6P, as this peak clearly displays π* character in its behavior with X-ray incident angle and is prominent in the solid state.

The σ*(i) peak of the gas phase benzene is not observed in the solid state of benzene. σ*(ii) of the solid state has been attributed to a shifted σ*(i) gas-phase peak [41] and does not seem to be present in solid *p*-6P. A shoulder was observed in benzene on Ni(110) by Ramsey *et al*. at the position of σ*(i) and assigned to an additional transition to a mixed character 3s Rydberg + σ*(C-H) orbital [48]. As with *p*-6P, a peak is seen at this position in biphenyl condensed on Ni(110) [38].

Peak σ*(ii) in the gas phase spectrum is generally assigned to 3p Rydberg excitations, while the shoulder at the same position in condensed benzene is considered to belong to a mixed-character $C_{1s}\rightarrow$3s Rydberg + σ*(C-H) transition in the literature. A peak at the position of this shoulder is seen in both the Auger yield NEXAFS of benzene [41], with the same assignment as the shoulder, and in partial yield spectra of biphenyl [48].

It is likely that the π*(II) resonance in benzene, attributed to a π*(b_{2g}) transition

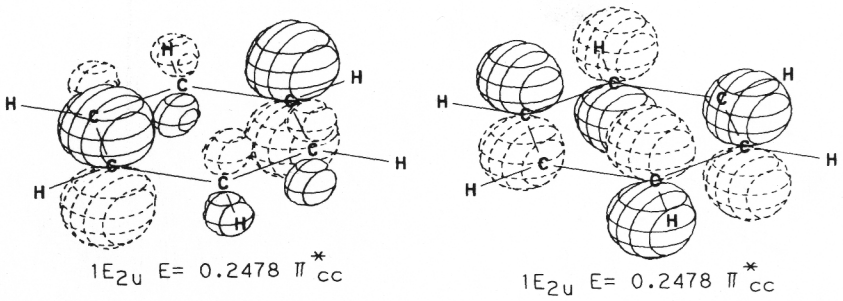

Figure 3.9 *The π*(e_{2u}) orbitals of benzene (from [21])*

mixed with shake-up from the HOMO creating double excitations [41], corresponds to the resonance labeled π*(D) in *p*-6P. They lie at the same position from the primary resonance and that in *p*-6P displays π* character with X-ray incident angle. The gas phase interpretation of this peak differs slightly, being assigned primarily to a σ*(a_1/C-H) transition with the asymmetric tail due to the π*(b_{2g}) transition with associated double excitations [42].

The σ*(a) transition in *p*-6P is a very broad peak and certainly contains several transitions which may correspond to those responsible for the σ*(i), σ*(ii) features, or the σ*(C-H) transition assigned to σ*(iii) in both solid state and gas phase benzene, concurrent with an IP step edge in the gas phase.

The final features in *p*-6P, σ*(b) and π*(E) lie close to the σ*(iv) resonance in benzene, assigned to two close-lying σ*(C-C) resonances, sometimes with π* shake-up in various sources. In condensed benzene, this polarization dependence suggests a doublet with in-plane and out-of-plane character [42]. As can be seen in Fig.3.8, this region for 6P also consists of a doublet with different angular character.

Chapter 4

Liquid Nitrogen Temperature Growth

The growth of *p*-6P at liquid nitrogen temperature (LNT), -190°C, on TiO_2 (110) was undertaken because it was expected to lower molecular mobility and to produce layer-by-layer growth without the interpretational problems that arise with island growth which occurs at higher temperatures. To a certain extent, this was indeed found to be the case. However, although molecular mobility was reduced, the substrate led to preferential azimuthal orientation, unlike on unordered oxide surfaces [49],[50]. The molecules were found to lie parallel to the surface and the [001] azimuth. Further, the molecules were found to maintain their gas-phase conformation (twisted). From the thermal behaviour, it is suggested that the films are locked into a crystalline structure even at LNT. These conclusions were drawn from electronic sturcture (UPS), morphological (AFM) and optical studies (RDS).

4.1 UPS

Typical growth series following the development of the valence band as a function of 6P exposure at LNT, -190 ± 5°C, are presented in Fig.4.1(a),(c) and 4.2(a), (c) for normal emission (NE) and normal incidence (NI) in the [1$\underline{1}$0] and [001] azimuths of the TiO_2(110) substrate.

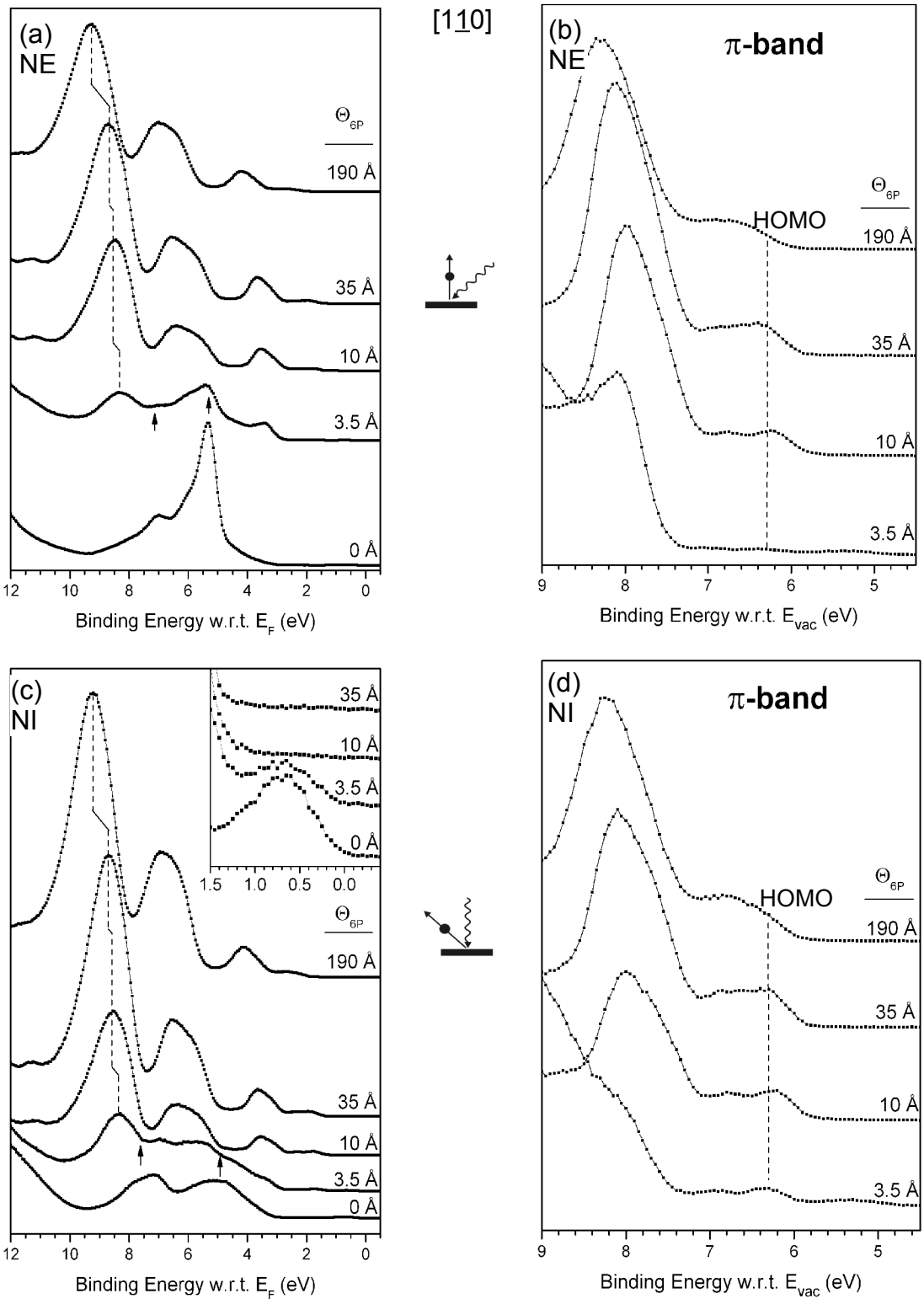

Figure 4.1 *LNT growth series in the [1$\underline{1}$0] azimuthal geometry. The* ***π****-band has been enlarged and the spectra shifted by their work function in (b) and (d) . Substrate features are marked by arrows. The inset shows the substrate defect state in detail.*

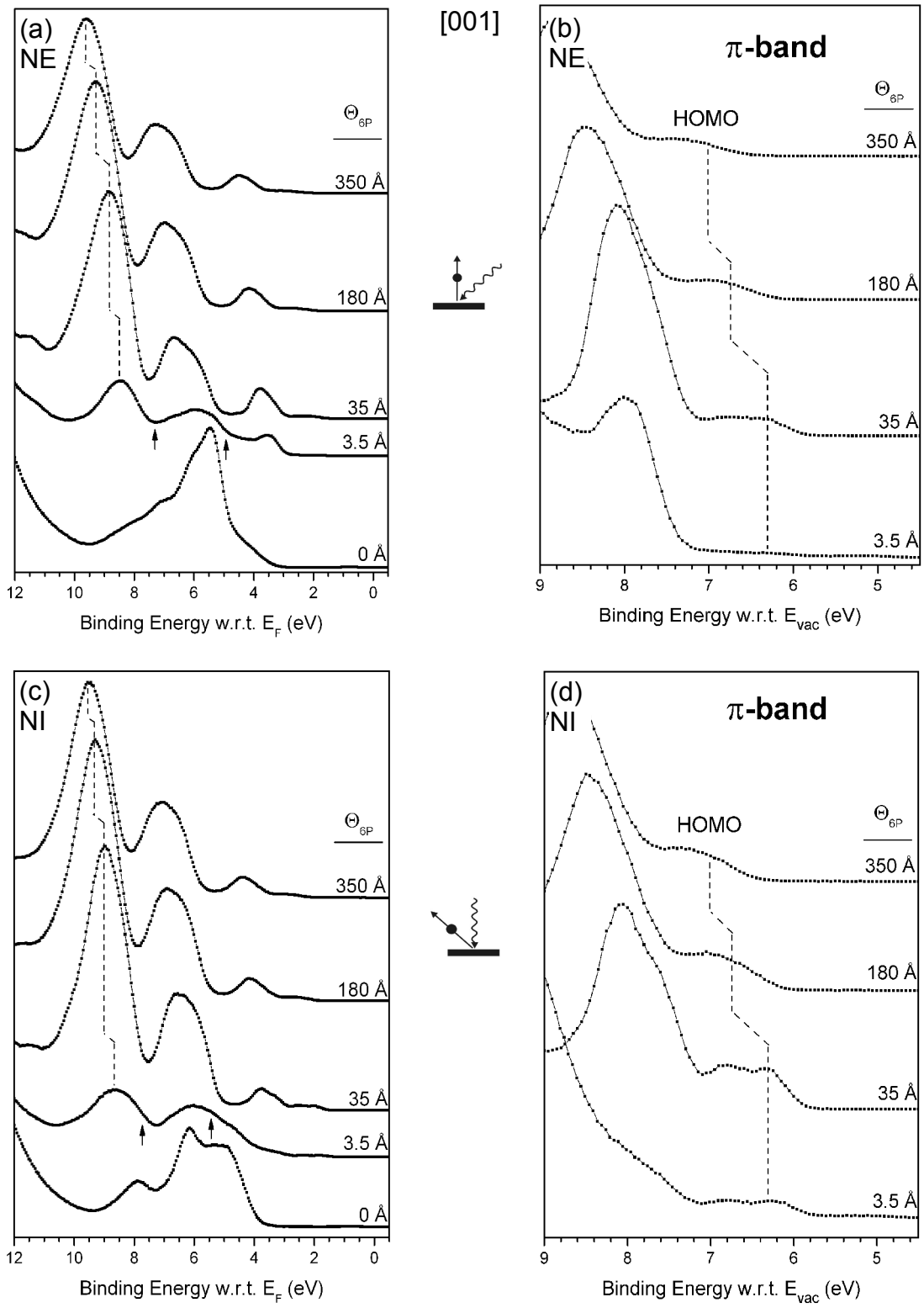

Figure 4.2 *LNT growth series in the [001] azimuthal geometry. The* π*-band has been enlarged and the spectra shifted by their work function in (b) and (d).. Substrate features are marked by arrows.*

As can be clearly seen in Fig.4.1(a),(c), the strong substrate features, indicated by arrows, are buried between 3.5 Å and 10 Å. Since 3.5 Å is about the material equivalent of a dense lying 6P monolayer, such behavior indicates that the growth at LNT occurs in a near layer-by-layer fashion with lying molecules. Beyond coverages of 35 Å, large energy shifts are seen in the spectra that are not associated with changes in the work function ϕ (ϕ for all spectra are given in Fig.4.3), and molecular features become less distinct. These shifts are attributable to charging, either due to thicker insulating 6P layers or some loss of substrate conductivity at LNT.

Monitoring of the growth with ϕ was more complicated in this case than with the growth of *p*-6P on metals, whose ϕ are reproducible and constant beyond 1 ML adsorption [50]. For molecular adsorption, the ϕ changes arise from the interface dipole induced by the interaction of molecules in the first monolayer [1]. The change in ϕ of -0.5 eV from the clean TiO_2 value in the 3.5 – 10 Å region (Fig.4.3) is compatible with the growth mode extracted from the valence band spectra. As no change is seen from 10 Å to 35 Å, it can be concluded that the interface dipole, and concurrently the first monolayer, is completed by ≤10 Å. At coverages of 180 Å and above the ϕ measurements were irreproducible when measured at LNT. Once the samples had been warmed to RT, reliable ϕ measurements could be made.

The π-bands of the growth series spectra are shown in detail in Fig.4.1(b),(d) and 4.2(b),(d). The spectra have been shifted by their respective work functions so that their energy scale is referenced to the vacuum energy E_{vac} and the position of the highest occupied molecular orbital (HOMO) should reflect the solid-state ionization potential (IP). For coverages up to 35 Å, an IP of 6.3 ± 0.1 eV is obtained, which agrees with the gas-phase IP of 5.1 eV [34] when a shift of 1.2 eV due to extra-molecular relaxation is considered [34],[51]. The torsional angle between individual phenyl rings is intimately related to the IP of the molecules, as discussed in Chapter 3 and references [3], [50] and [52]. Since 6P molecules are found to be twisted in the gas phase [34], it can be concluded that the molecules are also twisted in the solid state when grown at LNT. The same result was found for 6P growth on aluminum at LNT and RT and on oxidized aluminum at LNT [50].

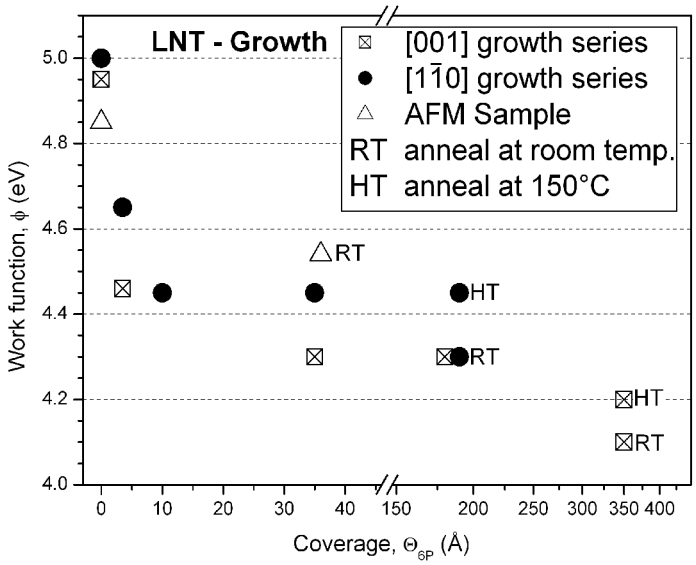

Figure 4.3 *Work function of the films in the UPS growth series and AFM grown at LNT. Due to irreproducibility in the work function for thick films when measured at LNT, only the work function measured after coming to RT has been given for coverages of ≥180 Å. Work functions after RT and HT anneals have been indicated.*

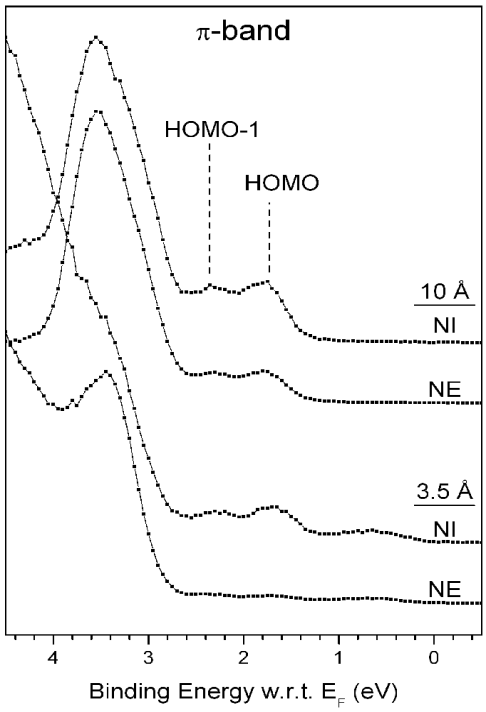

Figure 4.4 *Comparison of normal emission NE and normal incidence NI emission geometries in the [1$\underline{1}$0] azimuthal geometry of the* ***π****-band for LNT growth. NI spectra have been multiplied by 4.*

The HOMO's binding energy both relative to E_F and to E_{vac} show no appreciable shift between the monolayer (3.5 Å) and film (35 Å), and their IPs are the same as in the gas phase. These observations imply that there is no obvious bond to the TiO_2 surface – aromatics show significant increases in π-orbital binding energy (so-called π stabilization) when the π orbitals bond with the substrate [53]. Moreover, this also implies that the extra molecular relaxation of the monolayer due to the substrate is the same as extramolecular screening due to the neighboring molecules in the thin film. Similar observations have been made for benzene [54] and 6P [3] on Al (111) and have been associated with electrostatic bonding.

Although the spectra were collected using unpolarized light and a large acceptance angle, strong angular differences are nonetheless present in the π-band between the NE and NI emission geometries for a coverage of 3.5 Å. When the spectra are corrected for emission intensity as in Fig.4.4 (normalized to the nonbonding orbitals at 3.5 eV), it can be seen that the HOMO and HOMO-1 are nearly forbidden in NE but become prominent for higher emission angles like NI. Such ARUPS behavior has also been observed for the same coverage regime on Al (111) [3] and is indicative of a highly oriented molecular species [53].

For higher coverages angular effects become much less pronounced, as can be seen already at a coverage of 10 Å in Fig.4.4 and for further coverages in Fig.4.1 and 4.2. The decrease in angular effects with increasing coverage could be an indication of increasing disorder with increasing film thickness. The absence of azimuthal differences at all coverages would seem to indicate little or no azimuthal orientation of the molecules. Although the latter cannot be the case, as will become clear in the RDS measurements of Section 4.3.

Fig.4.5(a),(c) contain typical heating series following the development of the valence band as a function of substrate temperature for a 350 Å 6P film for normal emission (NE) and normal incidence (NI) in the [001] azimuth of the TiO_2(110) substrate. The RT spectra were obtained by allowing the cryostat to come to RT overnight, while temperatures above RT were obtained either by annealing, in the case of HT (150°C), or 'flashing', for all higher temperatures, the substrate with the filament behind it.

Thick films at RT no longer display the charging problems – the spectra

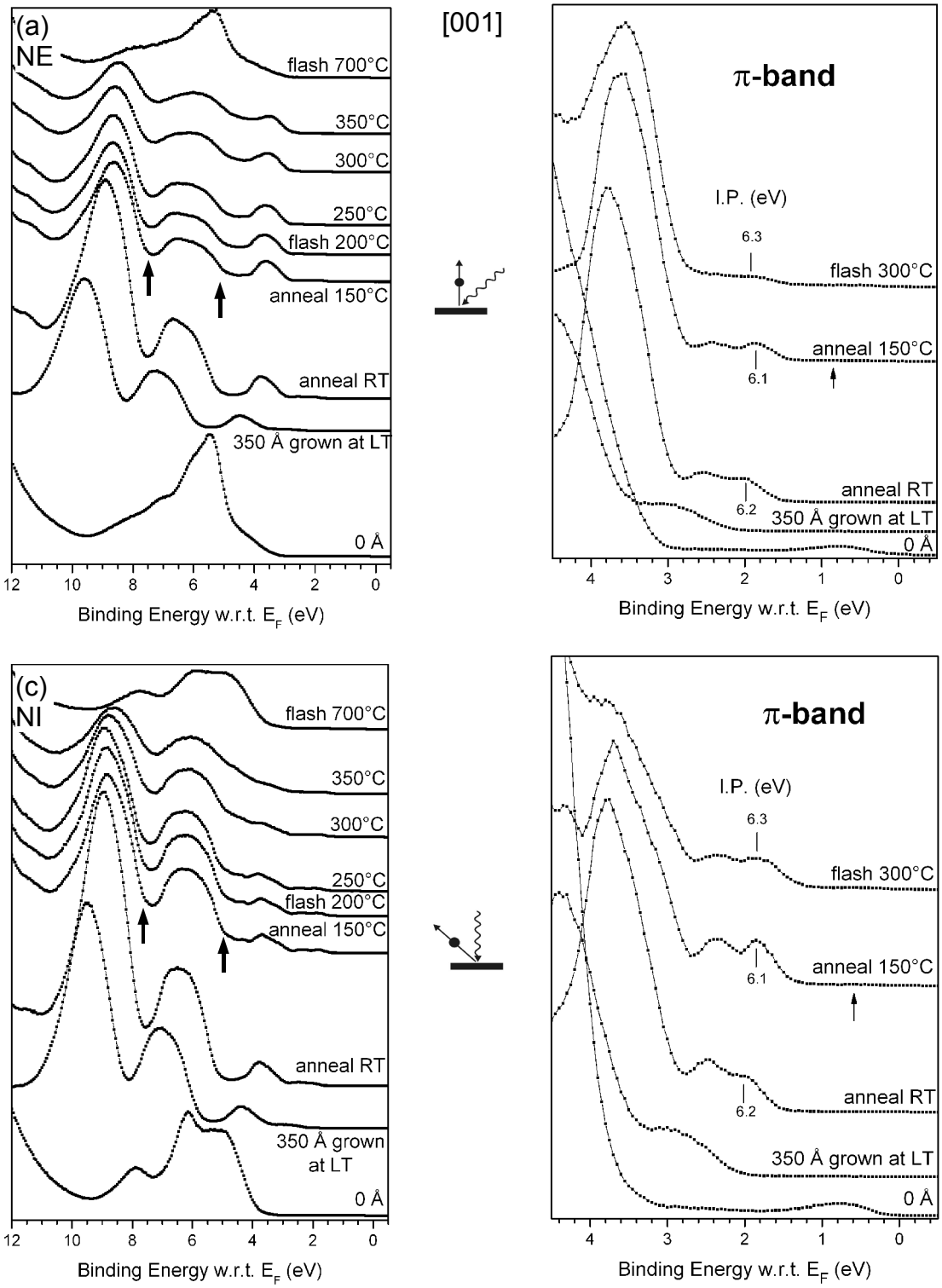

Figure 4.5 *LNT heating series measured in the [001] azimuthal geometry. The arrow in (b) indicates the substrate defect. This heating series was performed on the sample featured in the UPS growth series of Fig.4.1. Note high coverages measured at LNT display charging shifts.*

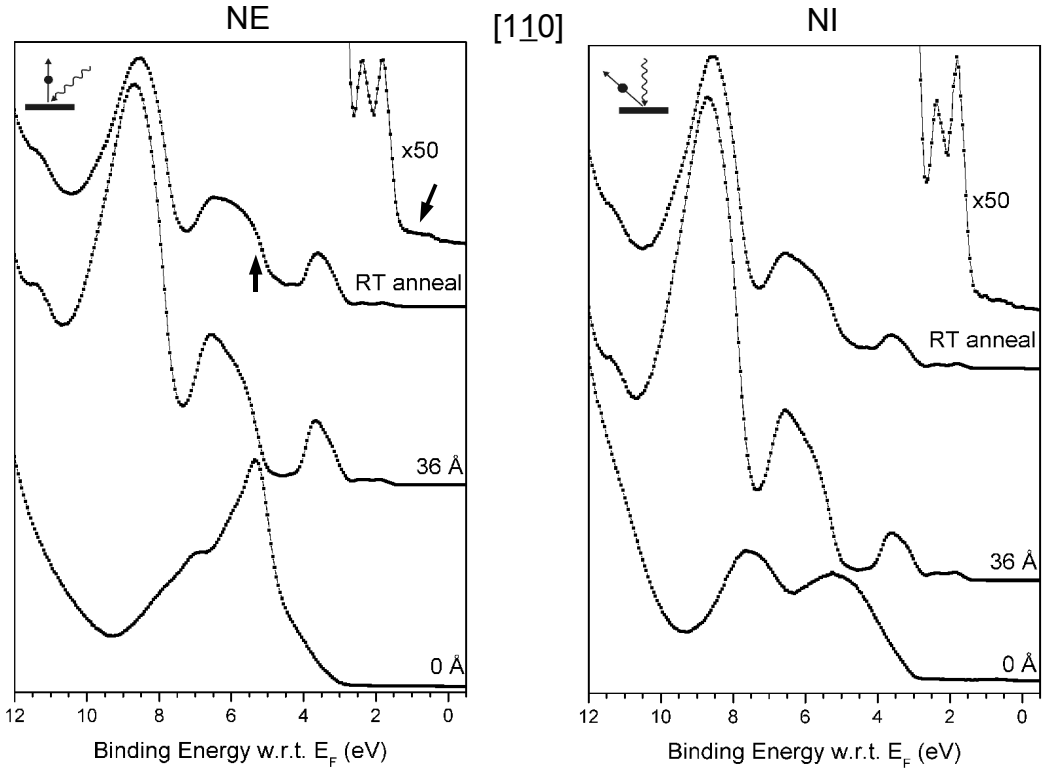

Figure 4.6 *UPS spectra in [1$\underline{1}$0] azimuthal geometry of the 36 Å film grown at LNT for the AFM measurements in Fig.4.7.*

become sharp, the ϕ returns to the expected value and the IP is the same as that obtained for 35 and 3.5 Å at LNT. For a thinner film (35 Å) grown at LNT, where no charging phenomena were observed, warming to RT only has subtle effects (Fig.4.6); significantly, the strong TiO_2 O_{2p} features do not appear as such, and only a trace of substrate defect state appears when the region around E_F is greatly magnified. Thus no strong morphological changes are indicated. Further, the IP remains constant, indicating that there is no conformational change of the molecules in the films on warming to RT. Such behavior is quite different to that of 6P on oxidized aluminum [50], where both conformation and orientation of the molecules changed on warming to RT. These results suggest that the majority of the molecules in the films grown on TiO_2(110) adopt a stable crystalline form even at low temperature.

As the temperature of the substrate is increased further to 150°C (Fig.4.5), the overall intensity of the molecular features decreases slightly and the presence of substrate emissions may be inferred by the filling in of the troughs between the

molecular emission bands. This and the decrease in the secondary electron background is evidence that some islanding occurs. The islanding is accompanied by a significant increase in angular differences between the two emission geometries, NE and NI, as is clearly seen in the difference in intensity of the nonbonding orbitals at 3.5 eV of the π-band of Fig.4.5(b),(d), which indicates an increase in the orientational order of the molecules. A change in orientation is perhaps further supported by the 0.1 to 0.15 eV increase in ϕ, although such a change in ϕ could also be attributed to the newly exposed substrate.

The temperature of the substrate was increased further by brief flashes in 50°C steps. At a temperature of 300°C, a substantial change occurs with the spectral appearance being very similar to 3.5 Å exposure at LNT (Fig.4.2 and 4.5, particularly the π-band in (b),(d)). As the temperature is increased further up to 700°C, the molecular features degrade, but a clean surface is never obtained (Fig.4.5(a),(c)). Evidently, the monolayer is rather well bound to the surface and remains until the molecules are destroyed by heat.

4.2 AFM

A direct study of the morphology of a 36 Å *p*-6P coverage grown at LNT and warmed to RT on TiO_2 was done with *ex-situ* AFM measurements. The UPS spectra obtained at LNT and on warming to RT prior to removal from UHV for the AFM measurements are shown in Fig.4.6. The large-scale (10x10 μm) AFM image of Fig.4.7(a) shows that the surface is regularly covered by two types of structures, which can be seen in detail in the smaller scale images (b),(c), with little material in between. It can be seen in the UPS spectra that, upon warming to RT, substrate features appear which were not present in the spectrum measured at LNT, particularly the substrate defect just below E_F (marked by arrow in Fig.4.6). Such behavior is presumably due to amorphous material between the islands migrating to the islands upon warming. The intensity of the substrate defect emission at about 1 eV below E_F could be the result of bare TiO_2 between the islands, although a molecular monolayer in this region cannot be ruled out. Additionally, the amount of material seen in the AFM seems to agree

(a) 10x10 μm

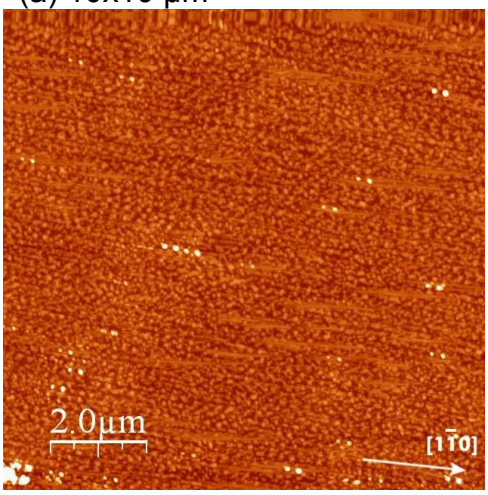

Figure 4.7 *A 36 Å film grown at LNT (-190°C) on TiO_2(110), subsequently annealed at RT (25°C) and measured* ex-situ. ***(a)*** *10x10 μm image.* ***(b)*** *3x3 μm image.* ***(c)*** *Linescan in (b).* ***(d)*** *1x1 μm image.* ***(e)*** *Linescan in (d). The TiO_2(110) [1$\underline{1}$0] azimuthal direction is shown in each image.*

(b) 3x3 μm

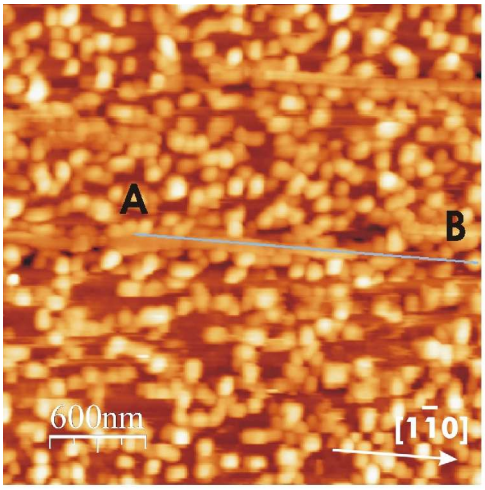

(c) Line scan in (b)

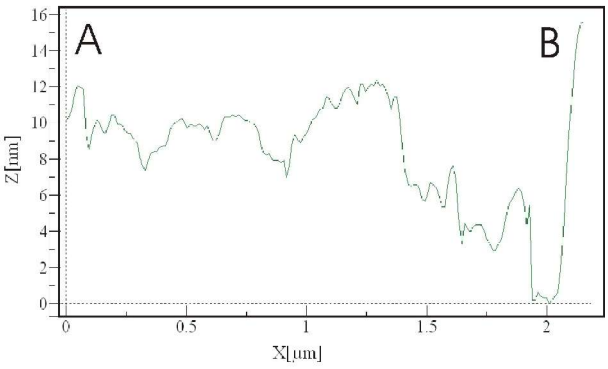

(d) 1x1 μm

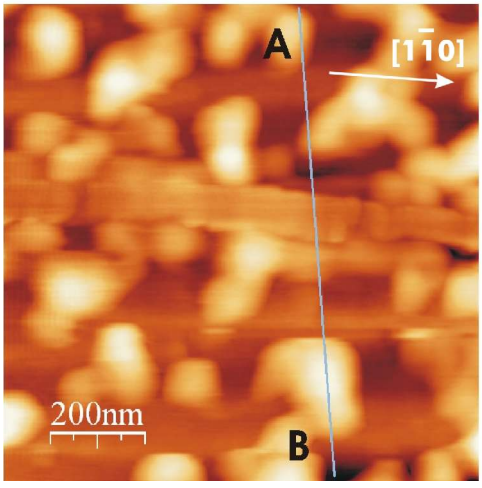

(e) Line scan in (d)

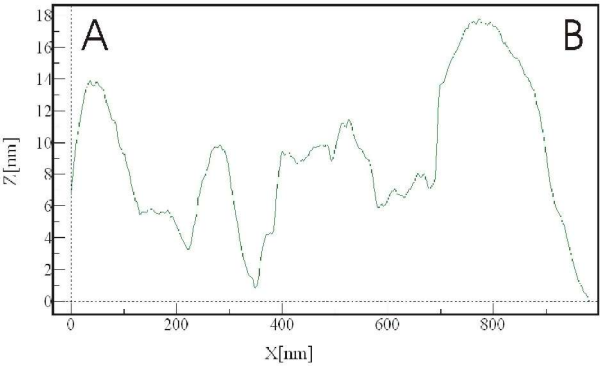

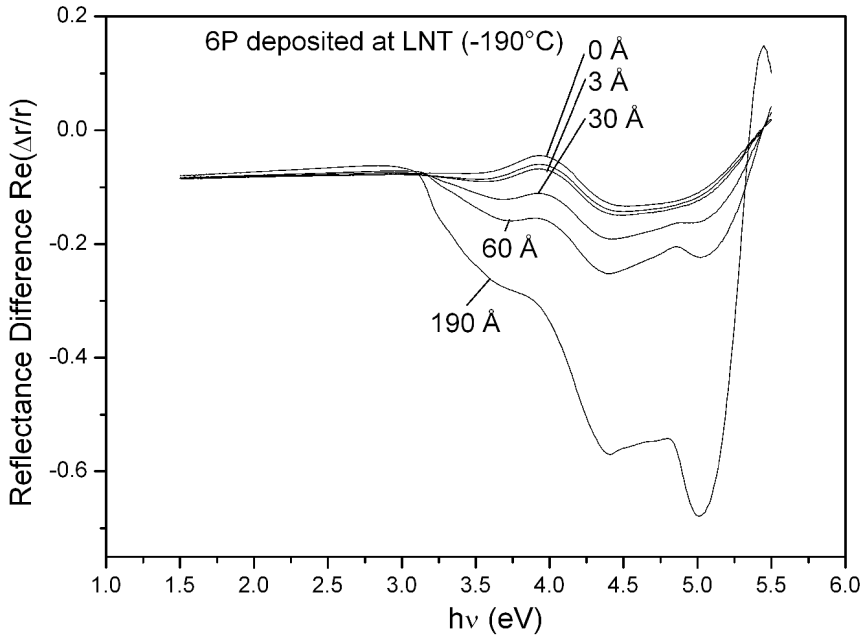

Figure 4.8 *A* p-*6P film was deposited at LNT and subsequent RDS spectra were taken. Negative values indicate lower reflectance in the [001] azimuthal direction.*

with the coverage of 36 Å measured with the quartz microbalance.

In the 10x10μm image (Fig.4.7(a)), it can be seen that the islands tend to aggregate in the [1$\underline{1}$0] substrate azimuthal direction. The smaller and taller structures range in height from 12 to 23 nm and are typically 60 to 200 nm wide (Fig.4.7(e)). Some appear to tend towards a rectangular shape, hinting at some crystal structure. Appearing with far less frequency are longer needle-like structures which range in size from 500x50 nm to 1000x100 nm and show a uniform height of 13 ± 2 nm (from the lowest point found on these images) over distances surpassing a micrometer (Fig.4.7(c)). These longer islands are similar to the needle structures predominantly seen at RT growth (Chapter 6).

4.3 RDS

The angular differences observed in UPS and the regular structures seen in AFM suggest some molecular orientation takes place in *p*-6P grown on TiO_2 even at LNT. To explore this possibility further, *in-situ* RDS measurements were performed

during growth at LNT (Fig.4.8).

The RDS signal of the TiO_2(110) substrate (0 Å in Fig.4.8) displays high anisotropy in the reflection of light polarized along the two azimuthal directions of the substrate throughout the entire spectral range of the instrument, particular in regions above 3 eV where the optical absorption of 6P is found [55]. Originally, it was thought that this would make the observation of 6P difficult. However, as *p*-6P is deposited onto the substrate, the RDS signal increases dramatically above a photon energy of 3 eV. The high amount of anisotropy is evidence of a high amount of order in the film. Since the molecules are expected to absorb light polarized along the molecular axis, and since reflection depends strongly on absorption, RDS clearly indicates that they are oriented primarily with their molecular axes parallel to the [001] substrate azimuthal direction. The RDS signal of a coverage of 190 Å at LNT is nearly identical to the RDS signal from a film of the same thickness grown at RT, known to be highly oriented from NEXAFS and XRD measurements (see Chapter 6).

Chapter 5

High-Temperature Growth

p-6P was deposited at high temperature (HT), 100-150°C, on TiO_2(110) to study its growth under conditions of high molecular mobility. 6P deposited on such different substrates as Al(111) and KCl [5] at HT and on oxidized aluminum at room temperature (RT) have produced films of standing, or upright molecules – molecules with their axes nearly perpendicular to the substrate surface, and, in the cases of 6P on Al(111) at HT and oxidized aluminum at RT, the molecules were found to have a planar conformation [25]. In the following it will be argued that a similar behavior occurs for *p*-6P grown on TiO_2 at HT, where the molecules were found to be planar and upright. Moreover, films of 6P on TiO_2 grown at HT were also seen to grow anisotropically, with preferential molecular diffusion in the direction of the [001] substrate azimuth and a preferential tilt of ~ 13° from the surface normal in the [001] direction. Thermal behavior indicates that the planar standing molecules are weakly bound to the substrate. These conclusions were drawn from electronic structure (UPS), morphological (AFM) and optical studies (RDS).

5.1 UPS

Typical growth series following the development of the valence band as a

function of 6P exposure at HT are presented in Fig.5.1(a),(c) and Fig.5.2(a),(c) for a substrate temperature of 150°C for normal emission (NE) and normal incidence (NI) in the [1$\underline{1}$0] and [001] azimuths of the TiO_2(110) substrate and in Fig.5.3(a),(c) for a substrate temperature of 100°C for NE and NI in the [001] azimuth of the substrate.

Of particular note in Fig.5.1(a),(c) and 5.2(a),(c) is the low coverage (3.5 Å) as it (1) significantly suppresses the substrate features (at least as much as 3.5 Å at LNT) and (2) displays a different π-band fingerprint, IP and angular behavior to higher coverages. The result suggests that, at low coverages, the surface is approximately covered with lying twisted molecules (similar to HT growth on clean Al(111) [25]).

As the coverage is increased, the substrate features, indicated by arrows, are buried between 35 Å and 180 Å. In the insets showing the substrate oxygen defect state in detail, it can be seen that the 35 Å spectra still display a hint of substrate defect state when compared to the spectra at higher coverages, particularly in the NE geometry. From 180 Å to 350 Å, no change is seen in the molecular emission bands.

Observation of the behavior of the growth series for a substrate temperature of 100°C in Fig.5.3(a),(c) leads to the same conclusions as for 150°C above with one exception. Although the molecular features are similar to those for growth at 150°C, it can be seen in the π-band detail of growth at 100°C that the peak labeled A at 8 eV w.r.t. E_{vac} in Fig.5.3(b),(d) has a higher intensity compared to the nonbonding orbitals than the same peak for growth at 150°C in the same emission geometry (cf. Fig.5.2(b),(d)). The position of peak A is concurrent with that of the six nonbonding orbitals of the twisted molecules of a 3.5 Å coverage at 150°C and coverages of 3.5 to 35 Å grown at LNT (Fig.4.2(b),(d)). Moreover, the nonbonding orbitals of the coverages with twisted molecules also tend to display a higher intensity in the NE geometry than in the NI geometry, similar to the behavior of peak A, suggesting that the higher intensity of peak A for a growth temperature of 100°C is due to the nonbonding orbitals of a twisted species which grows concurrently with the planar species presumably observed alone at a growth temperature of 150°C.

Fig.5.4 shows the development of the work function ϕ with increasing 6P coverage for four different samples: the three growth series above and the sample measured by AFM later in this chapter. After an initial drop $\Delta\phi \sim 0.4$ eV for

coverages of 3.5 Å, ϕ remains essentially constant for coverages up to 350 Å. If one grew an upright monolayer, the ϕ should reach its final value at ~ 27 Å. $\Delta\phi$ saturation at ~ 4 Å suggests that a lying molecular monolayer covers the surface at this coverage.

The π-bands of the growth series spectra are shown in detail in Fig.5.1(b),(d), 5.2(b),(d) and 5.3(b),(d). The spectra have been shifted by their respective work functions so that their energy scale is referenced to the vacuum energy E_{vac} and the position of the highest occupied molecular orbital (HOMO) should reflect the solid-state ionization potential (IP). For coverages of 3.5 Å at both 100°C and 150°C, an IP of 6.3 ± 0.1 eV is obtained, which agrees with the gas-phase IP of 5.1 eV [34] when a shift of 1.2 eV due to extra-molecular relaxation is considered [34],[51]. Since 6P molecules are found to be twisted in the gas phase [34], it appears that the molecules are also twisted for this low coverage when grown at HT. Coverages of 10 Å and above display an IP of 5.7 ± 0.1 eV, which is 0.6 eV lower than that of the twisted molecules seen at a coverage of 3.5 Å. Since the torsional angle between individual phenyl rings is intimately related to the IP of the molecules, as discussed in Chapter 3 and references [3], [50] and [52], and calculations show that the IP can be shifted by up to 0.5 eV depending on the twist angle of the phenyl rings [37], it can be concluded here that the 6P molecules are planar in the solid state for coverages above ~ 4 Å when grown at HT. The same result was found for 6P growth on aluminum at HT and on oxidized aluminum at RT [50], in which cases it has been determined that the solid state consists of upright molecules with a tilt angle of ~ 13° from the surface normal, as shown in [16] and Section 2.1.2 (Fig.2.9) of this thesis. For HT growth on Al(111), XRD results have revealed that the 6P (001) facet is parallel to the surface [16].

Although the spectra were collected using unpolarized light and a large acceptance angle, strong angular differences are nonetheless present in the π-band between the NE and NI emission geometries for a coverage of 3.5 Å (Fig.5.1(b),(d) and 5.2(b),(d)). As with a coverage of 3.5 Å grown at LNT (Fig.4.4), the HOMO and HOMO-1 are nearly forbidden in NE but become prominent for higher emission angles like NI. Such ARUPS behavior has also been observed for the same coverage regime on Al(111) [3] and is indicative of a highly oriented molecular species [53].

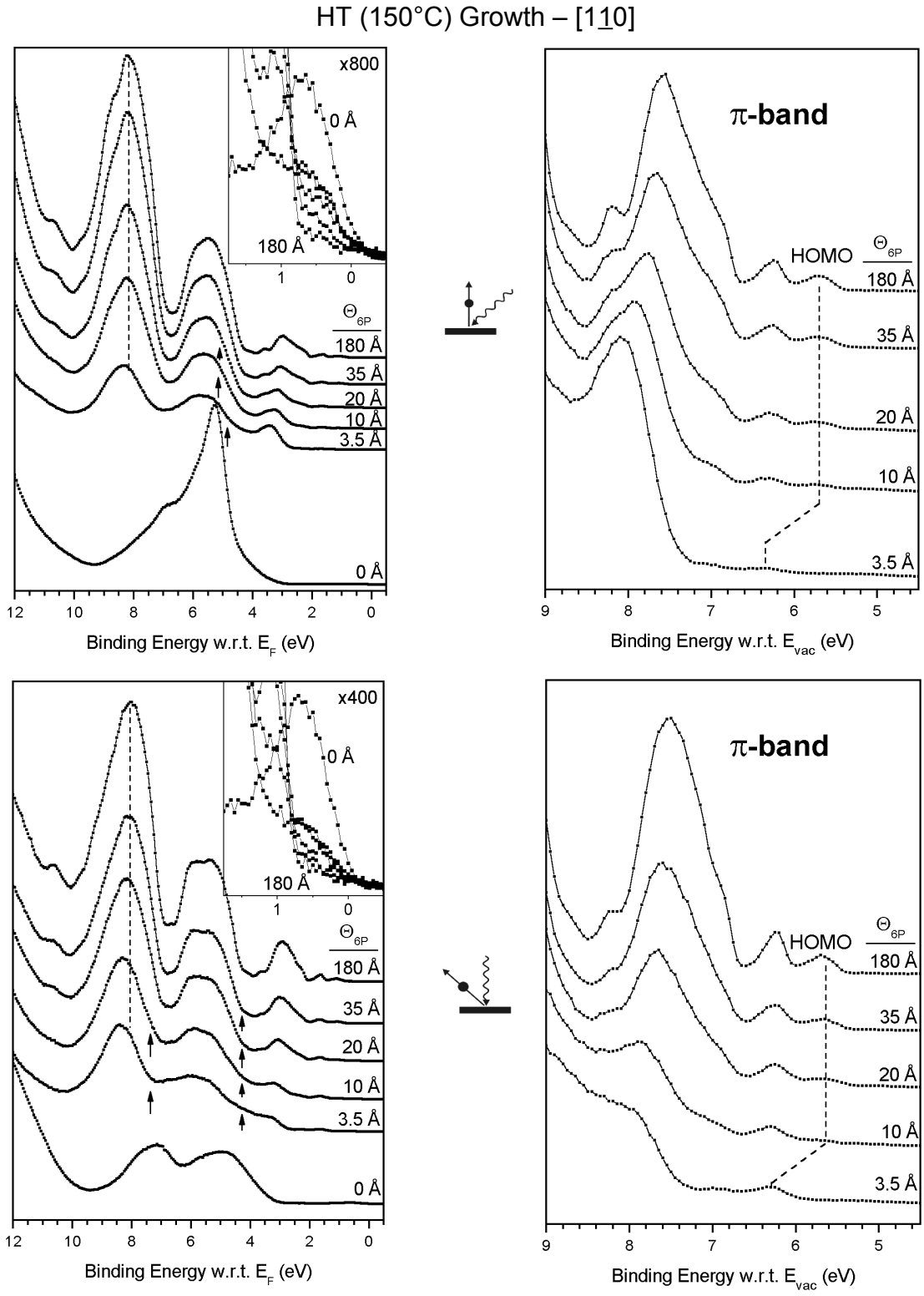

Figure 5.1 *HT (150°C) growth series in the [1$\underline{1}$0] azimuthal geometry. The* ***π****-band has been enlarged and the spectra shifted by their work function in (b) and (d). Substrate features are marked by arrows in (a) and (c). The insets show the substrate defects just below the Fermi level E_F in detail.*

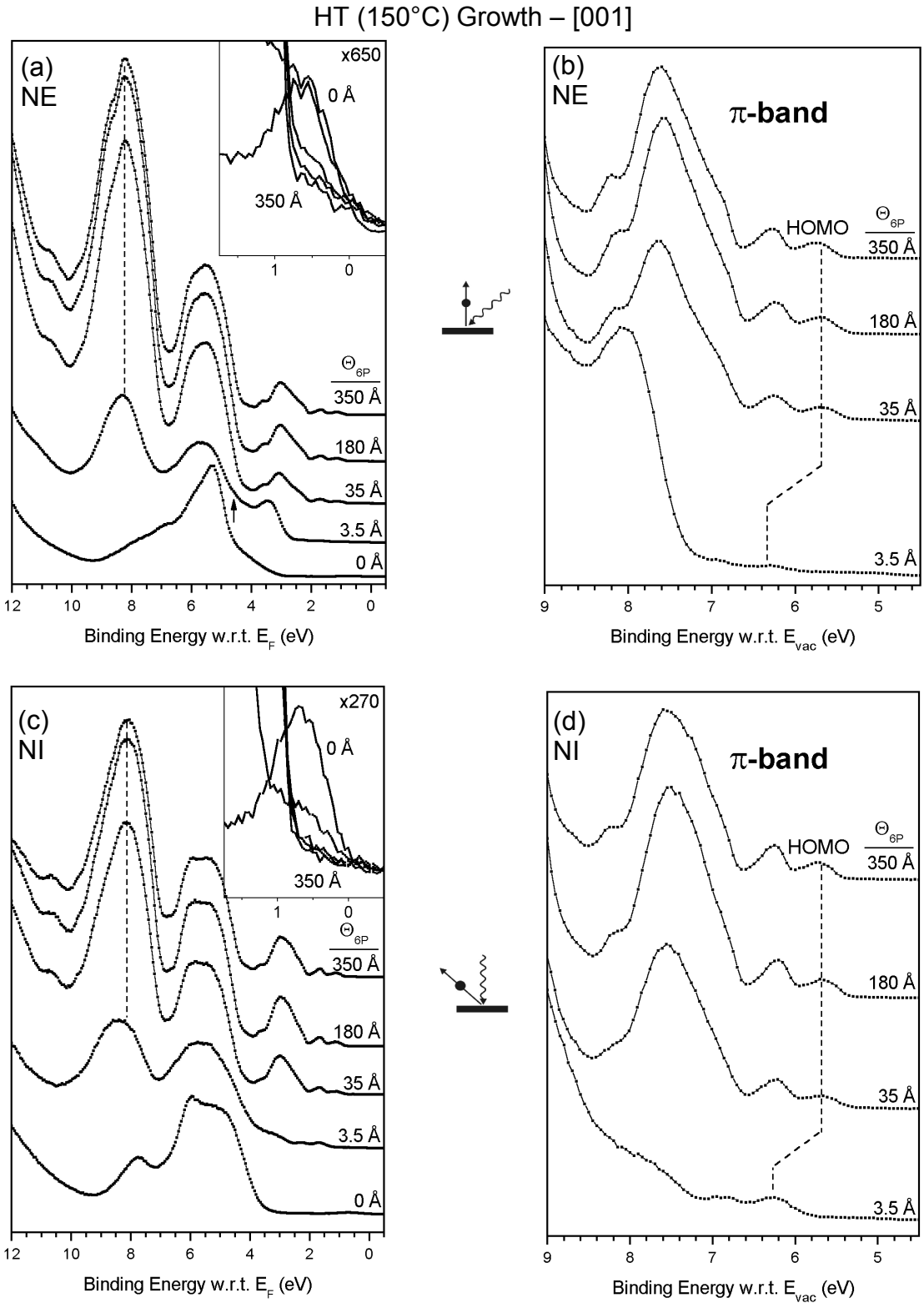

Figure 5.2 *HT (150°C) growth series in the [001] azimuthal geometry. The* π*-band has been enlarged and the spectra shifted by their work function in (b) and (d). Substrate features are marked by arrows in (a) and (c). The insets show the substrate defects just below the Fermi level* E_F *in detail.*

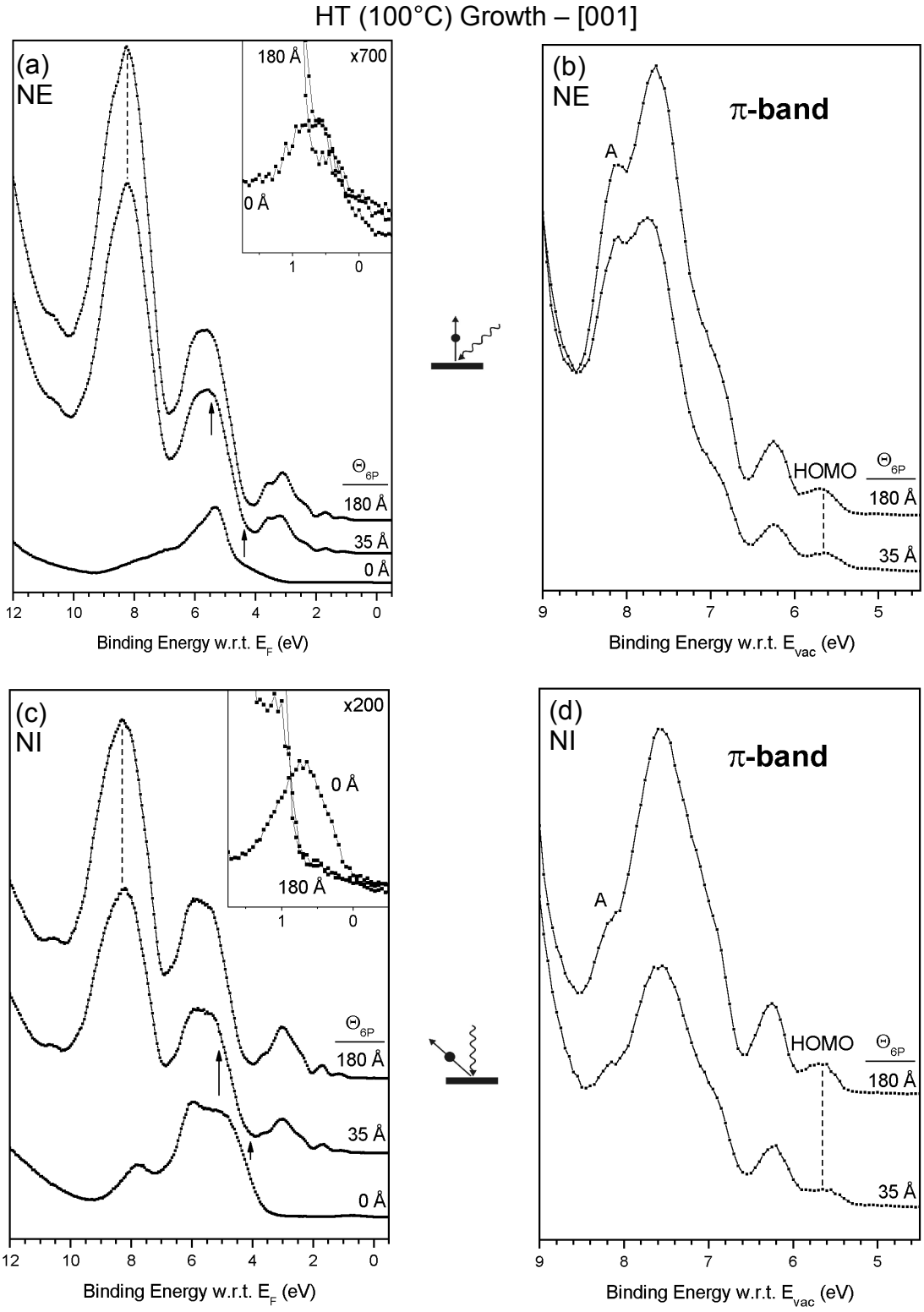

Figure 5.3 *HT (100°C) growth series in the [001] azimuthal geometry. The* π*-band has been enlarged and the spectra shifted by their work function in (b) and (d). Substrate features are marked by arrows in (a) and (c). The insets show the substrate defects just below the Fermi level* E_F *in detail.*

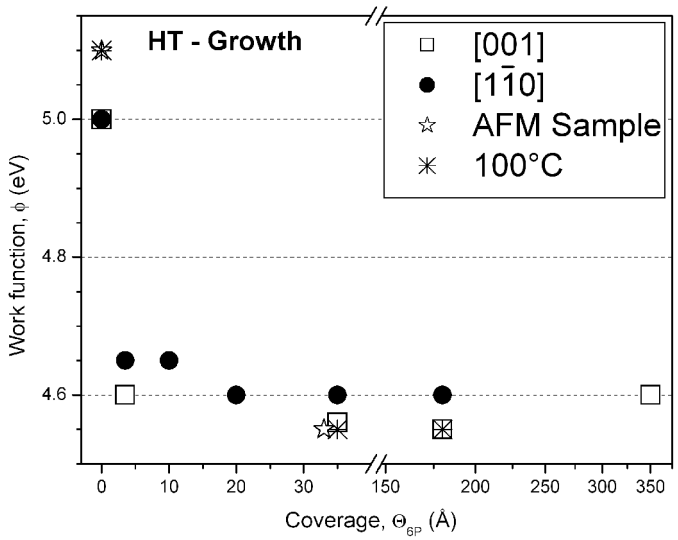

Figure 5.4 *Work function of the films in the UPS growth series and AFM grown at HT.*

For higher coverages angular effects in the π-band are far less pronounced. Additional angular differences can also be seen in the other molecular emission bands at 4 to 6 eV and 7 to 9 eV BE. Angular differences for all coverages indicate that the molecule is highly oriented even in thick films, which is expected for growth at higher temperatures. The absence of azimuthal differences in all coverages grown at 150°C indicates that there is little or no azimuthal orientation of the molecules, which is consistent with standing molecules, even if they are found in the Baker structure.

According to the considerations in Chapter 3 of the π-band splitting in *p*-6P (Fig.3.8(b)), the spread of the π-band should be largest when the molecule is planar. Indeed, all three inter-ring antibonding orbitals are resolved in most HT spectra. These orbitals are labeled in Fig.5.1(b) as HOMO, HOMO-1, and HOMO-2. Two of the three inter-ring bonding orbitals can be seen at binding energies (BE) of 8.2 eV and 8.7 eV with respect to E_{vac}, at a higher BE than the six degenerate nonbonding orbitals. Changes in conformation from a coverage of 3.5 Å to higher coverages make it difficult to draw any conclusions regarding bonding to the TiO_2 substrate.

Fig.5.5 contains heating series following the development of the valence band as a function of substrate temperature for a 180 Å 6P film for normal emission (NE) and normal incidence (NI) in the [1$\underline{1}$0] azimuth of the TiO_2(110) substrate. Little difference is seen in the spectra when the 180 Å film is heated briefly up to 300°C (not displayed). At a temperature of 350°C, a substantial change occurs with the

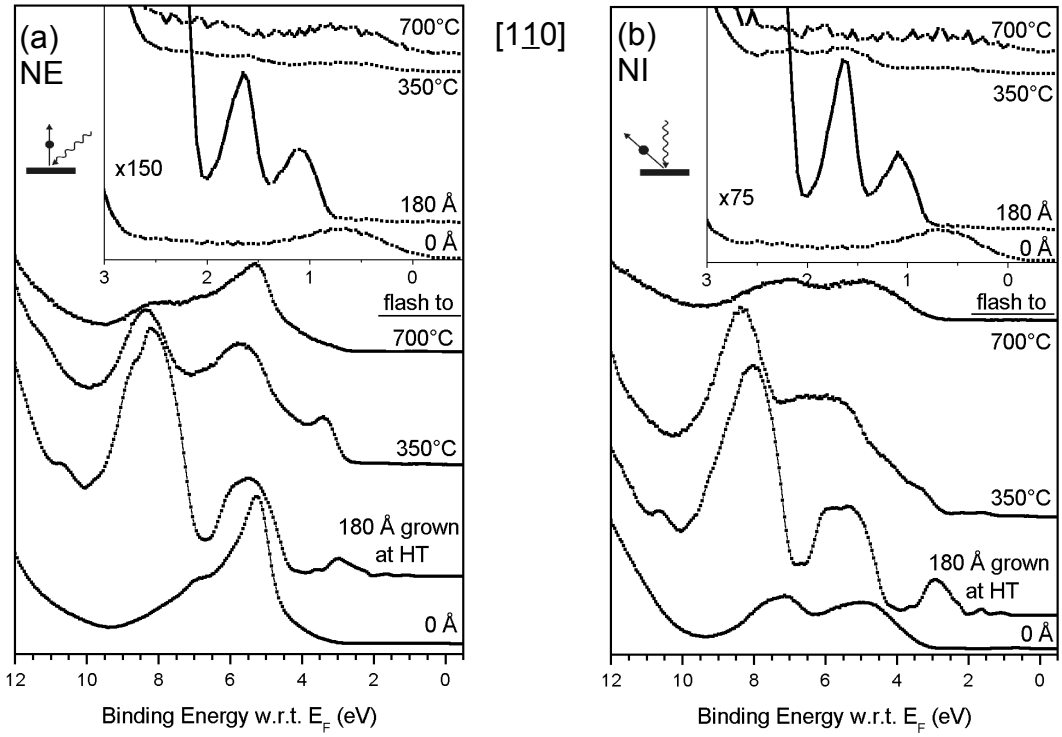

Figure 5.5 *UPS HT heating series measured in the [1$\underline{1}$0] azimuthal geometry. The region below the Fermi level EF has been enlarged in the insets. This heating series was done on the sample featured in the growth series of Fig.5.1.*

spectral appearance being very similar to 3.5 Å exposure at 150°C (Fig.5.1), suggesting that the upright molecules with an IP ~ 5.7 eV are weakly bound to the substrate. As the temperature is increased further up to 700°C, the molecular features degrade, but a completely clean surface is never obtained, as seen in the poorly defined O_{2p} features of the substrate. Evidently, some material with a twisted conformation is well bound to the surface and remains until the molecules are destroyed by heat.

5.2 AFM

A direct study of the morphology of a 35 Å 6P coverage grown at HT (150°C) on TiO_2 was done with *ex-situ* AFM measurements. The UPS spectra obtained prior to removal from UHV for the AFM measurements are shown in Fig.5.6. The large-scale

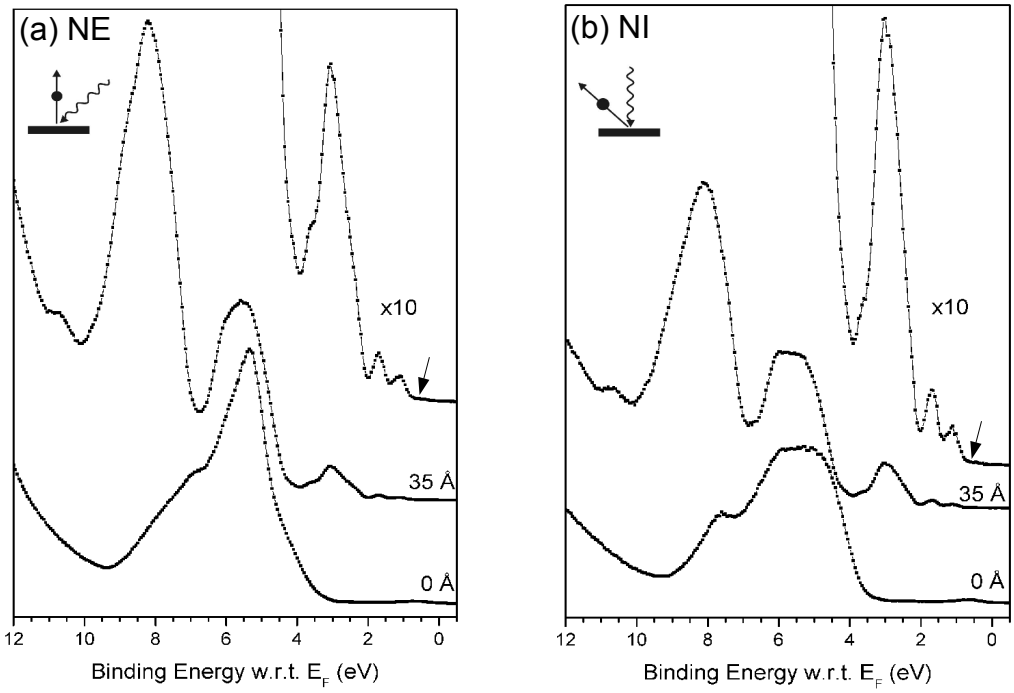

Figure 5.6 *UPS spectra in [001] azimuthal geometry of the 35 Å film grown at HT (150°C) measured by AFM in Fig.5.7.*

(20x20 μm) AFM image of Fig.5.7(a) shows that the surface is primarily covered by large islands elongated in the direction of the TiO_2 [001] principle azimuth. These large islands consist of a 'wedding-cake' structure with steps of 25 ± 2 Å, which can be clearly seen in the line scan of (a) in Fig.5.7(e). Since the length of the molecule is ~26.5 Å, it can be reasonably concluded that these layers are made of standing molecules. Any tilt in the molecules would, of course, result in a lower step height than the full length of the molecule. These islands typically run uninterrupted for more than 20 μm, the largest scan size of the instrument. Nevertheless, ends were periodically seen in this direction, as shown in Fig.5.7(c),(d). Observed widths vary widely from 0.5 to 10 μm in the [1$\underline{1}$0] direction.

The area between the larger islands appears to be exposed TiO_2 substrate, although a lying monolayer of 6P molecules cannot be ruled out due to the small amount of substrate defect state visible in the UPS (marked with arrow in Fig.5.6). The AFM, nevertheless, displays a significant phase change (not shown) between the islands and the area between them, indicating a difference in their relative 'hardness'.

Between the large islands, small islands, apparently randomly distributed, are

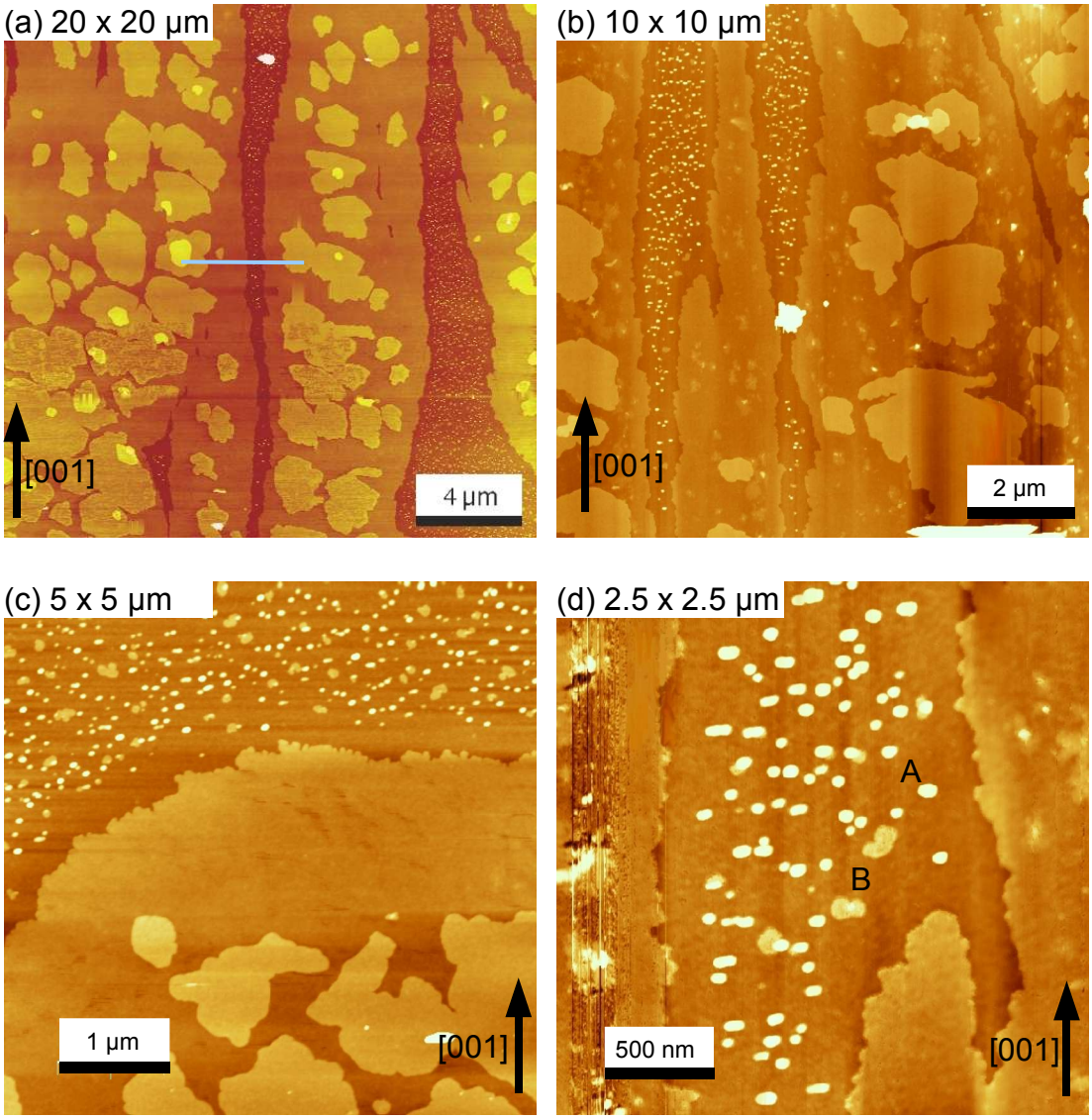

(e) Line scan in (a)

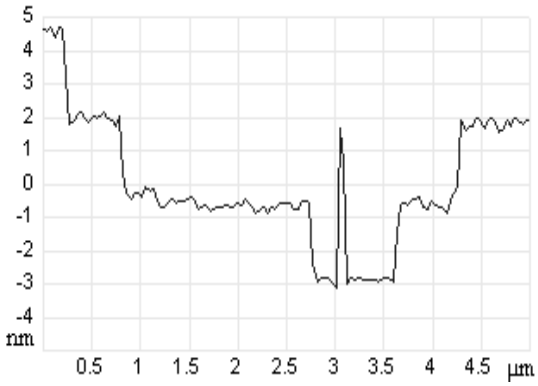

Figure 5.7 *AFM of a* p-6P *film grown at HT (150°C) on* TiO_2*(110) and measured* ex-situ. *In* ***(d)****, the two types of smaller islands have been labeled A and B. The* TiO_2 *(110) [001] azimuthal direction is shown in each image.Images* ***(a)*** *and* ***(c)*** *have been scanned at 90° to images* ***(b)*** *and* ***(d)****.*

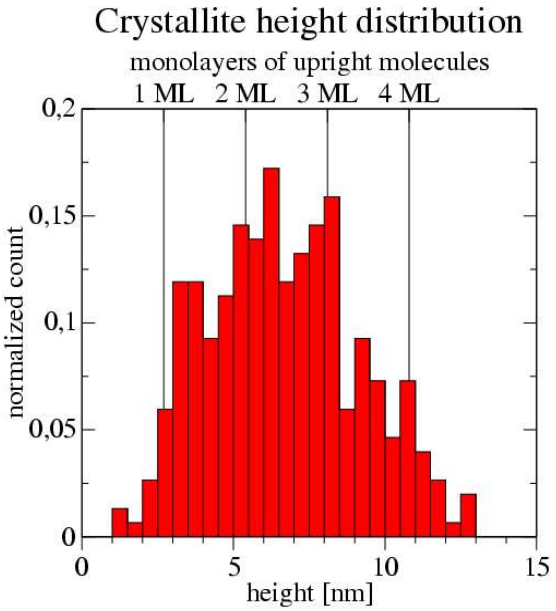

Figure 5.8 *Distribution of the heights of small crystallites in the upper half of the image on the left in Fig.5.9 below.*
1 ML = 27 Å

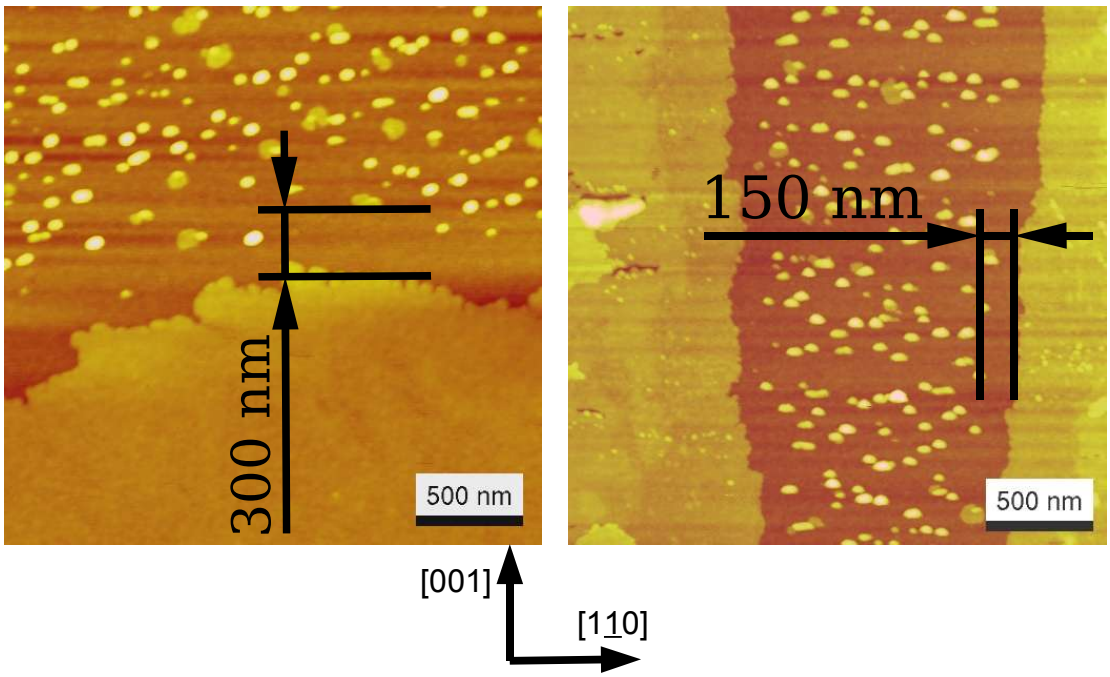

Figure 5.9 *Width of the denuded zone along the two principal azimuths. The image on the left is a 2.5 x 2.5 μm magnification of the center of Fig.5.7(c).*

found, as seen in detail in Fig.5.7(d) and Fig.5.9. Most of these islands, those that appear brighter and generally elliptical, e.g. those labeled 'A' in Fig.5.7(d), have lateral dimensions between 20 and 100 nm and are often 50 - 60 % wider in the TiO_2 substrate [1$\underline{1}$0] azimuthal direction. The elongation is not a scanning artifact, as confirmed by a comparison between the images in Fig.5.7(d) and 5.9 which were scanned at 90° to each other. A statistical analysis (Fig.5.8) reveals that the heights of these islands are non-uniform and tend to cluster around integer multiples of 27 Å – approximately the height of a standing ML – suggesting that these islands consist of layers of standing molecules. Although the small island included in the line scan of Fig.5.7(e) appears to be a tall tower, the lengths of this and similar structures range increasingly from 15 times their height for islands with a height of 1 ML to 150 times their height for 4 ML.

More irregular islands, e.g. those labeled 'B' in Fig.5.7(d), are also found in the area between the large islands, although they are less numerous than the small oblong islands. With lateral dimensions around 100 nm, they generally have about 5 times the area of the smaller islands and are of the same height as the large islands of standing molecules, i.e. the height of a single upright molecule. They appear to be a smaller version of the large islands and occasionally contain second and third layers of ML height.

Around their circumference, the large islands display a zone depleted of the small oblong islands. This denuded zone is not isotropic around the larger islands. It can be seen in Fig.5.9 that it has a width of approximately 300 nm in the direction of the [001] substrate azimuth and only 150 nm in the direction of the [1$\underline{1}$0] azimuth. This denuded zone can also be observed around the small irregular islands such as those labeled 'B' in Fig.5.7(d). In Fig.5.7(c), it can be seen that this zone often extends only in the [001] direction around the smaller islands. The anisotropic nature of the denuded zone and the preferential growth of the large islands along the [001] substrate azimuthal direction indicates that an anisotropy exists in the diffusion of the molecules over the surface during growth. Calculations for aromatic monomers (benzene, pyridine) on TiO_2 indicate that they adopt edge-on geometries hydrogen bonded to the oxygen rows and are highly mobile along them, i.e. along [001] [56]. Indeed here, diffusion is clearly favored along the oxygen rows in the direction of the

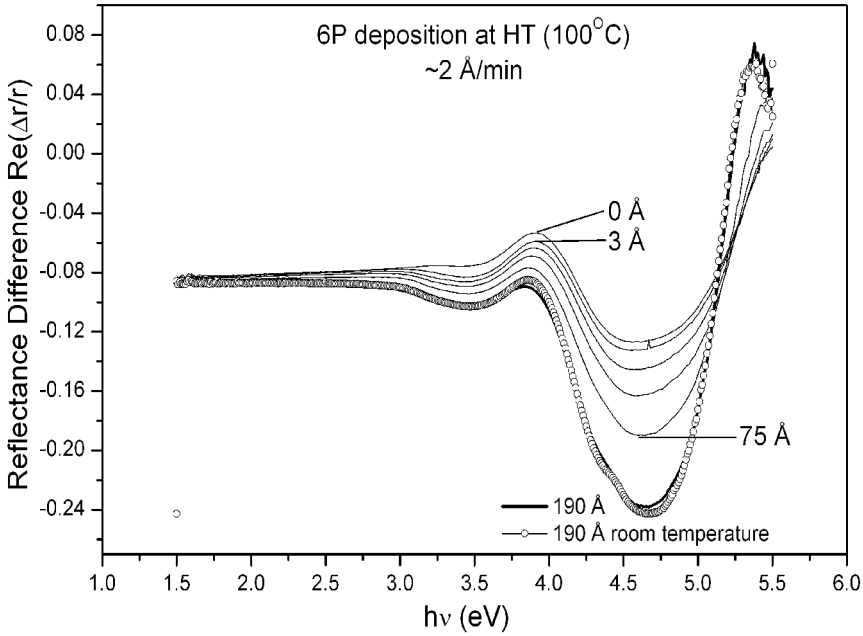

Figure 5.10 *A* p-*6P film was deposited at HT and subsequent RDS spectra were taken. Negative values indicate lower reflectance in the [001] azimuthal direction.*

TiO_2 substrate [001] principle azimuth. The anisotropic growth is lost already in the 2nd ML, as evidenced by isotropic 2nd and 3rd layer growth on the larger islands, confirming that the TiO_2 is indeed responsible for the anisotropic growth of *p*-6P at HT. 6P grown on TiO_2 by hot-wall epitaxy, not by evaporation in UHV as in the present study, did not produce the same anisotropic effects in the growth [57].

5.3 RDS

The angular differences observed in UPS suggest that some molecular orientation takes place in *p*-6P grown on TiO_2 at HT. The lack of azimuthal differences in the UPS data, however, does not suggest that azimuthal orientation of the molecules exists. To explore the possibility of azimuthal orientation, *in-situ* RDS measurements were performed during growth at 100°C (HT) and presented in Fig.5.10.

The RDS signal of the TiO_2(110) substrate (0 Å in Fig.5.10) displays high anisotropy in the reflection of light polarized along the two azimuthal directions of the substrate. However, as 6P is deposited onto the substrate, the RDS signal increases

dramatically above a photon energy of 3 eV. Since the molecules are expected to absorb light polarized along the molecular axis, and since reflection depends strongly on absorption, RDS indicates that the molecules tend to tilt in the [001] direction. This is in agreement with recent surface XRD experiments performed at ESRF in Grenoble [58]. The spectral fingerprint of 6P deposited at HT is somewhat different to that of LNT (Fig.4.8) and RT (Fig.6.17), and the signal intensity is greatly reduced at HT.

The strongly reduced intensity would be expected for the near upright species that is observed in the AFM for HT growth. What is perhaps most surprising is not the reduction in intensity, but that there is still a strong optical anisotropy seen. Perfectly upright molecules would show nearly no anisotropy, whereas tilted species (as expected for 6P(001)) would also show no anisotropy unless there was a preferred tilt direction. On simple geometrical grounds, if the molecules were tilted ± 13° along [001], the length of the molecular axis exposed to the incident light would be ~ 1/5 of the length of the molecule. The optical anisotropy induced by 190 Å at HT is $\Delta r/r \sim 0.1$ at an energy of 4.7 eV, while 190 Å at LNT causes a change of ~ 0.5, corresponding well to the geometric ratio.

Chapter 6

Room-Temperature Growth

The growth of *p*-6P at room temperature (RT) on TiO_2(110) was undertaken to study the films that form at typical ambient temperatures. It became clear from various experimental runs that mixed phases were often formed and the precise substrate temperature seemed a critical factor. Consequently, growth was studied over a temperature range of 0°C to 40°C.

Here it is shown that at 0°C, *p*-6P forms highly oriented nano-needles from the initial stages of growth up to thin films. Although the growth of *p*-6P needles has been reported on the dielectrics mica and alkali halides [27], [59], [60], [61], [62], these needles consist of numerous crystallite orientations [62]. In contrast the *p*-6P nano-needles on TiO_2 presented here display only a single crystalline orientation, the p-6P (20$\underline{3}$). These *p*-6P(20$\underline{3}$) crystallites are exclusively oriented along the TiO_2[1$\underline{1}$0] substrate azimuth. All the molecules are perfectly parallel to each other, to the substrate surface and to the TiO_2[001] azimuthal direction, with their molecular planes all having the same angle of ±34° with respect to the substrate surface plane. Furthermore, the highly oriented nature of the molecules causes a great degree of optical anisotropy in the films.

When the growth temperature is increased to 40°C, in addition to the needles, other areas form in which the molecules adopt an upright orientation. Moreover, these

upright molecules are found to have a planar conformation, in contrast to the twisted conformation of the molecules in the needles.

These conclusions were drawn from electronic structure (UPS), morphological (AFM) optical (RDS) crystallographic (XRD) and absorption studies (NEXAFS).

6.1 UPS

Typical growth series following the development of the valence band as a function of 6P exposure at RT are presented in Fig.6.1(a),(c) for a substrate temperature of 40°C ± 10°C for normal emission (NE) and normal incidence (NI) in the [1$\underline{1}$0] azimuth of the TiO_2(110) substrate and in Fig.6.2(a),(c) for a substrate temperature of 0°C ± 10°C for NE and NI in the [001] azimuth of the substrate.

As can be seen in Fig.6.1(a),(c) and 6.2(a),(c), the strong substrate features, indicated by arrows, are buried between 35 Å and 180 Å. Since 3.5 Å is about the material equivalent of a dense lying 6P monolayer, such behavior indicates that islanding occurs for growth at RT.

As with growth at HT, monitoring the growth with ϕ was inconclusive at RT. An initial drop of $\Delta\phi$ ~ 0.25 to 0.4 eV from the clean TiO_2 value is seen in coverages of 3.5 Å (Fig.6.3). Above this coverage, even up to thicker films, a further decrease of not more than 0.1 eV is seen. For molecular adsorption, the ϕ changes arise from the interface dipole induced by the interaction of molecules in the first monolayer [1]. Although it appears that the interface dipole is largely completed by ≤10 Å, growth information extracted from the UPS spectra suggests that the substrate is still not completely covered in this coverage regime. Indeed, results seen later in the STM section of this chapter indicate that a wetting molecular monolayer is not formed at these low coverages.

The π-bands of the growth series spectra are shown in detail in Fig.6.1(b),(d) and 6.2(b),(d). The spectra have been shifted by their respective work functions so that their energy scale is referenced to the vacuum energy E_{vac} and the position of the highest occupied molecular orbital (HOMO) should reflect the solid-state ionization potential (IP). For 6P grown at 40°C (Fig.6.1) and 0°C (Fig.6.2), an IP of 6.2 ± 0.1 eV

is obtained for a coverage of 3.5 Å. For coverages of 10 Å and up, the IP diverges between the films grown at these two temperatures. The IP of the films grown at 40°C changes to 5.7 ± 0.1 eV for coverages ≥10 Å, while the IP remains 6.2 ± 0.1 eV for growth at 0°C.

The shift in the HOMO w.r.t. the deeper orbitals (such as at 8 eV) in going above 3.5 Å at 40°C (Fig.6.1) is very clear. Two possible reasons for this are (1) π-bond stabilization in the monolayer or (2) a change in the conformation of the molecules. Growth at 0°C (Fig.6.2) clearly demonstrates that the latter is the case. At 0°C there is no shift in the HOMO with coverage, and its IP remains at 6.2 eV, indicative of a twisted molecular species. The behavior of the RT spectra of coverages >3.5 Å is probably the result of a mixture of twisted and upright planar species. The latter dominate the area-average, surface-sensitive UPS.

A comparison of UPS spectra of growth at 0°C and 40°C with films grown at LNT and HT further elaborates this interesting characteristic of growth in the RT temperature range. In Fig.6.4, 180 Å grown at 40°C and at 0°C is compared to 35 Å grown at LNT (180 Å shifts due to charging) and 180 Å at HT in corresponding emission geometries. Clearly, growth at 40°C has a spectral appearance very similar to HT, while growth at 0°C is similar to LNT. These similarities are seen both in the shape and position of all molecular emission bands and suggest that the growth of twisted molecules with a lying orientation, as for LNT growth, is preferred at 0°C. For growth at 40°C, it has been mentioned above that a planar upright species dominates the UPS signal, but, since UPS is surface sensitive and, thus, area sensitive, it may not reflect the majority species. Therefore, it is possible that more molecules are in the needles at 40°C, although they are not explicitly seen in UPS.

For RT growth in various experimental runs, the UPS suggests mixtures of twisted and planar species. This mixture leads to quite complex π-band structure, but evidence for the HOMOs of twisted and planar species can be discerned on careful inspection. For instance in Fig.6.5(a),(b), the spectra of 35 Å grown at RT shows the signal is dominated by twisted molecules with their distinctive HOMO of IP = 6.3 eV, but a shoulder with an IP of 5.7 eV is also evident. The AFM of this particular sample showed the surface to primarily contain oriented needles, however regions were also present which clearly indicated patches of upright molecules. In contrast, the >300 Å

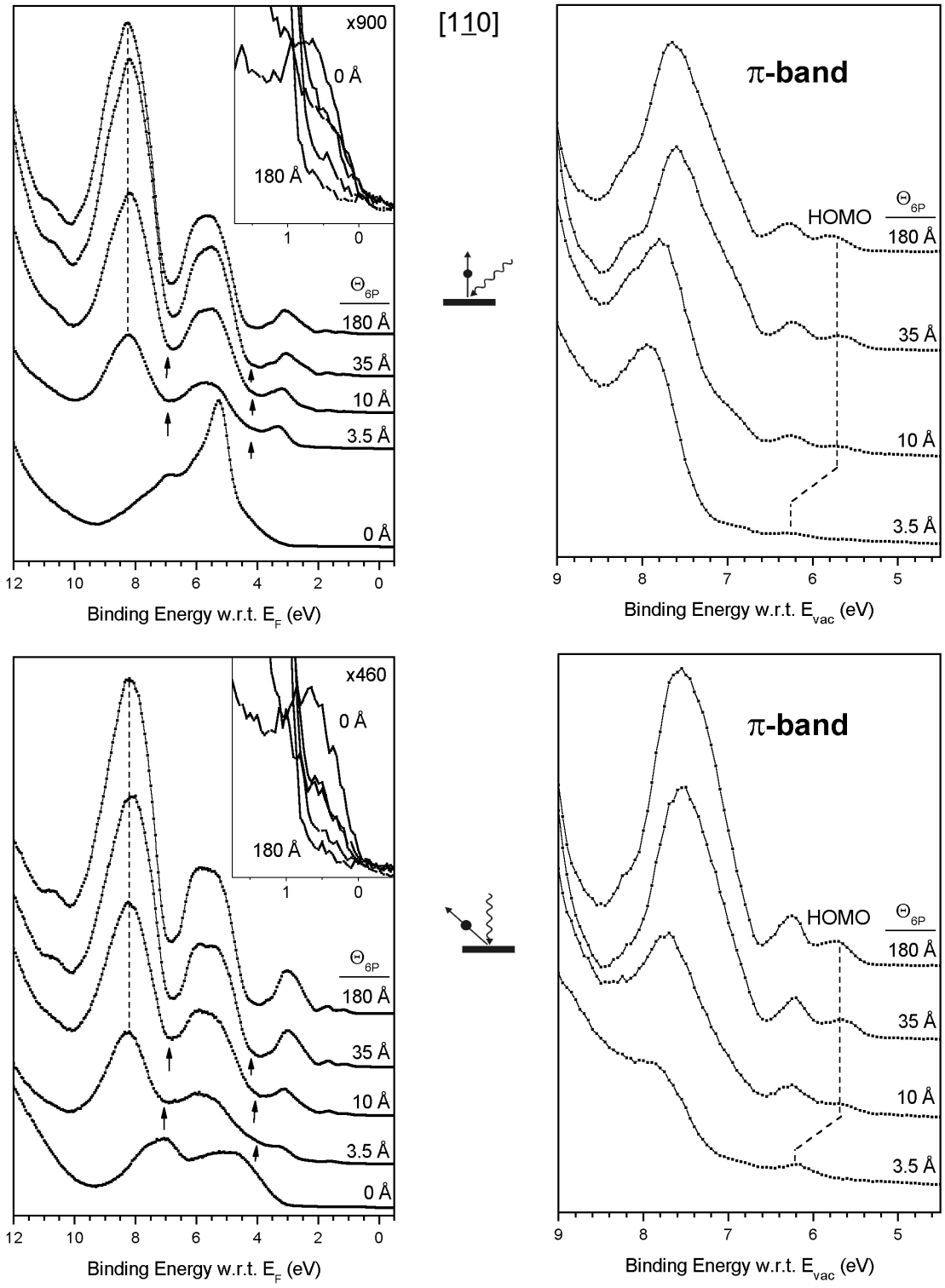

Figure 6.1 *RT (40°C) growth series in the [1$\underline{1}$0] azimuthal geometry.The* ***π****-band has been enlarged and the spectra shifted by their work function in (b) and (d). Substrate features are marked by arrows in (a) and (c). The insets show the substrate defects just below the Fermi level* E_F *in detail.*

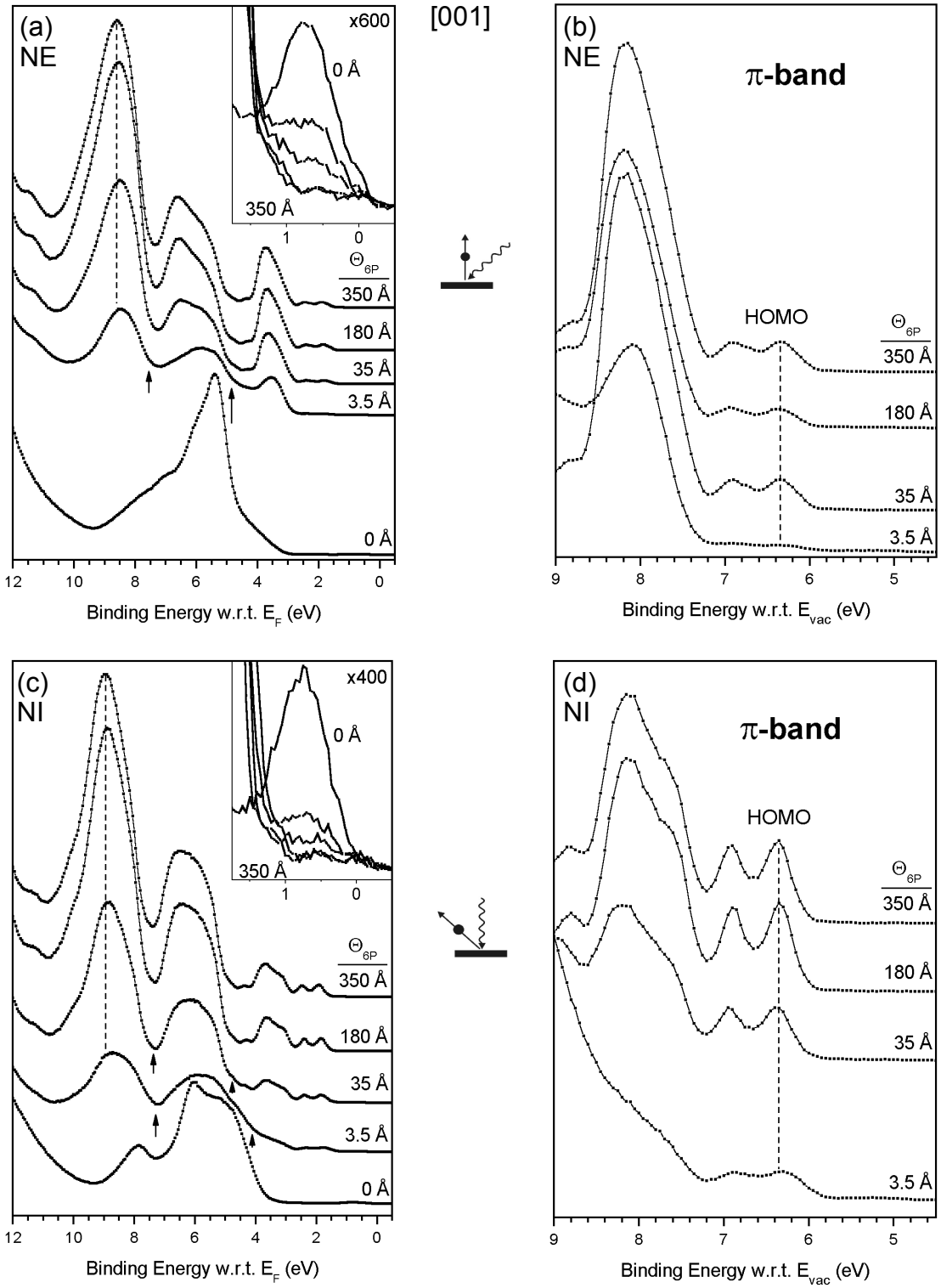

Figure 6.2 *RT (0°C) growth series in the [001] azimuthal geometry. The* π*-band has been enlarged and the spectra shifted by their work function in (b) and (d). Substrate features are marked by arrows in (a) and (c). The insets show the substrate defects just below the Fermi level* E_F *in detail.*

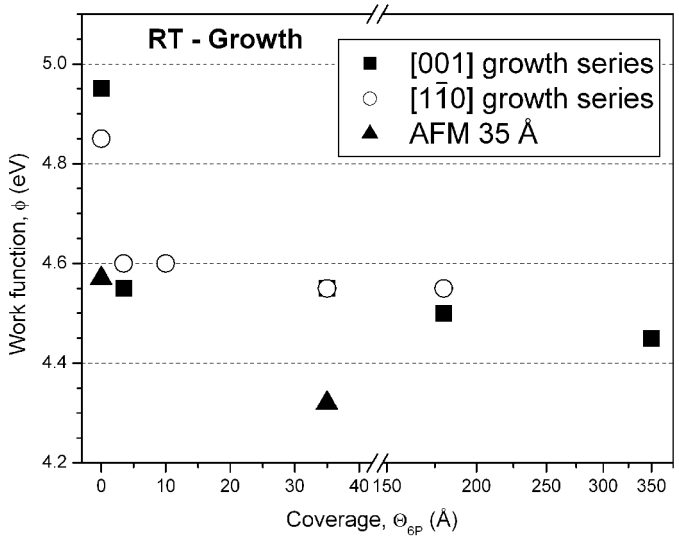

Figure 6.3 *Work function of the films in the UPS growth series and the 35 Å film used for AFM grown at RT. While the AFM shows deviant values for the work function, those af the growth series were typical of other samples made at RT.*

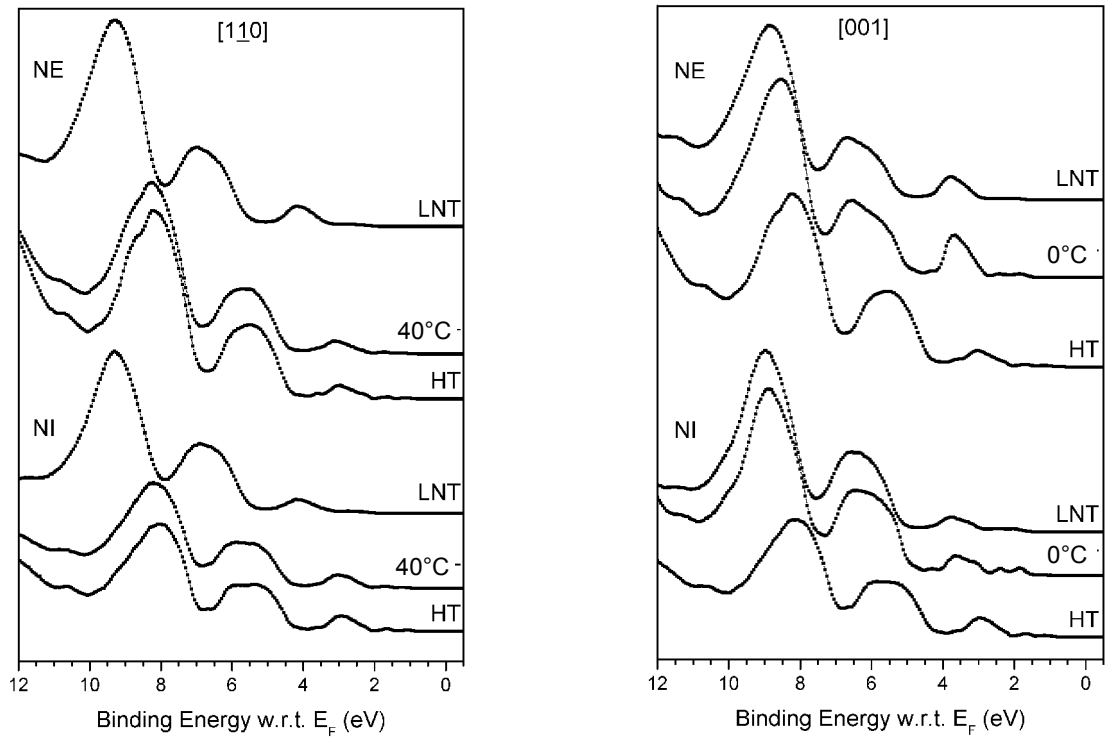

Figure 6.4 *Comparison of normal emission (NE) and normal incidence (NI) UPS spectra 35 Å at LNT, 180 Å at RT and 180 Å at HT in both azimuths. Taken from growth series in Fig.4.1, 4.2, 5.1, 5.2, 6.1 and 6.2.*

sample grown at 0°C in Fig.6.6(a),(b) indicates that no species with an IP of 5.7 eV exist, and NEXAFS of this sample confirms that standing molecules are not present.

Although the spectra were collected using unpolarized light and a large acceptance angle, strong angular differences are nonetheless present on the π-band between the NE and NI emission geometries for a coverage of 3.5 Å (Fig.6.1(b),(d) and 6.2(b),(d)). As with a coverage of 3.5 Å grown at LNT (Fig.4.4) and HT (Fig.5.1 (b),(d) and 5.2(b),(d)), the HOMO and HOMO-1 are nearly forbidden in NE but become prominent for higher emission angles like NI. Such ARUPS behavior has also been observed for the same coverage regime an Al(111) [3] and is indicative of a highly oriented molecular species [53].

For higher coverages, angular effects in the π-band become somewhat less pronounced but remain throughout all coverages, seen particularly in the difference of the shape of the nonbonding orbitals between NE and NI geometry for growth both at 40°C (Fig.6.1(b),(d)) and at 0°C (Fig.6.2(b),(d)). Additionally, differences in intensity between the nonbonding orbitals and the HOMO and HOMO-1 can be observed for 0° C growth. Angular differences for all coverages indicate that the molecule is highly oriented even in thick films. Although a comparison of UPS spectra recorded in the two substrate azimuths of the TiO_2(110) surface, [1$\underline{1}$0] (Fig.6.1) and [001] (Fig.6.2), show differences in the intensity ratios of the nonbonding orbitals and the antibonding orbitals, because of the different temperatures at which these films were grown, such differences may not be used for conclusions about azimuthal orientation of the molecules.

Fig.6.7 and Fig.6.8 contain typical heating series following the development of the valence band as a function of substrate temperature for a 35 Å film for normal incidence (NI) in the [1$\underline{1}$0] azimuth of the TiO_2(110) substrate and for a 10 Å film for normal emission (NE) and normal incidence (NI) in the [001] azimuth. Before heating, both films display evidence of twisted species and planar species, whose HOMO is seen at ~ 1.7 eV w.r.t. E_F (marked by lines) or as a shoulder at a BE of 1.2 eV (shaded), respectively.

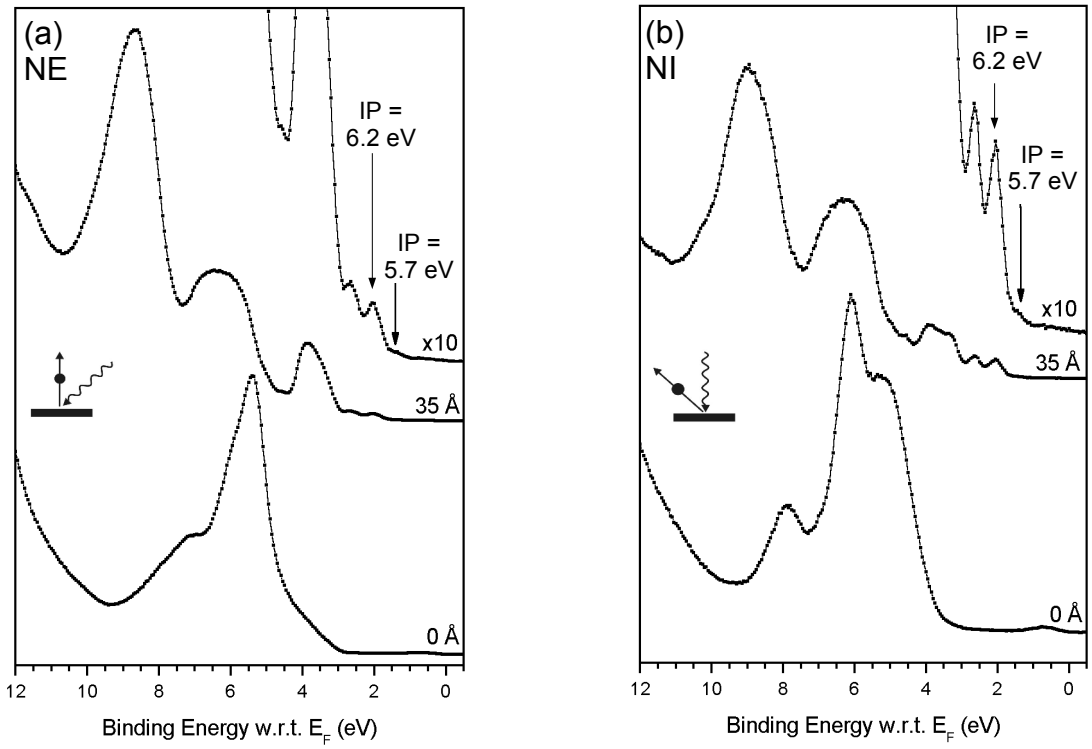

Figure 6.5 *UPS spectra in [001] azimuthal geometry of the 35 Å film grown at 40°C and measured by AFM in Fig.6.9(b),(c).*

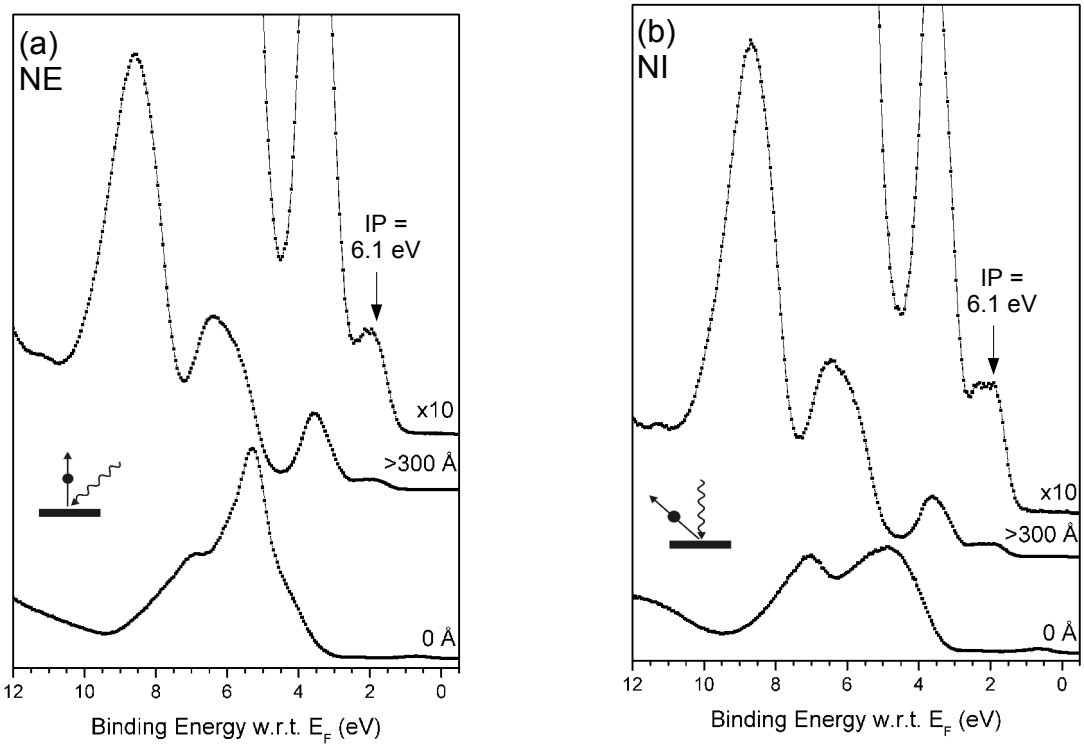

Figure 6.6 *UPS spectra of >300 Å film grown at 0°C measured by NEXAFS in Fig.6.14(a).*

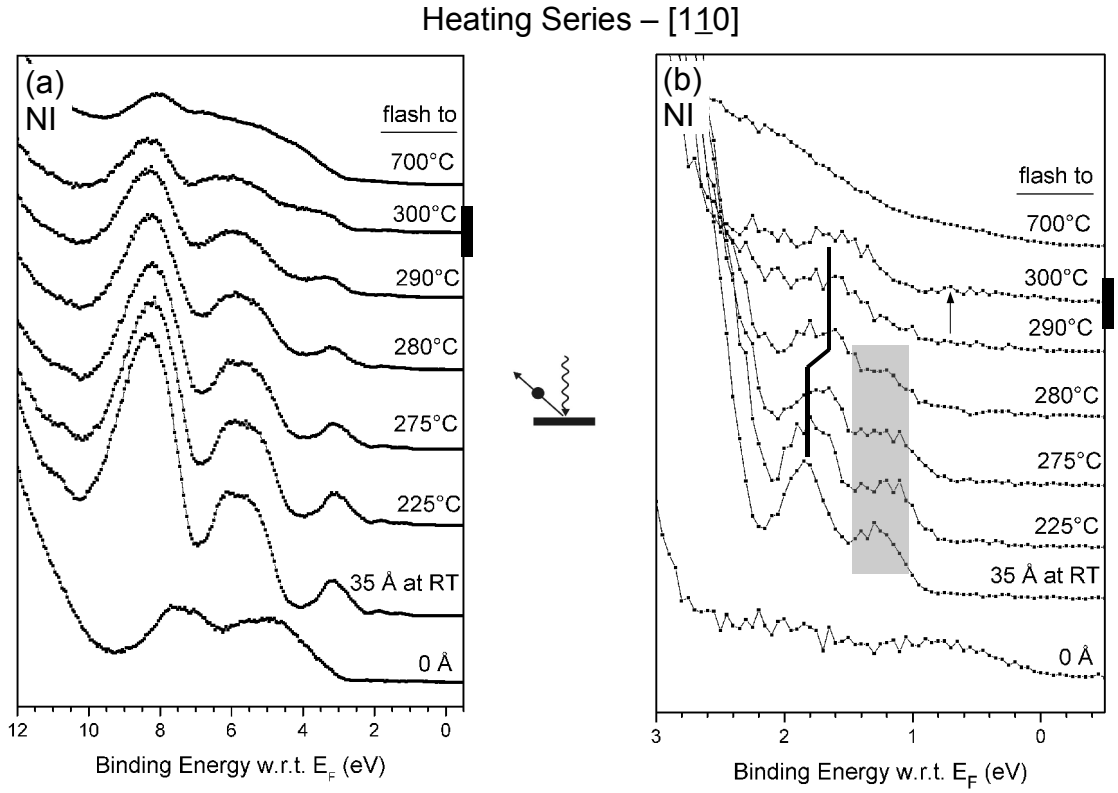

Figure 6.7 *UPS RT heating series measured at NI in the [1$\underline{1}$0] azimuthal geometry. The shaded box indicates HOMOs with IP = 5.7 eV. HOMOs with IP = 6.2 eV are marked by a line. Arrow indicates substrate defect states.*

As seen for both LNT and HT growth, at a certain temperature the films obtain the spectral appearance of a coverage of 3.5 Å, marked by bars in Fig.6.7 and 6.8. At this point in both films, the HOMO at 1.2 eV BE has vanished, indicating that the planar species has completely desorbed. Here, the return of substrate features, particularly the substrate defect ~ 1 eV below E_F (arrows in Fig.6.7 and 6.8), suggests a loss of most of the molecules, both lying and standing. As seen in the NEXAFS data later in this chapter (Fig.6.17), the heating of a 180 Å sample was accompanied by a major reduction in signal with the remaining molecules being parallel to the surface. Although variations in temperature due to different mountings and uneven heating prevent a precise determination of desorption temperature, this evidence clearly indicates that the standing molecules desorb before the lying molecules, suggesting that the upright molecules are more weakly bound to the substrate.

As the temperature is increased further up to 700°C for the 35 Å film (Fig.6.7),

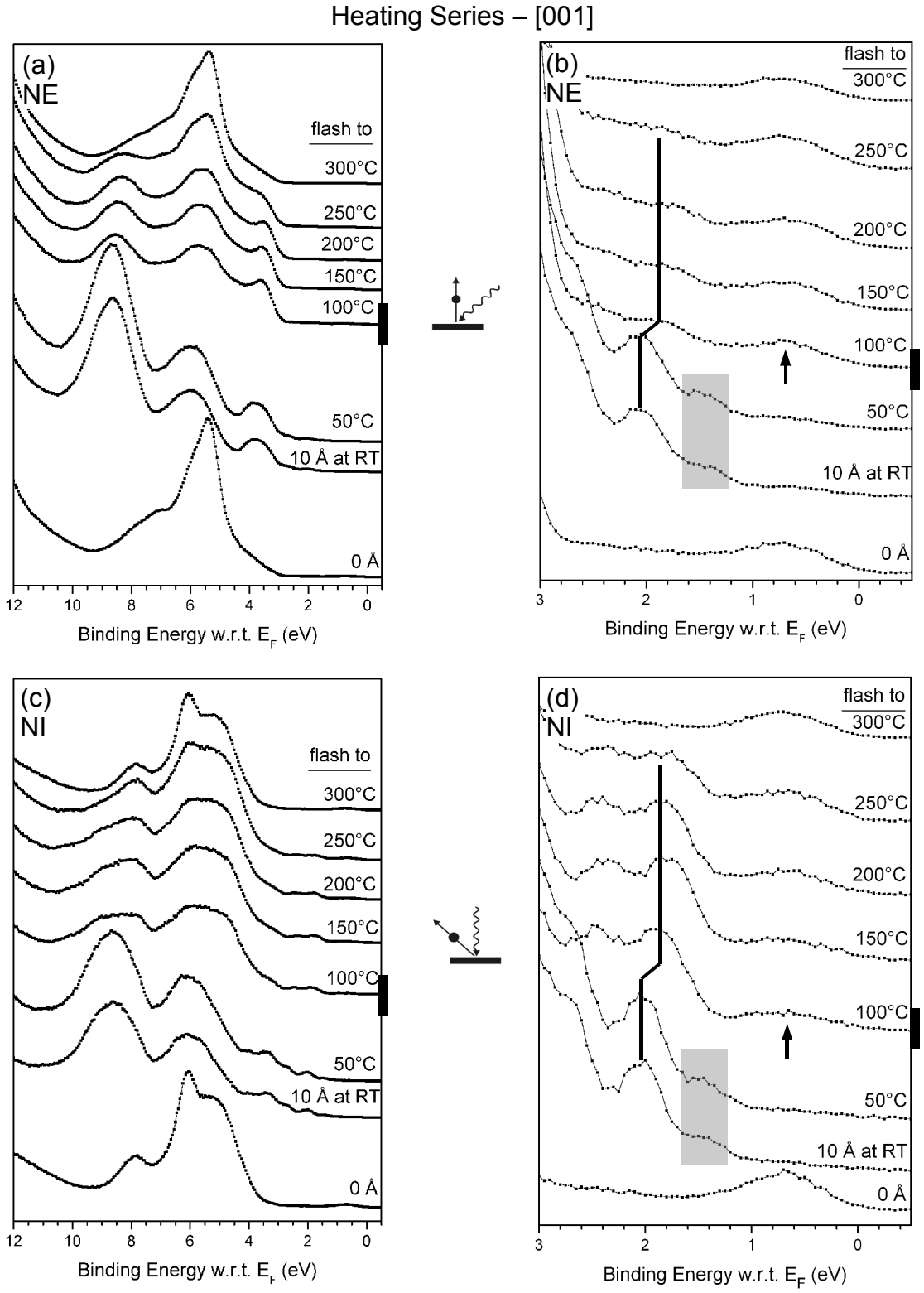

Figure 6.8 *UPS RT heating series measured in the [001] azimuthal geometry. The shaded boxes indicate HOMOs with IP = 5.7 eV. HOMOs with IP = 6.2 eV are marked by lines. Arrows indicates substrate defect states.*

the molecular features degrade, but a completely clean surface is never obtained, as seen in the poorly defined O_{2p} features of the substrate. Evidently, some material is well bound to the surface and remains until the molecules are destroyed by heat, as seen for films grown at LNT and HT. Contrastingly, the substrate features were nearly completely reobtained for the 10 Å film at an apparent temperature of 300°C. Unlike other heating series for films grown at all temperatures (LNT, RT and HT), the material in this film could be completely removed from the substrate by heating. It is unknown whether this behavior is due to uneven heating of the substrate or the a small amount of material involved (10 Å).

6.2 STM and AFM

A direct study of the morphology of coverages 3.5, 35 and 350 Å grown at RT on TiO_2 was done with *in-situ* STM measurements for 3.5 Å and *ex-situ* AFM measurements for 35 Å and 350 Å. The UPS spectra obtained prior to removal from UHV for the AFM measurements of the 35 Å film are provided in Fig.6.5.

Fig.6.9(a) shows STM images of a TiO_2 surface exposed to 3.5 Å of sexiphenyl, which would be enough to cover the TiO_2 with a monolayer of flat lying 6P molecules. Clearly a wetting molecular monolayer is not formed as steps and terraces of the bare substrate can be distinctly seen, together with a large near rectangular needle structure, which can be associated with the 6P molecules. Such structures were found distributed over the substrate with typical dimensions on the order of 600 nm x 60 nm and an apparent height of ~ 6 nm in STM. A statistical analysis of their frequency of appearance is difficult as the 600 nm x 600 nm large scale image of Fig.6.9(a) covers the maximum scan range available to the instrument.

Nevertheless, the regular appearance of one or two such *p*-6P needles per image at various points over the surface suggests a rather uniform distribution with an average needle separation of the order of several hundred nanometers. The orientation of the needles is such that they are all parallel to each other and aligned along the [1$\underline{1}$0] azimuth of the TiO_2 substrate. A close-up of a needle, shown in the bottom of Fig.6.9(a), displays a cloudy structure. However, these structures are not reproducible

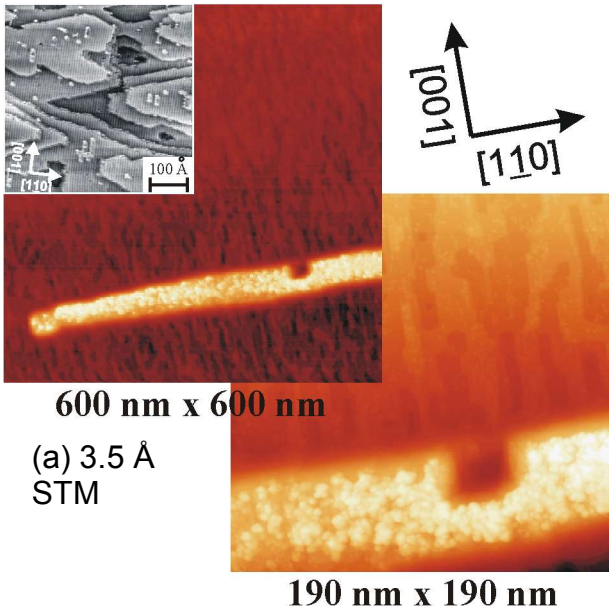

Figure 6.9 *(a) STM of a 3.5 Å coverage. (b), (c) AFM of a 35 Å coverage. (d),(e) AFM of a 350 Å coverage. The TiO_2 [001] substrate azimuth has been marked in all images.*

(b) 35 Å
9x9 µm

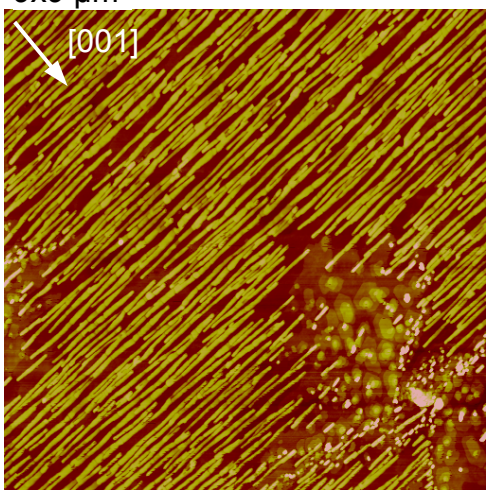

(c) 35 Å
1x1 µm

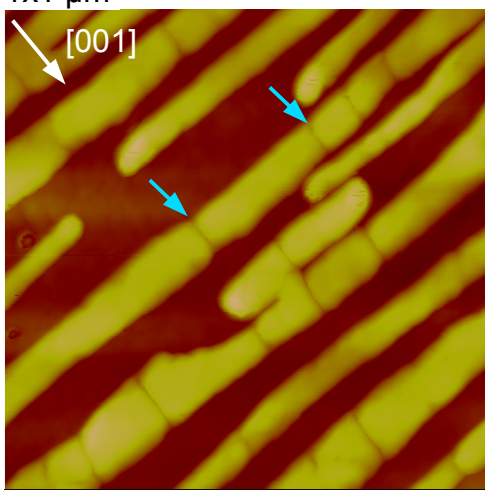

(d) 350 Å
16x16 µm

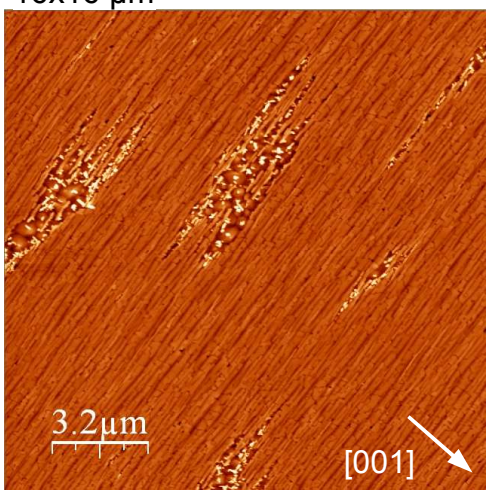

(e) 350 Å
8x8 µm

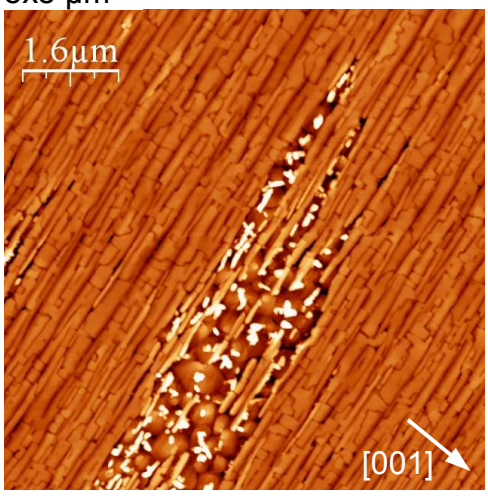

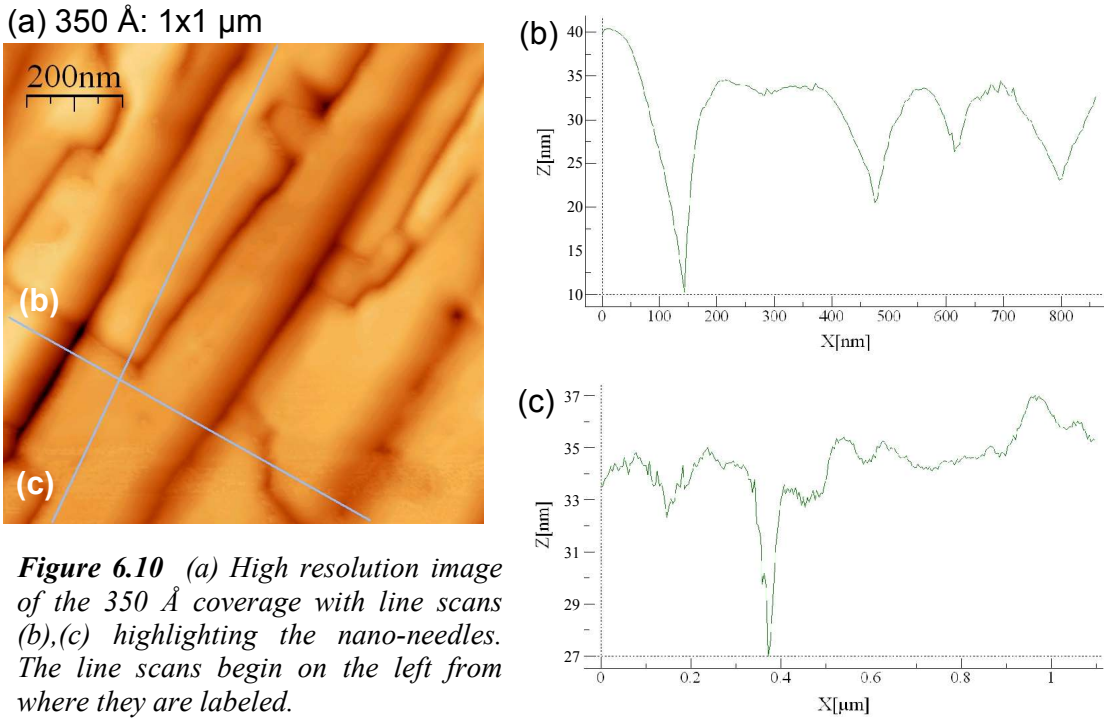

Figure 6.10 *(a) High resolution image of the 350 Å coverage with line scans (b),(c) highlighting the nano-needles. The line scans begin on the left from where they are labeled.*

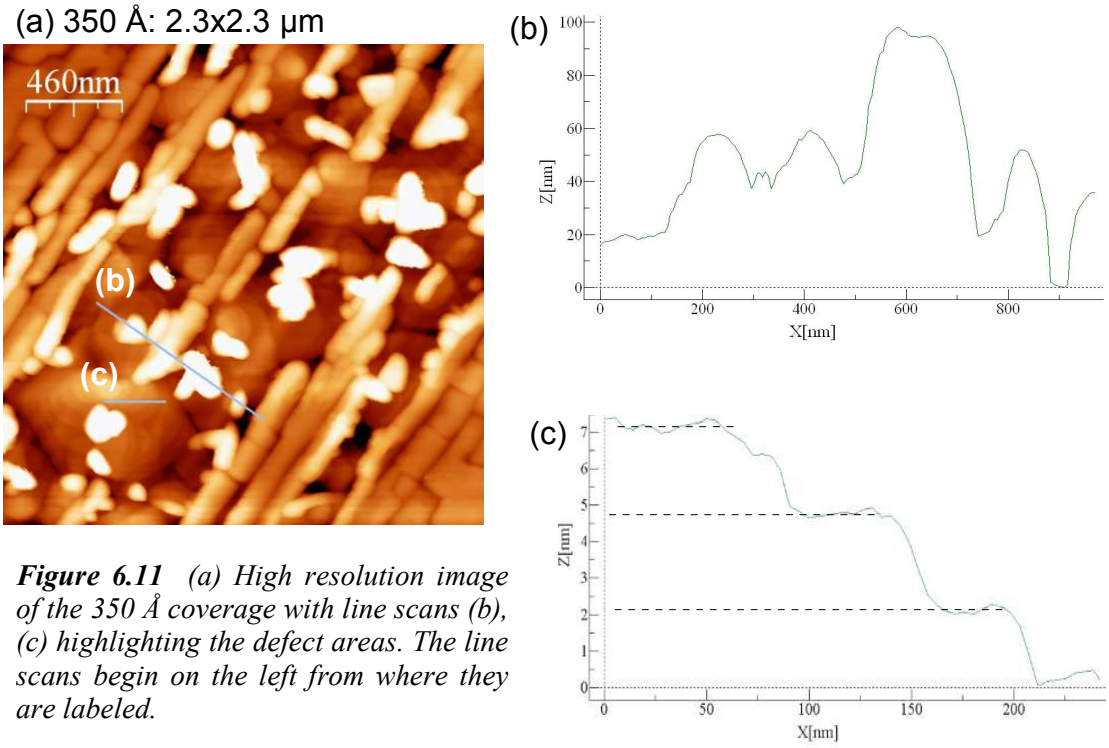

Figure 6.11 *(a) High resolution image of the 350 Å coverage with line scans (b), (c) highlighting the defect areas. The line scans begin on the left from where they are labeled.*

and can be attributed to difficulties in tunnelling through thicker insulating layers. The individual molecular needles are of a regular near rectangular shape, and even occasional regularly shaped defects such as the indentation found in the *p*-6P needle displayed in Fig.6.9(a) have the same near rectangular form.

On increasing the *p*-6P exposure by a factor of ten (35 Å) about 40% of the surface area is covered by 6P needles, as can be seen by the AFM images of Fig.6.9 (b),(c). The large scale AFM image (b) shows that the rise in needle density is also accompanied by a growth in their average dimensions: ~ 1 μm length, ~ 100 nm diameter and 10 nm height. Although there is a scatter in the lateral dimensions of the molecular structures, the heights of the needles (10 ± 1 nm) are uniform over large areas. Long needles up to 8 μm in length have been found, but, as the high resolution AFM image in Fig.6.9(c) shows, they are divided into segments perpendicular to the long needle axes. The segment boundaries (indicated by arrows in Fig.6.9(c)) have an apparent depth of approximately 3 nm, which is probably limited by the tip radius (Fig.6.9(b),(c) were obtained with a carbon whisker tip of radius <5 nm attached to the conventional AFM probe). The segments range from 1 to 0.1 μm in length. These needles are thus quite different from the 6P needles grown on mica [60], [62], which are linear chains of small (~50 nm x 100 nm x 10 nm) crystallites with slightly different crystallographic orientations. At this coverage, areas appear containing structures quite different from the majority nano-needle species (Fig.6.9(b)). These areas also appear at an exposure of 350 Å and will be discussed below.

After an exposure of 350 Å (Fig.6.9(b),(c), Fig.6.10 and Fig.6.11) nearly the entire surface is tiled with the *p*-6P nanostructures (see high resolution image of Fig.6.10(a)). The needles have grown further in size and number with lateral dimensions typically around 2000 nm x 200 nm. Of particular note is the uniform thickness over large areas, with all needles having the same height of approximately 34 ± 2 nm from the lowest point found on the surface, as demonstrated in the line scans of Fig.6.10(b),(c) and in good agreement with the amount of material deposited. The orientation of the *p*-6P nanostructures along the $TiO_2[1\underline{1}0]$ azimuth remains, but some of the needles have met and coalesced, while others show distinct boundaries, the depth of which can reach at least 34 nm, measurement of which is limited by tip diameter <25 nm. This sample was investigated with XRD, AFM and

photoluminescence (PL) measurements over several months in air, and the AFM images degraded over this time with defective areas appearing, however, the rectangular needle structures could still be observed.

The rougher areas that appear at coverages of 35 Å and 350 Å between the needles have been analyzed in more detail in Fig.6.11. The line scans in Fig.6.11 highlight the two types of structures found in these areas: tall structures with heights ranging from 50 to 100 nm from their base and lateral dimension between 100 and 250 nm (b) surrounded by layered structures displaying step edges with heights close to the length of the molecule (~26.5 Å). Similar layered structures were observed at HT and found there to contain standing molecules which have been shown to have a planar conformation, as evidenced by their IP of 5.7 eV. Presumably, these areas contain standing molecules and are responsible for the IP of 5.7 eV seen in the UPS spectra of the 35 Å sample grown at 40°C (Fig.6.5) and the growth series at 40°C (Fig.6.1). The relative scarcity of these areas observed by AFM in the 35 Å sample is reflected in the low intensity of the HOMO with an IP of 5.7 eV in the UPS spectra of this sample (Fig.6.5).

Molecules with both orientations, lying and upright, were observed on both new and older, highly reduced substrate crystals. Furthermore, the 35 Å and 350 Å AFM samples were deposited on irregularly reduced, cracked TiO_2 crystals (photos in Fig.3.3(a),(b)), yet no significant differences were observed in film morphology across the crystal, suggesting that substrate defects and reconstructions play a minor role in film growth.

6.3 XRD

As indicated by the regular shapes of the needle-like nanostructures observed in STM and AFM, these are oriented crystallites. The X-ray diffraction (XRD) data taken from the 350 Å sample of Fig.6.9, 6.10 and 6.11 has been summarized in Fig.6.12 displaying Θ/2Θ scans and pole figures. A comparison of the Θ/2Θ scans of the clean and the *p*-6P covered TiO_2 surface shows that the molecular film leads to an additional diffraction peak at 2Θ = 34.5° (see fig. 2 (a)). This is associated with the

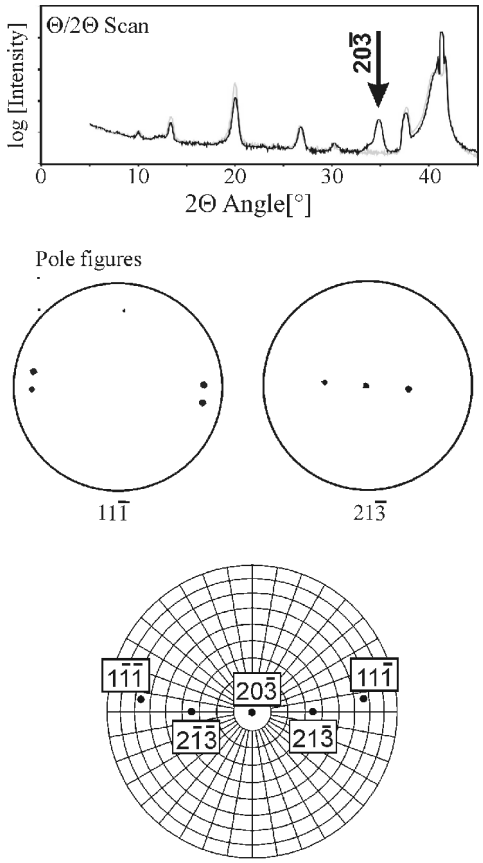

Figure 6.12 *XRD* ***(a)*** *X-ray diffraction (XRD) Θ/2Θ scans of clean (circles) and a 300 Å thick p-6P film (full line) on TiO_2.* ***(b)*** *XRD-pole figures of the 11$\underline{1}$ and 21$\underline{3}$ reflections, the limits of the representations are 60°; reflections from the TiO_2 substrate are indicated as crosses.* ***(c)*** *calculated spherical projection of a single crystal of p-6P.*

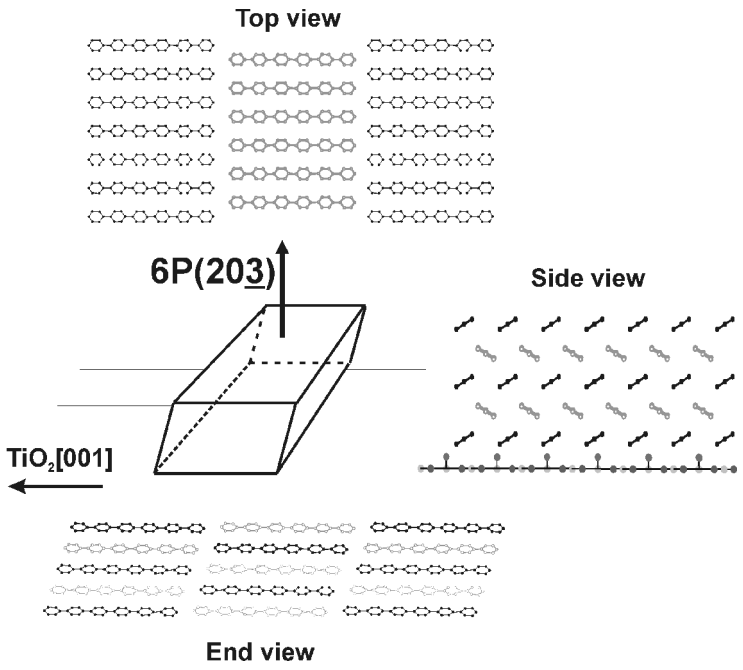

Figure 6.13 *Schematic of a p-6P (20$\underline{3}$) oriented needle indicating the crystallographic structure with respect to the substrate azimuthal directions.*

(20$\underline{3}$) orientation of *p*-6P crystals, based on the β-phase of *p*-6P [29]. The well defined points observed in the XRD - pole figures (see Fig.6.12(b)) illustrate the high degree of epitaxy of the (20$\underline{3}$) oriented crystallites. As can be seen in the comparison of the calculated spherical projection of a single *p*-6P crystal to the observed experimental result, the needles consist of two symmetry equivalent domains, mirrored about the TiO_2(001) plane of the substrate, explaining the segment boundaries observed by AFM. A model of the crystal structure suggested by the XRD data is shown in Fig.6.13.

In conclusion, XRD of the 350 Å thick molecular film showed that all molecules are parallel to each other, to the substrate surface and to the TiO_2[001] azimuthal direction. Moreover, the molecular planes of the molecules have the same angle to the surface of ± 34° (see Fig.6.13). As only the nano-needles seen in the AFM represent enough material for XRD sensitivity, it can be inferred that these needles contain this highly oriented species.

6.4 NEXAFS

As standard laboratory-based XRD is not sensitive to small coverages, where the surface is decorated with isolated nano-needles, and to minority or relatively disordered species, we performed near edge X-ray absorption fine structure (NEXAFS) measurements to determine whether the molecular orientation at very low exposures is the same as for higher exposures.

The assignment of the resonances in Fig.6.14 and 6.15 has been completed according to the scheme introduced in Chapter 3, particularly in Fig.3.8. Two resonances at 299 eV and 304.2 eV, outside the range of Fig.3.8, are labeled here in Fig.6.14(a),(c) as σ*(c) and σ*(d) due to their σ* angular dependency. Resonances at these energies in benzene (Fig.3.8) have been identified as σ* shape resonances by Menzel *et al*. [41].

A thick film (>300 Å) was grown at 0°C in Graz and transported *ex-situ* to BESSY, Berlin. The UPS of this film measured *in-situ* (Fig.6.6) clearly indicates a molecular IP of 6.2 eV, consistent with twisted molecules. In the NEXAFS spectra

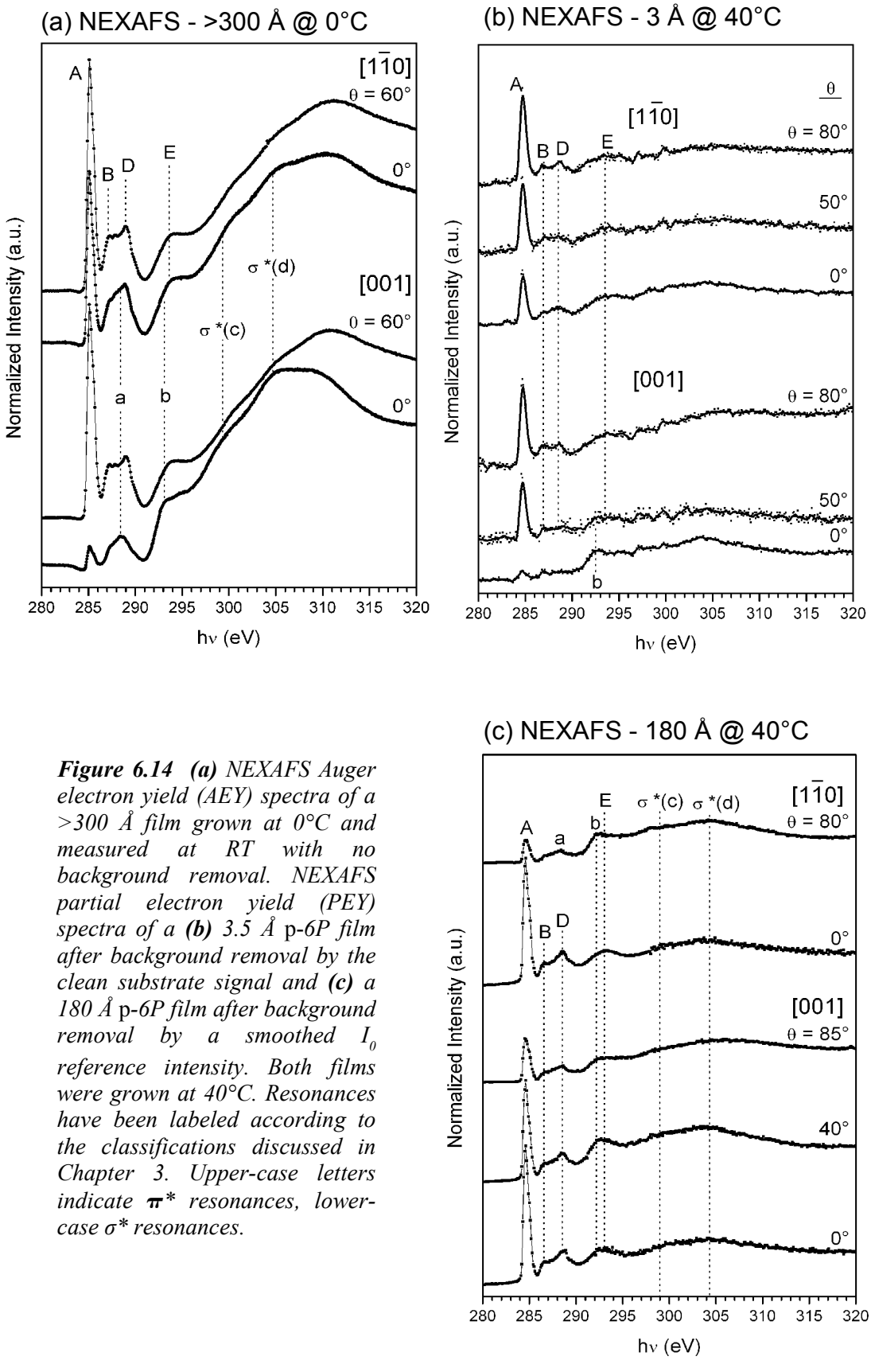

Figure 6.14 ***(a)*** *NEXAFS Auger electron yield (AEY) spectra of a >300 Å film grown at 0°C and measured at RT with no background removal. NEXAFS partial electron yield (PEY) spectra of a* ***(b)*** *3.5 Å* p-*6P film after background removal by the clean substrate signal and* ***(c)*** *a 180 Å* p-*6P film after background removal by a smoothed I_0 reference intensity. Both films were grown at 40°C. Resonances have been labeled according to the classifications discussed in Chapter 3. Upper-case letters indicate* ***π**** *resonances, lower-case σ* resonances.*

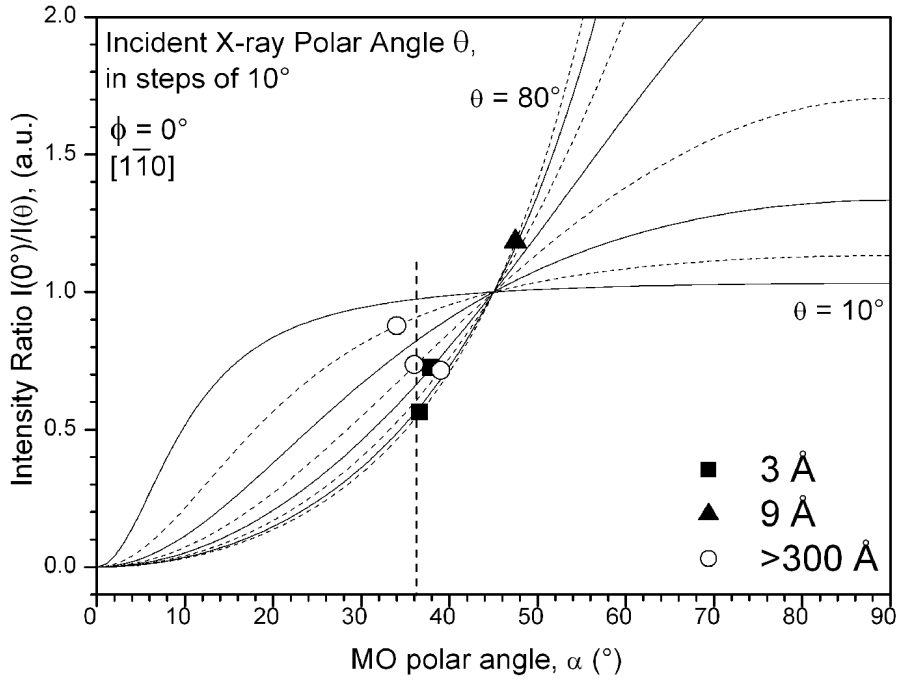

Figure 6.15 *The MO tilt angle α and, hence, the tilt angle of the molecular plane with respect to the surface has been calculated by comparing the ratios of the* π^**(A) resonance intensities from the NEXAFS spectra of the 3 Å, 9 Å and >300 Å coverages with theoretical curves calculated from Eqn.2.5.*

(Fig.6.14(a)), the X-ray polarisation, parallel to the [001] or [1$\underline{1}$0] azimuthal directions of the substrate, clearly reveals the molecular orientation within the self-assembled *p*-6P nano-structures: for normal incidence (NI), with an incidence angle of θ = 0°, in [001] the $C_{1s} \rightarrow \pi^*$(A) transition has little intensity, while in [1$\underline{1}$0] it is a strong feature, indicating that the molecular axis is parallel to [001] and revealing that little to no upright species of molecule is present. In both azimuths the intensity of the π^* transition increases with the angle of incidence (glancing incidence (GI): θ = 60°).

NEXAFS for an exposure of 3 Å at 40°C (comparable to the STM image of Fig.6.9(a)) is shown in Fig.6.14(b). Like the sample grown at 0°C, the X-ray polarization for NI shows a π^*(A) transition nearly invisible in [001], and quite distinct in [1$\underline{1}$0], thus showing the azimuthal orientation of the molecules of the needles at this coverage. Further, the intensity of the π^* transition increases with incidence angle (θ = 80°).

For the clearly azimuthally oriented species of the 3 Å and >300 Å coverages, a detailed analysis of the tilt angle of the aromatic planes was undertaken in the

manner described in Section 2.1.2. The results are summarized in Fig.6.16. The comparison of the π*(A) resonance intensity ratios with theoretical curves calculated from Eqn.2.5 implies that the molecular planes are tilted with respect to the surface plane at an angle of 36 ± 5°, in agreement with the XRD results for the thick films.

As film thickness is increased beyond a coverage of 3 Å growth at 40°C, absorption displays increasingly opposite behavior to that of the 3 Å film and the >300 Å film grown at 0°C. As is seen in the NEXAFS spectra of middle coverages in Fig.6.16(a),(b),(c) and, finally, in a coverage of 180 Å in Fig.6.14(c), as film thickness is increased, the π*(A) resonance gradually, yet consistently changes angular character altogether. In the spectra of the 180 Å coverage, the π*(A) resonance has increased dramatically at NI in both azimuths and decreased in GI, as expected for molecules with an upright orientation. Clearly, at a growth temperature of 40°C, the amount of standing molecules increases with coverage. The deviation of the 9 Å coverage in Fig.6.15 shows the futility of tilt angle determination of the lying species once a standing species is present on the surface, as Eqn.2.5 is intended for only one molecular species.

The overwhelming intensity of the standing species at 180 Å does not seem to correlate with the relatively small amounts of standing molecules compared to lying molecules observed by AFM for coverages of 35 Å and 350 Å in Fig.6.9. This is likely due to the uncertainty in temperature of samples grown at BESSY. It is assumed that a temperature somewhat higher than 40°C would produce a larger amount of standing molecular species.

NEXAFS was used to determine the orientation of the film achieved after brief heating of ~250°C, equivalent to those with the spectral appearance of a monolayer in the heating series of Fig.6.7 and 6.8. It is seen immediately in Fig.6.17 that the amount of material has decreased dramatically after heating, as evidenced by the decrease in signal. Additionally, it appears that all standing species have been removed from the surface, as the intensity of the π*(A) is quite small at NI (θ = 0°) in both azimuthal orientations. Evidently, only a small amount of material is left on the surface after heating, in which the molecules are oriented like the molecules in the nano-needles, lying with their molecular axes parallel to the TiO_2 [001] substrate azimuth.

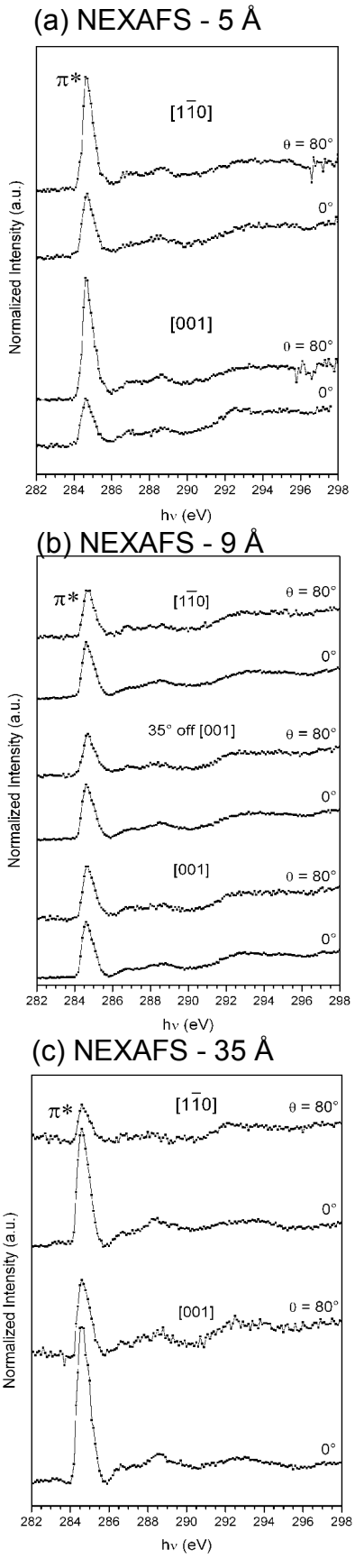

Figure 6.16 *NEXAFS PEY spectra of a* ***(a)*** *5 Å* ***(b)*** *9 Å and* ***(c)*** *35 Å coverages following the evolution of the spectra with increasing coverage at a growth temperature of 40°C.*

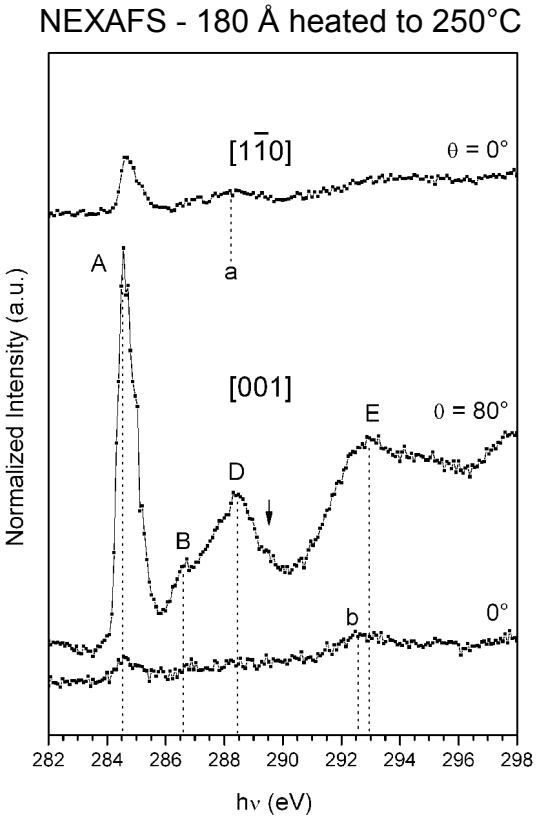

Figure 6.17 *NEXAFS PEY spectra of the 180 Å film of Fig.6.14(c) after heating to ~250°C.*

6.5 RDS

It is known from XRD and NEXAFS that the *p*-6P molecules grown on TiO_2 at RT are highly orientated, lying with their molecular axes all parallel to the [001] substrate azimuth. Since 6P absorbs light in the region immediately above 3 eV along the molecular axis, such an orientation is expected to produce a strong RDS signal, as seen at LNT (Fig.4.8). To determine how this known orientation appears in RDS, *in-situ* measurements were performed during growth at RT (Fig.6.18(a)).

Although the RDS signal of the TiO_2(110) substrate (0 Å in Fig.6.18(a)) displays high anisotropy in the reflection of light polarized along the two azimuthal directions of the substrate throughout the entire spectral range of the instrument, particularly in regions above 3 eV where the optical absorption of 6P is found [55], as *p*-6P is deposited onto the substrate the RDS signal increases dramatically above a photon energy of 3 eV. The high amount of anisotropy reflects the highly oriented nature of the film. Since the molecules are expected to absorb light polarized along the molecular axis, and since reflection depends strongly on absorption, RDS clearly indicates that they are oriented primarily with their molecular axes parallel to the [001] substrate azimuthal direction, in good agreement with the XRD and NEXAFS results. The features that cross from negative values to positive values above a coverage of around 200 Å can be attributed to interference effects as the film thickness approaches the wavelength of the light used for measurement.

When the completed 320 Å film is heated to 150°C (Fig.6.18(b)), there is no change in the RDS signal, indicating that the film grown at RT is stable up to this temperature and does not change orientation. As this film is heated further to 250°C, a substantial change takes place where the RDS spectrum takes on the spectral appearance of the clean substrate or a low coverage (≤3.5 Å), indicating that most of the material has been removed from the substrate, consistent with heating results obtained in UPS and NEXAFS.

6.6 Photo activity

Photoluminescence (PL) measurements were performed *ex-situ* on the 350 Å

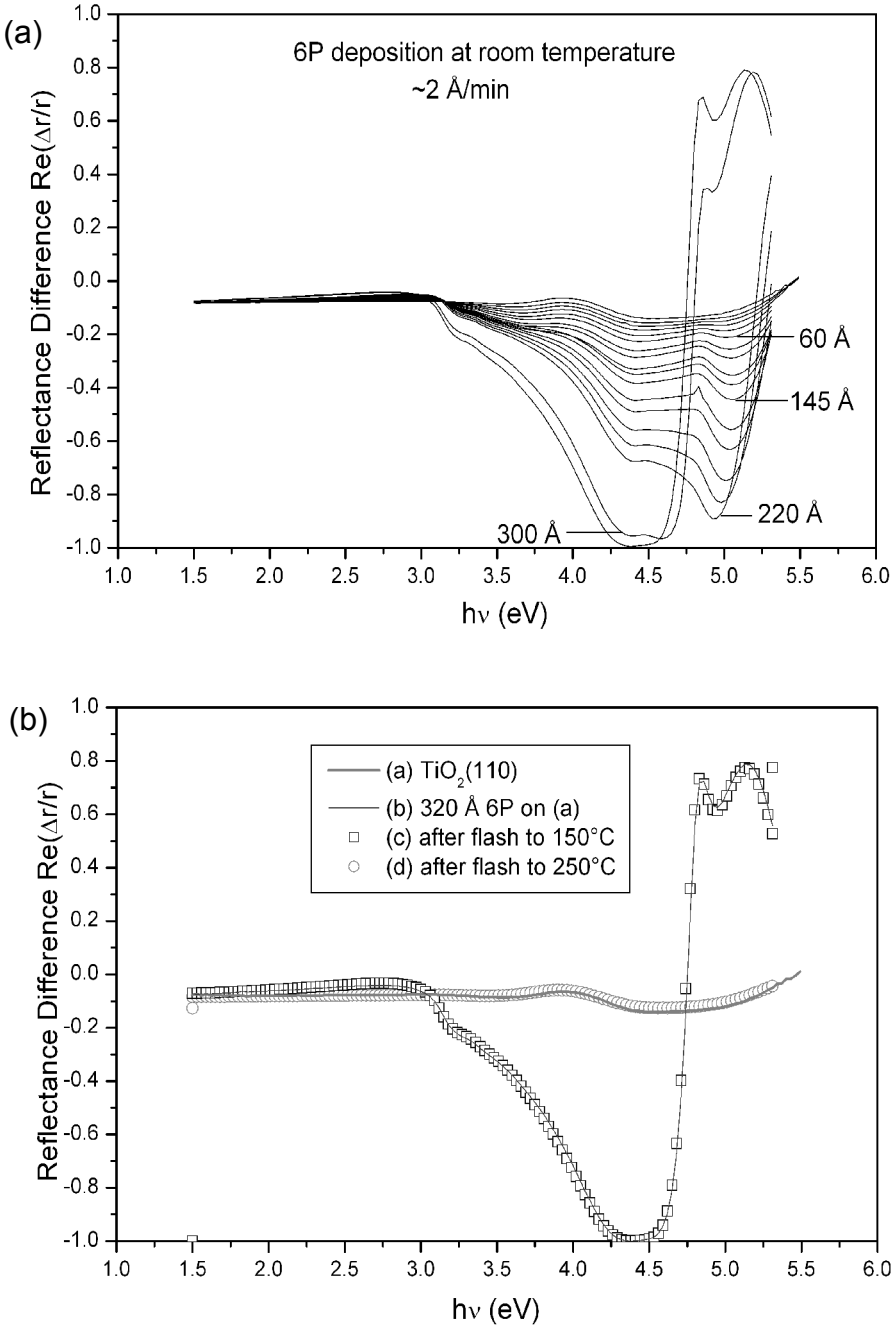

Figure 6.18 (a) *A* p-*6P film was deposited at RT (40°C) and subsequent RDS spectra were taken.* ***(b)*** *The total of 320 Å 6P was then flashed to two temperatures, 150°C and 250°C, and measured by RDS. Negative values indicate lower reflectance in the [001] azimuthal direction.*

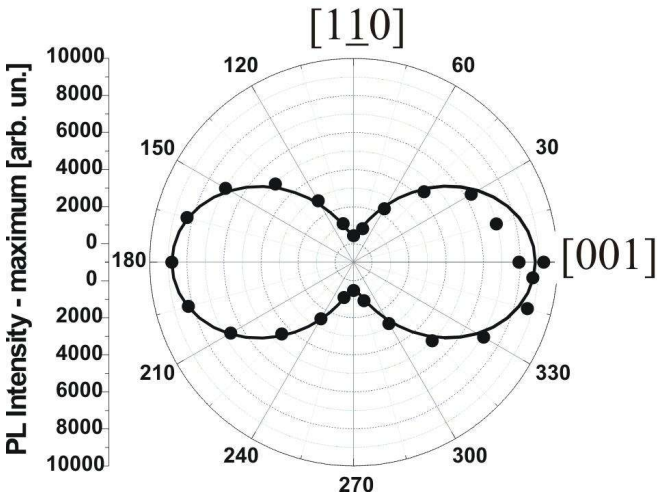

Figure 6.19 *Photoluminesence PL measurements were performed on the 350 Å sample seen in the AFM and XRD sections of this chapter. The results to the left show the film has a dichroic ratio greater than 22.*

film featured in the AFM and XRD results seen in Fig.6.9(d),(e), 6.10, 6.11 and 6.12. The results are presented in Fig.6.19 and reveal the high anisotropy of PL in the two azimuthal orientations. This film has a dichroic ratio of more than 22.

p-6P crystals begin to absorb light above an energy of around 3 eV [55]. Because the reflection of a film depends heavily on its absorption, an approximate absorption spectrum can be simulated by substracting the RDS signal of the TiO_2 substrate from that of a thin film (0.65 Å), as displayed in Fig.6.20(b). At this small coverage, three well-defined peaks can be found in the resulting spectrum, located at 3.5 eV, 4.2 eV and 5.0 eV, which have been fitted by Gaussian peaks. This spectrum can be compared to the calculated absorption spectra of Zojer *et al*. in Fig.6.20(a) [55]. The calculated spectra show multiple absorption peaks between 3 and 5.5 eV. Since the RDS signal is the difference between the reflection along the [001] and [1$\underline{1}$0] substrate azimuths, the absorption spectrum measured corresponds to the calculation at $\theta = 90°$ minus that at $\theta = 0°$. The comparison of the calculated and measured absorption spectra in Fig.6.20 reveals a great amount of similarity, much more so than the experimental absorption spectra obtained from rubbed samples in the original article [55], reflecting the truly highly-oriented nature of *p*-6P films grown on TiO_2.

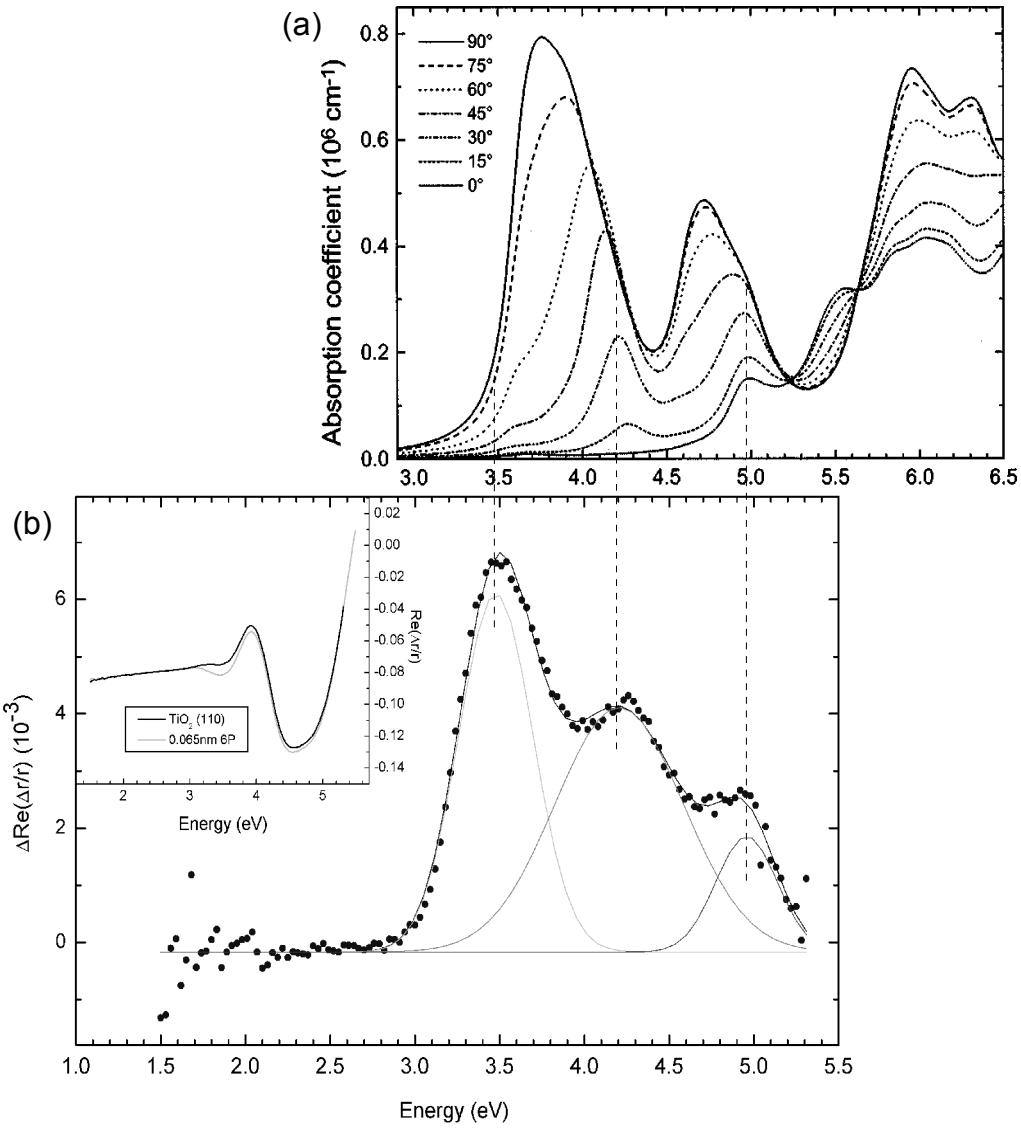

Figure 6.20 (a) *Calculated absorption spectra of a three dimensional* p-*6P crystal from Zojer* et al. *[55]. The curves were calculated for angles of 0° to 90° between the molecular axis and the wave vector. For θ = 90°, the polarization of the incident light is parallel to the molecular axis.* ***(b)*** *The difference between the RDS signal of a sub-'ML' dose (0.65 Å) and the substrate. The difference has been fit with 3 Gaussian peaks. The inset shows the original RDS spectra.*

Fit Parameters
Model: Gauss

χ^2	= 7.4464E-8
y_0	-0.00017
x_{c1}	3.47748 eV (energy)
w_1	0.43867 eV (width)
A_1	0.00345 eV (area)
x_{c2}	4.20489
w_2	0.75547
A_2	0.00405
x_{c3}	4.9564
w_3	0.36327
A_3	0.00092

Chapter 7

Conclusions

The growth of *para*-sexiphenyl (6P) films on TiO_2(110) has been studied over a wide range of temperatures from -190°C to 150°C by ultraviolet photoemission spectroscopy (UPS), atomic force microscopy (AFM) and reflection difference spectroscopy (RDS). In addition, X-ray diffraction (XRD), near-edge X-ray absorption fine structure (NEXAFS) spectroscopy and photoluminesence (PL) were used in the characterization of films grown at room temperature (RT). Growth at various temperatures produced two types of films, each with its own molecular orientation and conformation.

For growth at liquid nitrogen temperature (LNT), -190 ± 5°C, the molecules were found to lie parallel to the surface and the TiO_2 [001] azimuth. Further, the molecules were found to have an IP of 6.3 ± 0.1 eV, indicating they maintain their gas-phase conformation (twisted). From the thermal behaviour, it is suggested that the films are locked into a crystalline structure even at LNT.

Growth at high temperature (HT), 150°C ± 10°C, produced films of standing molecules, whose molecular axes were found to have a tilt angle of 77 ± 5° with respect to the substrate plane. The molecules possessed an IP of 5.7 ± 0.1 eV, indicating a planar conformation. Moreover, films of 6P on TiO_2 grown at HT were also seen to grow anisotropically, with preferential molecular diffusion in the

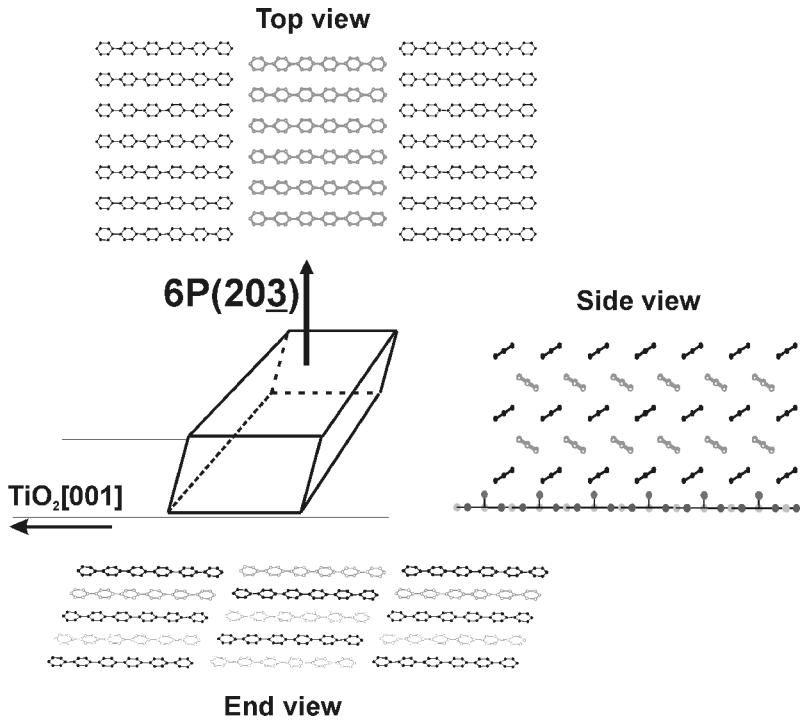

Figure 7.1 *Schematic of a p-6P (20$\underline{3}$) oriented needle indicating the crystallographic structure with respect to the substrate azimuthal directions.*

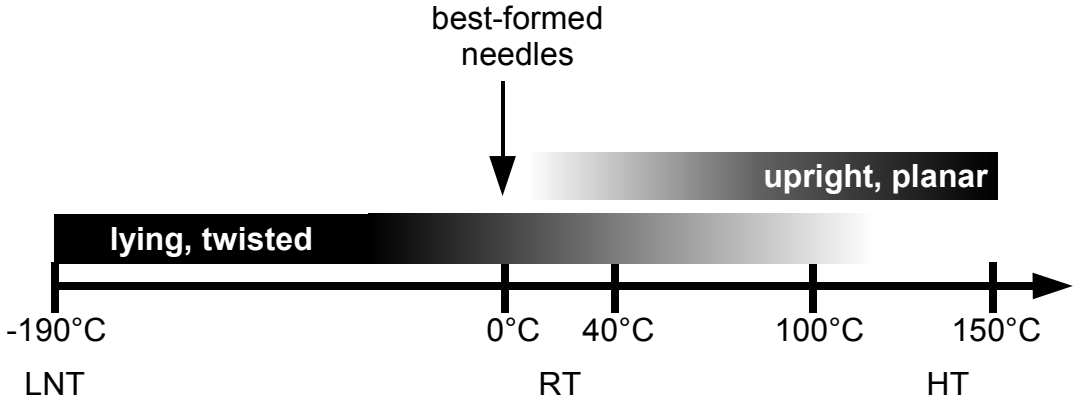

Figure 7.2 *Phase diagram over the entire growth range studied.*

direction of the [001] substrate azimuth and a preferential tilt in the [001] direction. For low coverages, twisted planar molecules are suggested in UPS. Whether the upright molecules form on a monolayer of lying molecules or whether the latter are incorporated into the film of upright molecules at higher coverages is still an open question.

When grown below room temperature (RT), 0°C ± 10°C, *p*-6P assembles into crystalline needle-like nanostructures-structures, which are found to be exclusively oriented along the [1$\underline{1}$0] substrate azimuth. The individual molecules however are oriented along the [001], i.e. perpendicular to the needle axes. They are found to maintain the twisted conformation, as for growth at LNT, and their molecular planes are found to have the same angle of ± 34° with respect to the substrate surface plane. The *p*-6P nano-needles display only a single crystalline orientation, the *p*-6P(20$\underline{3}$), whose relation to the TiO2(110) surface can be seen in the schematic in Fig.7.1. They already formed at submonolayer coverages, decorating the surface with isolated needles, while at higher exposures the needles grow until they completely tile the surface with a film of uniform thickness.

As the growth temperature is raised to 40°C and above, increasing amounts of 6P molecules adopt the upright HT orientation and begin to form rougher areas in the nano-needle film. The molecules in these areas are found to have a planar conformation, as for HT growth. A phase diagram of the growth of *p*-6P on TiO_2 over the entire growth-temperature range used in this thesis can be found in Fig.7.2.

Strikingly similar absorption behavior between 190 Å films grown at LNT and RT, as seen in the RDS of Fig.7.3, demonstrates the similar molecular orientation in these films, in which the molecules are perfectly parallel to each other and to the substrate [001] azimuth. The high quality of the absorption spectrum inferred from the RDS data in Chapter 6 and its agreement with calculations of a 6P crystal is a further testament to the crystallographic order of the nano-needles. The RDS of growth at LNT and RT stand in contrast to the film grown at HT, which consists of upright molecules. Regardless of the orientation, however, the anisotropic nature of the substrate was impressed upon molecular film growth, having its greatest effect at RT.

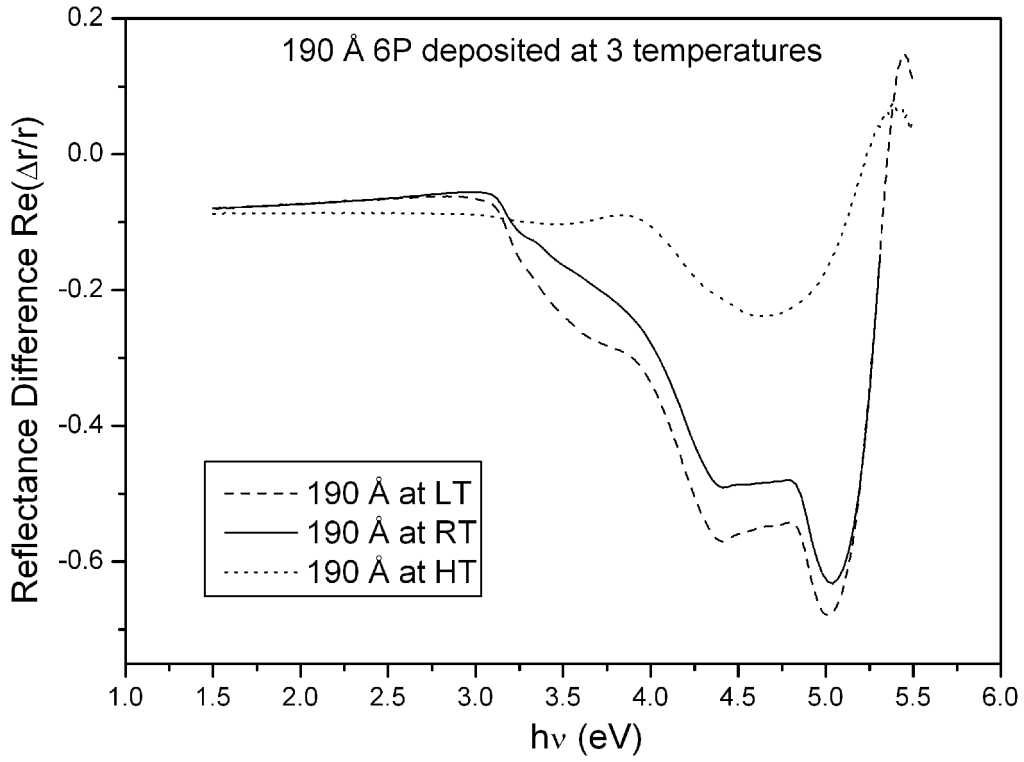

Figure 7.3 *Comparison of RDS signal of 190 Å 6P deposited at LNT, RT and HT.*

The NEXAFS results clearly show that the highly crystalline needles are formed at low exposures for RT deposition, and XRD and AFM reveal that they grow in size with increasing coverage. This is in contrast to the *p*-6P needle growth on mica, where the initial stage consists of very small randomly distributed crystallites, which aggregate into long islands [62]. Why the unique morphology and crystallite orientation observed here arises on the TiO_2 substrate is still unresolved. Clearly, the *p*-6P molecules are mobile on the TiO_2 surface and calculations for aromatic monomers (benzene, pyridine) on TiO_2 indicate that they adopt edge-on geometries hydrogen bonded to the oxygen rows and are highly mobile along them [56]. Indeed, for growth at HT, diffusion is clearly favored along the atomic oxygen rows even though the final orientation of the molecules is perpendicular to the substrate plane. Therefore, it is believed that the individual p-6P molecules are oriented by the atomic rows and are channeled along the [001] direction of TiO_2 such that when they meet and nucleate they are already near the orientation that they adopt in the [1$\underline{1}$0] oriented needles [63].

The novel morphology obtained for RT growth combined with the unique orientation of the molecules, all parallel to each other and the substrate and all with their molecular planes tilted with respect to the substrate, appears useful for both planar LEDs and lateral FET applications. As growth temperatures increase, HT-like areas in the film would present problems for use in devices, although the molecular orientation at HT, perpendicular to the surface plane, offers its own possibilities (e.g. traditional FET applications). The ability to control crystalline orientation of the molecular film, in combination with the TiO_2 substrate, which can be prepared as either insulating or conducting, appears promising for both technology and basic research.

Bibliography

[1] G. Koller, R.I.R. Blyth, S.A. Sardar, F.P. Netzer, M.G. Ramsey, *Appl. Phys. Lett.* 76 (2000) 927-929

[2] R.I.R. Blyth, R. Duschek, G. Koller, F.P. Netzer, M.G. Ramsey, *J. Appl. Phys*. 90 (2001) 270

[3] J. Ivanco, B. Winter, F.P. Netzer, M.G. Ramsey, *Adv. Mat*. 15 (2003) 1812-1815

[4] Y.-Y. Lin, D.J. Grundlach, S.F. Nelson, T.N. Jackson, *55th Device Research Conference Digest* (1997) 60

[5] H. Yanagi, S. Okamoto, *Appl. Phys. Lett*. 71 (1997) 2563-2565

[6] D.J. Gundlach, Y.-Y. Lin, T.N. Jackson, D.G. Schlom, *Appl. Phys. Lett*. 71 (1997) 3853-3855

[7] C.D. Dimitrakopoulos, P.R.L. Malenfant, *Adv. Mat*. 14 (2002) 99

[8] J. Fraxedas, *Adv. Mat*. 14 (2002) 1603

[9] H. Yanagi, T. Ohara, T. Morikawa, *Adv. Mat*. 13 (2001) 1452-1455

[10] F. Balzer, V.G. Bordo, A.C. Simonsen, H.-G. Rubahn, *Phys. Rev. B* 67 (2003) 115408

[11] G. Koller, F.P. Netzer, M.G. Ramsey, *Appl. Phys. Lett*. 83 (2003) 563-565

[12] Y. Ohmori, T. Tsukagawa, H. Kajii, *Displays* 22 (2001) 61

[13] C. Winder, A. Andreev, H. Sitter, G. Matt, N.S. Sariciftci, D. Meissner, *Syn. Met*. 139 (2003) 573

[14] L. Athouël, G Froyer, M.T. Riou, M. Schott, *Thin Solid Films* 274 (1996) 35-45

[15] S. Blumstengel, F. Meinardi, R. Tubino, A. Borghesi, *Syn. Met*. (2003) 961-962

[16] R. Resel, I. Salzmann, G. Hlawacek, C. Teichert, B. Koppelhuber, B. Winter, J.K. Krenn, J. Ivanco, M.G. Ramsey, *Organic Electronics* 5 (2004) 45-51

[17] S. Eck, Master's Thesis, Karl-Franzens University, Graz (2000)

[18] S. Hüfner, *Photoelectron Spectroscopy* (Springer-Verlag, 1995)

[19] G. Ertl, J. Küppers, *Low Energy Electrons and Surface Chemistry* (VCH Verlagsgesellschaft mbH, 1985)

[20] J. Stöhr, *NEXAFS Spectroscopy* (Springer-Verlag, 1992)

[21] W.L. Jorgensen, L. Salem, *The Organic Chemist's Book of Orbitals* (Academic Press, 1973)

[22] J. Schnadt, J. Schiessling, J.N. O'Shea, S.M. Gray, L. Patthey, M.K.-J. Johansson, M. Shi, J. Krempasky, J. Åhlund, P.G. Karlsson, P. Persson, N. Mårtensson, P.A. Brühwil, *Surf. Sci*. 540 (2003) 39-54

[23] A. Schoell, Y. Zou, Th. Schmidt, R. Fink, E. Umbach, *J. Electron. Spectrosc. and Relat. Phenom*. 129 (2003) 1-8

[24] M.A. Van Hove, W.H. Weinberg, C.-M. Chan, *Low-Energy Electron Diffraction* (Springer-Verlag, 1986)

[25] B. Winter, J. Ivanco, F.P. Netzer, M.G. Ramsey, *Thin Solid Films* 433 (2003) 269-273

[26] L.D. Sun, M. Hohage, P. Zeppenfeld, R.E. Balderas-Navarro, *Phys. Stat. Sol. C* 0 (2003) 3022 - 3026

[27] H. Plank, R. Resel, S. Purger, J. Keckes, A. Thierry, B. Lotz, A. Andreev, N.S. Sariciftci, H. Sitter, *Phys. Rev. B* 64 (2001) 235423

[28] S. Weber, J. Appl. Cryst. 29 (1996) 306

[29] K.N. Baker, A.V. Fratini, T. Resch, H.C. Adams, E.P. Socci, B.L. Farmer, *Polymer* 34 (1993) 1571-1587

[30] G. Koller, S. Surnev, M.G. Ramsey, F.P. Netzer, *Surf. Sci. Lett*. 559 (2004) 187-193

[31] G. Koller, Ph.D. Thesis, Karl-Franzens University (2002)

[32] U. Diebold, *Surf. Sci. Rep*. 48 (2003) 53-229

[33] C. Castellarin-Cudia, Ph.D. Thesis, Karl-Franzens University, Graz (2003)

[34] K. Seki, U.O. Karlsson, R. Engelhardt, E.-E. Koch, W. Schmidt, *Chem. Phys*. 91 (1984) 459-470

[35] H. Ishii, S. Narioka, K. Edamatsu, K Kamiya, S. Hasegawa, T. Ohta, N. Ueno, K. Seki, *J. Electron. Spectrosc. .Relat. Phenom*. 76 (1995) 553-558

[36] M.G. Ramsey, D. Steinmüller, M. Schatzmayr, M. Kiskinova, F.P. Netzer, *Chem. Phys*. 177 (1993) 349-361

[37] M.S. Miao, P.E. Van Camp, V.E. Van Doren, J.J. Ladik, J.W. Mintmire, *J. Chem Phys.* 109 (1998) 9623

[38] M.G. Ramsey, F.P. Netzer, D. Steinmüller, D. Steinmüller-Nethl, D.R. Lloyd, *J. Chem. Phys*. 97 (1992) 4489-4495

[39] H. Oji, R. Mitsumoto, E. Ito, H. Ishii, Y. Ouchi, K. Seki, T. Yokohama, T. Ohta, N. Kosugi, *J. Chem. Phys*. 109 (1998) 10409

[40] G. Koller, R.I.R. Blyth, S.A. Sardar, F.P. Netzer, M.G. Ramsey, *Surf. Sci*. 536 (2003) 155-165

[41] D. Menzel, G. Rocker, H.-P. Steinrück, D. Coulman, P.A. Heimann, W. Huber, P. Zebisch, D.R. Lloyd, *J. Chem. Phys*. 96 (1992) 1724-1734

[42] D. Duflot, J.-P. Flament, J. Heinesch, M.-J. Hubin-Franskin, *J. Electron. Spectrosc. Relat. Phenom*. 113 (2000) 79-90

[43] M.J. Kong, A.V. Teplyakov, J.G. Lyubovitsky, S.F. Bent, *Surf. Sci*. 411 (1998) 286-293

[44] P. Zebisch, M. Stichler, P. Trischberger, M. Weinelt, H.-P. Steinrück, *Surf. Sci*. 396 (1998) 61-77

[45] J.A. Horsley, J. Stöhr, A.P. Hitchcock, D.C. Newbury, A.L. Johnson, F. Sett, *J. Chem. Phys*. 83 (1985) 6099-6107

[46] T. Sekipuchi, Y. Baba, H.I. Sekiguchi, M. Imamura, N. Matsubayashi, H. Shimada, *Appl*. *Surf. Sci*. 169-170 (2001) 287-291

[47] Y. Ma, F. Sette, G. Meigs, S. Modesti, C.T. Chen, *Phys. Scr*. 41 (1990) 833

[48] M.G. Ramsey, D. Steinmüller, F.P. Netzer, T. Schedel, A. Santaniello, D.R. Lloyd, *Surf. Sci.* 251/252 (1991) 979-984

[49] L. Athouël, R. Resel, N. Koch, F. Meghdadi, G. Froyer, and G. Leising, *Syn. Met.* 101 (1999) 627-628

[50] B. Winter, Master's Thesis, Karl-Franzens University, Graz (2003)

[51] J. Ivanco, J.R. Krenn, M.G. Ramsey, F.P. Netzer, T. Haber, R. Resel, A. Haase, B. Stadlober, G. Jakopic, *J. Appl. Phys*. 96 (2004) 2716-2723

[52] B. Winter, J. Ivanco, I. Salzman, R. Resel, F.P. Netzer, M.G. Ramsey, *Langmuir* 20 (2004) 7512-7516

[53] F.P. Netzer, M.G. Ramsey, *CRC Crit. Rev. Solid State Mater. Sci*. 17 (1992) 397

[54] R. Duschek, F. Mittendorfer, R.I.R. Blyth, F.P. Netzer, J. Hafner, M.G. Ramsey, *Chem. Phys. Lett*. 318 (2000) 43

[55] E. Zojer, N. Koch, P. Puschnig, F. Meghdadi, A. Niko, R. Resel, C. Ambrosch-Draxl, M. Knupfer, J. Fink, J.L. Brédas, G. Leising, *Phys. Rev. B* 61 (2000) 16538-16549

[56] T. Sasaki, K. Fukui, Y. Iwasawa, *Stud. Surf. Sci. Catal*. 132 (2001) 749

[57] A. Andreev, Personal communication

[58] R. Resel, M.G. Ramsey, Personal communication

[59] H. Yanagi, T. Morikawa, *Appl. Phys. Lett.* 75 (1999) 187

[60] A. Andreev, G. Matt, C.J. Brabec, H. Sitter, D. Badt, H. Seyringer, N.S. Sariciftci, *Adv. Mat*. 12 (2000) 629

[61] F. Balzer, H.G. Rubahn, *Surface Science* 548 (2004) 170

[62] H. Plank, R. Resel, H. Sitter, A. Andreev, N.S. Sariciftci, G. Hlawacek, C. Teichert, A. Thierry, B. Lotz, *Thin Solid Films* 443 (2003) 108

[63] G. Koller, S. Berkebile, J. Krenn, G. Tzvetkov, G. Hlawacek, O. Lengyel, F.P. Netzer, M.G. Ramsey, C. Teichert, R. Resel, *Adv. Mat*. (in press)

Figure Index

Appendix

```
/*-------------------------------------------------------------------------*
 * File Name:    Nexafs.c

 * Purpose:      Origin programs for NEXAFS analysis using Origin C. This code and the
                 required template files are found on the CD included in thesis. The functions
                 in this program can be called in the Script Window in Origin after it has been
                 compiled in the Code Builder.
*-------------------------------------------------------------------------*/


////////////////////////////////////////////////////////////////////////////
#include <origin.h>
#include <wksheet.h>
#include <data.h>
#include <string.h>
#include <graph.h>
#include <OrgObj.h>
#include <page.h>

////////////////////////////////////////////////////////////////////////////


/*      The functions min and max should be included in the Origin C builder, but the
        program doesn't work without including them here. */

double min(Dataset &aa)
{
        BasicStats stat;
        stat.min = -1;
        Data_sum(&aa, &stat);
        return stat.min;
}

double max(Dataset &aa)
{
        BasicStats stat;
        stat.max = -1;
        Data_sum(&aa, &stat);
        return stat.max;
}



/*      The function norm divides a whole column by the average of the column values in the
        specified energy range.
        wksName = worksheet name
        colNum = column number (starting with 0 from left) */

void norm(string wksName, int colNum)
{
        Worksheet wks(wksName);
        Dataset dS(wksName, colNum), dE(wksName, 0);
        Curve crv1(wks,colNum);
```

```
	double dE1=dE[0], dE2=dE[1], dYfromX, E, Sum;
	double dEinc=dE2-dE1;			//Energy value separation
	int i;

	//Sums column values for C_K-NEXAFS, pre-edge energy range 280-282 eV

	if (dE1==280)
		for (E=dE1, Sum=0, i=0; E <= 282; E+=dEinc)
		{
			i++;
			dYfromX = Curve_yfromX(&crv1, E);
			Sum+=dYfromX;
		}

	//Sums column values for C_K-NEXAFS, pre-edge energy range 282-282.5 eV

	else if (dE1==282)
		for (E=dE1, Sum=0, i=0; E <=282.5; E+=dEinc)
		{
			i++;
			dYfromX = Curve_yfromX(&crv1, E);
			Sum+=dYfromX;
		}

	//Sums column values for S_L-NEXAFS, pre-edge energy range 162-162.5 eV

	else if (dE1==162)
		for (E=dE1, Sum=0, i=0; E <=162.5; E+=dEinc)
		{
			i++;
			dYfromX = Curve_yfromX(&crv1, E);
			Sum+=dYfromX;
		}

	//Sums column values for arbitrary pre-edge energy range E_1 to E_1+0.5 eV

	else for (E=dE1, Sum=0, i=0; E <= (dE1+0.5); E+=dEinc)
		{
			i++;
			dYfromX = Curve_yfromX(&crv1, E);
			Sum+=dYfromX;
			if(i==1) printf("Check the column! Weird stuff!\n");
		}

	/*Calculates average, divides all column values by the average and then copies new
	normalized value into original column */

	double Div=Sum/i;
	vector Vector1(dS), Vector2;		//load dataset into vector
	Vector2=Vector1/Div;			//normalize column
	dS=Vector2;				//copy normalized values into new worksheet
}


/*	The function plotraw plots a series of worksheets individually (x = 1st column, y = 2nd
	column), which have the same prefix and a numeral suffix. The plots are automatically
	resized to the data and labeled with the worksheet name.
	Input:
	prefix = worksheet prefix
```

```
        num1 = beginning suffix number
        num2 = ending suffix number */

void plotraw(string prefix, int num1, int num2)
{
        printf("Graphed:\n");

        for(int i=num1; i <= num2; i++)                 //cycle through worksheets
        {
                string suffix ((string) i);
                string name = prefix + suffix;

                Worksheet wks(name);

                if(wks.IsValid()==FALSE) continue;      //check if worksheet exists

                printf("%s\n",name);

                Dataset ds(wks,1), de1(wks,0);
                Curve cv(wks,1);                        //assign data to x and y
                ASSERT(cv.IsValid());
                GraphPage grph;                         //create graph from template
                string strTemplate="nexafs.otp";
                BOOL bOK = grph.Create(strTemplate, CREATE_VISIBLE);

                if (!bOK)
                return;

                GraphLayer grlay = grph.Layers(0);      //assign graph layer
                ASSERT(grlay.IsValid());

                bOK = 0 <= grlay.AddPlot(cv);           //graph data
                if (!bOK)
                return;


                double maximum(max(ds));                //find max./min. values in data
                double minimum(min(ds));

                GraphLayer gl = Project.ActiveLayer();
                if(gl)
                {
                        Scale scy(gl.Y);                //set y scale
                        scy.From = maximum*0.95;
                        scy.To = minimum*1.04;


                        if(de1[0]==162)                 //set x scale (for C_K- or S_L-edge)
                        {
                                Scale scx(gl.X);
                                scx.From = 162;
                                scx.To = 202;
                                scx.Inc = 5;
                        }
                        else
                        {
                                Scale scx(gl.X);
                                scx.From = 280;
                                scx.To = 320;
                                scx.Inc = 5;
```

```
                }
            }

        grph.Rename(name+"g");                  //name graph worksheet name+"g"

        string LTcmd;                           //add worksheet name as label to
        string str1 = "label -d 300 4600 ";     //graph
        string str2 = ";";
        LTcmd = str1+name+str2;
        LT_execute(LTcmd);
        }

        printf("Finished!\n");
}


/*      The function ploti0 plots a series of worksheets, which have the same prefix and a
        numeral suffix, in one graph (x = 1st column). The plots are automatically resized to
        the data and labeled with the worksheet name.(meant for use with I0 curves)
        Input:
        prefix = worksheet prefix
        num1 = beginning suffix number
        num2 = ending suffix number
        colNum = column number of y data (starts with 0 from left)*/

void ploti0(string prefix, int num1, int num2, int colNum)
{
        printf("Graphed:\n");

        GraphPage grph;                         //create graph from template
        string strTemplate="nexafsi0.otp";
        BOOL bOK = grph.Create(strTemplate, CREATE_VISIBLE);

        if (!bOK)
        return;

        double maximum = -100;
        double minimum = 100;
        double scale;

        for(int i=num1; i<=num2; i++)           //cycle through worksheets
        {
                string suffix ((string) i);
                string name = prefix + suffix;

                Worksheet wks(name);

                if(wks.IsValid()==FALSE) continue;

                printf("%s\n",name);            //display current worksheet name

                Dataset ds1(wks,colNum), de1(wks,0);  //assign x and y values to curve
                Curve cv(wks,colNum);           //object
                ASSERT(cv.IsValid());
                scale = de1[0];

                GraphLayer grlay = grph.Layers(0);
                ASSERT(grlay.IsValid());
```

```
            bOK = 0 <= grlay.AddPlot(cv);          //plot current curve
            if (!bOK)
            return;

            /* evaluate whether max./min. y value is larger/smaller than any previous
            values; if so, the value is saved */
            double maxtemp = max(ds1);
            double mintemp = min(ds1);

            if(maxtemp > maximum) maximum = maxtemp;
            if(mintemp < minimum) minimum = mintemp;
        }

        GraphLayer gl = Project.ActiveLayer();
        if(gl)
        {
            Scale scy(gl.Y);                       //set y scale
            scy.From = minimum*0.95;
            scy.To = maximum*1.04;

            if(scale==162)                         //set x scale (for C_K- or S_L-edge)
            {
                Scale scx(gl.X);
                scx.From = 162;
                scx.To = 202;
                scx.Inc = 5;
            }
            else
            {
                Scale scx(gl.X);
                scx.From = 280;
                scx.To = 320;
                scx.Inc = 5;
            }
        }
        grph.Rename("i0plot");                     //set plot name to "i0plot"
        printf("Finished!\n");
}


/*      The function multiplot plots a series of worksheets, which have the same prefix and a
        numeral suffix, in one graph (x = 1st column). The plots are automatically resized to
        the data and labeled with the worksheet name.(meant for use with NEXAFS spectra)
        Input:
        prefix = worksheet prefix
        num1 = beginning suffix number
        num2 = ending suffix number
        colNum = column number of y data (starts with 0 from left)*/

void multiplot(string prefix, int num1, int num2, int colNum)
{
        printf("Graphed:\n");

        GraphPage grph;
        string strTemplate="nexafs.otp";
        BOOL bOK = grph.Create(strTemplate, CREATE_VISIBLE);

        if (!bOK)
            return;
```

```
double maximum = -100;
double minimum = 100;
double scale;

for(int i=num1; i<=num2; i++)                    //cycle through worksheets
{
        string suffix ((string) i);
        string name = prefix + suffix;

        Worksheet wks(name);

        if(wks.IsValid()==FALSE) continue;

        printf("%s\n",name);                     //display current worksheet name

        Dataset ds1(wks,colNum), de1(wks,0);  //assign x and y values to curve
        Curve cv(wks,colNum);                    //object
        ASSERT(cv.IsValid());
        scale = de1[0];

        GraphLayer grlay = grph.Layers(0);
        ASSERT(grlay.IsValid());

        bOK = 0 <= grlay.AddPlot(cv);            //plot current curve
        if (!bOK)
        return;

        /* evaluate whether max./min. y value is larger/smaller than any previous
        values; if so, the value is saved */
        double maxtemp, mintemp;
        maxtemp = max(ds1);
        mintemp = min(ds1);

        if(maxtemp > maximum) maximum = maxtemp;
        if(mintemp < minimum) minimum = mintemp;
}

GraphLayer gl = Project.ActiveLayer();
if(gl)
{
        Scale scy(gl.Y);                         //set y scale
        scy.From = minimum*0.95;
        scy.To = maximum*1.04;

        if(scale==162)                           //set x scale (for C_K- or S_L-edge)
        {
                Scale scx(gl.X);
                scx.From = 162;
                scx.To = 202;
                scx.Inc = 5;
        }
        else
        {
                Scale scx(gl.X);
                scx.From = 280;
                scx.To = 320;
                scx.Inc = 5;
        }
}
```

```
	grph.Rename("nexafs");				//name graph "nexafs"
	printf("Finished!\n");
}


/*	The function multinorm normalizes a column in a series of worksheets which have
	the same prefix and a numeral suffix using the function norm.
	Input:
	prefix = worksheet prefix
	num1 = beginning suffix number
	num2 = ending suffix number
	colNum = column number to be normalized (starts with 0 from left)*/

void multinorm(string prefix, int num1, int num2, int colNum)
{
	printf("Normalized:\n");

	for(int i=num1; i<=num2; i++)		//cycle through worksheets
	{
		string suffix ((string) i);
		string name = prefix + suffix;

		Worksheet wks(name);

		if(wks.IsValid()==FALSE) continue;

		printf("%s\n",name);

		norm(name, colNum);
	}

	printf("Finished!\n");
}


/*	The function wksi0 creates a worksheet in which a single column from each
	worksheet is successively placed into a column in a new worksheet. The columns
	must have the same x values and the left-most column of the new worksheet is
	resevered for these values. (intended to place multiple I0 curves into one worksheet)
	Input:
	prefix = worksheet prefix
	num1 = beginning suffix number
	num2 = ending suffix number
	colNum = column number of y data (starts with 0 from left)*/

void wksi0(string prefix, int num1, int num2, int colNum)
{
	printf("Added:\n");

	Worksheet Nex;

	if(Nex.Create())				//create new worksheet
		printf("New wks(%s) created\n", Nex.GetPage().GetName());
	Dataset peN(Nex, 0), sigT(Nex,1);
	vector<double> T, O;

	for(int i=num1; i<=num2; i++)		//cycle through worksheets
	{
```

```
                string suffix ((string) i);
                string name = prefix + suffix;

                Worksheet wks(name);

                if(wks.IsValid()==FALSE) continue;

                printf("%s\n",name);
                int newcol = Nex.AddCol(name);          //adds a new column for current
                                                        //worksheet and names it after the
                                                        //current worksheet
                Dataset peO(wks,0);
                Dataset sigO(wks, colNum);
                Dataset sigN(Nex, newcol);
                int Size=sigO.GetSize();
                sigN.SetSize(Size);

                sigN = sigO;                            //copy values from old worksheet
                                                        //to new worksheet

                if(i==num1)                             //set new worksheet to size of the first
                {                                       //worksheet evaluated
                        int Size2=peO.GetSize();
                        peN.SetSize(Size2);
                        peN = peO;
                }
                if(!(peO[1]==peN[1])) printf("Check the energies for %s!!\n",name);
                                                        //energy scale (x) check

                O = sigO;
                int Size3 = O.GetSize();
                T.SetSize(Size3);
                T = T + O;
        }

        sigT = T;
        printf("Finished!\n");
}


/*      The function plot creates multiple plots from a specific column of multiple worksheets,
        each in its own graph (x = 1st column).
        Input:
        prefix = common worksheet prefix
        num1 = beginning suffix number
        num2 = ending suffix number
        colN = column number of y data (starts with 0 from left)*/

void plot(string prefix, int num1, int num2, int colN)
{
        printf("Graphed:\n");

        for(int i=num1; i <= num2; i++)                 //cycle through worksheets
        {
                string suffix ((string) i);
                string name = prefix + suffix;

                Worksheet wks(name);
```

```
        if(wks.IsValid()==FALSE) continue;

        printf("%s\n",name);

        Dataset ds(wks,colN), de1(wks,0);
        Curve cv(wks,colN);
        ASSERT(cv.IsValid());

        GraphPage grph;                         //create graph from template
        string strTemplate="nexafs.otp";
        BOOL bOK = grph.Create(strTemplate, CREATE_VISIBLE);

        if (!bOK)
        return;

        GraphLayer grlay = grph.Layers(0);
        ASSERT(grlay.IsValid());

        bOK = 0 <= grlay.AddPlot(cv);           //plot data on graph
        if (!bOK)
        return;


        double maximum(max(ds));                //find max./min. values in data
        double minimum(min(ds));

        GraphLayer gl = Project.ActiveLayer();
        if(gl)
        {
                Scale scy(gl.Y);                //set y scale
                scy.From = maximum*0.95;
                scy.To = minimum*1.04;


                if(de1[0]==162)                 //set x scale (for C_K- or S_L-edge)
                {
                        Scale scx(gl.X);
                        scx.From = 162;
                        scx.To = 202;
                        scx.Inc = 5;
                }
                else
                {
                        Scale scx(gl.X);
                        scx.From = 280;
                        scx.To = 320;
                        scx.Inc = 5;
                }
        }

grph.Rename(name+"g");                          //name graph after worksheet+"g"

string LTcmd;                                   //add worksheet name as label to
string str1 = "label -d 300 4600 ";             //graph
string str2 = ";";
LTcmd = str1+name+str2;
LT_execute(LTcmd);
}

printf("Finished!\n");
```

```
}


/*      The function nex divides a raw NEXAFS spectrum by the background spectrum in
        the worksheet "Background" and creates a new worksheet with the divided values
        called input:letter+NEXAFS worksheet name (x = 1st column, y = 2nd column). An
        energy shift between the raw data and the background must be specified (0 = no
        shift). The new column is automatically normalized using the norm function.
        wksName = worksheet name
        letter = prefix letter for new worksheet
        shift = energy shift of background (eV) */

void nex(double shift, string letter, string wksName)
{
        Worksheet Original(wksName), Nex, Bgd("Background");
                                                //assign worksheet objects
        if(Nex.Create("nexafs.otw"))            //create new worksheet for output data
        {
                Nex.GetPage().Rename(letter+wksName);       //name new worksheet
                printf("New wks(%s) created\n", Nex.GetPage().GetName());    //display name
        }

        Dataset peO(Original,0), sigO(Original,1), peN(Nex,0), sigN(Nex,1),
                        bgdOE(Bgd,0), bgdO(Bgd,1), bgdN(Nex,4), normsigN(Nex,2),
                        bgdNE(Nex,3);                   //assign columns to dataset objects

        vector<double> pe(peO), sig(sigO), bgd(bgdO), normsig, bgdE(bgdOE);
                                                //load dataset values into vectors

        bgdE=bgdE+shift;                        //shift background by specified energy

        peN=pe; sigN=sig; bgdN=bgd; bgdNE=bgdE;
                                                //copy vectors to worksheet

        int Size=sig.GetSize();                 //set energy vector size to signal size
        pe.SetSize(Size);

        vector normsigNvec(Size);               //create vector for normalized signal

        double E1, B, S;

        for(int i=0; i < Size; i++)             //divide each raw data point by the
        {                                       //corresponding background point
                E1=pe[i];
                B=Data_table(E1, &bgdN, &bgdNE);
                S=sig[i];

                normsigNvec[i]=-(S/B);
        }

        normsigN=normsigNvec;

        norm(Nex.GetPage().GetName(), 2);       //normalize new worksheet
}


/*      The function nexmulti runs the function nex on a series of worksheets which have
        the same prefix and a numeral suffix.
```

```
	prefix = common worksheet prefix
	num1 = beginning suffix number
	num2 = ending suffix number
	shift = energy shift of background (eV)
	letter = prefix letter for new worksheet */

void nexmulti(string prefix, int num1, int num2, double shift, string letter)
{
	printf("Normalized:\n");

	for(int i=num1; i <= num2; i++)			//cycle through worksheets
	{
		string suffix ((string) i);
		string name = prefix + suffix;

		Worksheet wks(name);
		if(wks.IsValid()==FALSE) continue;

		nex(shift, letter, name);			//run nex on current worksheet
	}
}
```

Acknowledgements

Over the last year and a half, it has become clear to me that scientific progress is based on the work of many collaborators, even within a single project such as this one. Without the input and work of many people, from students to professors, such a complete picture this experimental system would not have been possible. My thanks goes to all those who contributed to this project.

Foremost, I would like to thank Dr. M.G. Ramsey. Under his patient guidance I have come to appreciate how the scientific process is used to investigate the specific questions we set before us. The creativity in his approach is both inspiring and a source of motivation. He was the first professor whom I met at the university, and I can still remember him saying, "This is silly to speak in German, why don't we speak in English."

I would like to thank the head of our group and chairman of my Master's examination board, Dr. F.P. Netzer, who maintains a professional research atmosphere in which it is a pleasure to work. His experience and accessibility are valuable resources.

My thanks also goes to: Dr. G. Koller, whose friendship and support were irreplaceable during the time of my thesis and from whom I have learned much. Dr. J.K. Krenn, who served as the second examiner on the examination board and with whom several AFM measurements were made. Dr. S. Eck, for his introduction to the SCIENTA system. Dr. C. Teichert and G. Hlawacek, who contributed both several AFM measurements and analysis of the resulting data. Drs. P. Zeppenfeld, M. Hohage and L. Sung for RDS measurements and analysis. Dr. R. Resel and O. Lengyel for XRD measurements and analysis. Dr. C. Castellarin-Cudia for the STM images of TiO2(110) and her encouragement as I was working towards beginning my thesis. Dr. G. Tzvetkov for help with NEXAFS experiments and his support as another foreigner lost in Graz. Dr. J. Ivanco for always offering help and advice when I needed it. B. Winter for the schematics in Chapter 1 and her comradeship in the molecule group. F. Pfuner, who helped with NEXAFS experiments and with whom I could commiserate about the life of a Master's student. M. Sock and J. Schoiswohl for their help and advice on various difficulties and support as fellow students.

I could not have asked for a better environment in which to work. It has been a great opportunity and a pleasure.